

Freeze tolerant soft matter

Citation for published version (APA):

Olijve, L. L. C. (2015). *Freeze tolerant soft matter*. [Phd Thesis 1 (Research TU/e / Graduation TU/e), Chemical Engineering and Chemistry]. Technische Universiteit Eindhoven.

Document status and date:

Published: 01/01/2015

Document Version:

Publisher's PDF, also known as Version of Record (includes final page, issue and volume numbers)

Please check the document version of this publication:

- A submitted manuscript is the version of the article upon submission and before peer-review. There can be important differences between the submitted version and the official published version of record. People interested in the research are advised to contact the author for the final version of the publication, or visit the DOI to the publisher's website.
- The final author version and the galley proof are versions of the publication after peer review.
- The final published version features the final layout of the paper including the volume, issue and page numbers.

[Link to publication](#)

General rights

Copyright and moral rights for the publications made accessible in the public portal are retained by the authors and/or other copyright owners and it is a condition of accessing publications that users recognise and abide by the legal requirements associated with these rights.

- Users may download and print one copy of any publication from the public portal for the purpose of private study or research.
- You may not further distribute the material or use it for any profit-making activity or commercial gain
- You may freely distribute the URL identifying the publication in the public portal.

If the publication is distributed under the terms of Article 25fa of the Dutch Copyright Act, indicated by the "Taverne" license above, please follow below link for the End User Agreement:

www.tue.nl/taverne

Take down policy

If you believe that this document breaches copyright please contact us at:

openaccess@tue.nl

providing details and we will investigate your claim.

Freeze tolerant soft matter

PROEFSCHRIFT

ter verkrijging van de graad van doctor aan de
Technische Universiteit Eindhoven, op gezag van de
rector magnificus prof.dr.ir. F.P.T. Baaijens, voor een
commissie aangewezen door het College voor
Promoties, in het openbaar te verdedigen op
donderdag 8 oktober 2015 om 16:00 uur.

door

Luuk Lambertus Christina Olijve

geboren te Heerlen

Dit proefschrift is goedgekeurd door de promotoren en de samenstelling van de promotiecommissie is als volgt:

voorzitter: prof.dr.ir. R.A.J. Janssen

promotor: prof.dr. E.W. Meijer

copromotor: dr.ir. I.K. Voets

leden: prof.dr.ir. J.C.M. van Hest (RUN)

prof.dr. A.L. DeVries (University of Illinois)

prof.dr. N.A.J.M. Sommerdijk

prof.dr. E.M. Meijer

adviseur: dr. M.I. Gibson (University of Warwick)

Cover design: Koen Olijve and Luuk Olijve

Printed by: Gildeprint, Enschede

A catalogue record is available from the Eindhoven University of Technology Library

ISBN: 978-90-386-3920-8

This work has financially been supported by NWO (Veni grant 700.10.406) and the European Union (FP7-PEOPLE-288 2011-CIG contract 293788, ERC-2014-StG contract 635928).

Table of contents

Chapter 1

Introduction

1.1 Towards freeze tolerant materials	2
1.2 Freeze protection in Nature	2
1.3 Activity of antifreeze proteins	4
1.4 Identifying the ice binding plane of antifreeze proteins	6
1.5 Ice binding mechanism of antifreeze proteins	7
1.6 Stopping ice growth with synthetic polymers	9
1.7 Advances in polymer sciences	9
1.8 Macromolecular structure determination using small angle X-ray scattering	11
1.9 Aim and outline	14
1.10 References	16

Chapter 2

Blocking rapid ice crystal growth through non-basal plane adsorption of antifreeze proteins

2.1 Introduction	20
2.2 Results	24
2.2.1 Freezing point determination using the sonocrystallization method	24
2.2.2 Activity ranking based on cryoscopy and sonocrystallization experiments	26
2.2.3 Sonocrystallization TH activity correlates to IRI activity	30
2.3 Discussion	31
2.4 Conclusion	33
2.5 Materials and methods	34
2.6 References	37

Chapter 3

Ice binding of poly(vinyl alcohol)

3.1 Introduction	42
------------------	----

3.2 Results	44
3.2.1 Kinetics of RAFT polymerization of vinyl ester monomers	44
3.2.2 Hydrolysis of poly(vinyl esters) to poly(vinyl alcohol)	46
3.2.3 Antifreeze activity of poly(vinyl alcohol)	47
3.2.4 Synthesis of fluorescently labeled poly(vinyl alcohol)	49
3.2.5 Characterization of fluorescently labeled poly(vinyl alcohol)	51
3.3 Discussion	53
3.3.1 Controlled radical polymerization of poly(vinyl alcohol)	53
3.3.2 Conformation of poly(vinyl alcohol) at the ice-water interface	54
3.4 Conclusion	55
3.5 Materials and methods	56
3.6 References	60

Chapter 4

A molecular bottlebrush that blocks ice growth

4.1 Introduction	62
4.2 Results	63
4.2.1 ATRP of TMS-hydroxyethyl methacrylate and preparation of macro-CTA	63
4.2.2 Preparation of PPXEM-g-PVA polymer brushes	64
4.2.3 Structural characterization of the PVA molecular bottlebrush	66
4.2.4 Antifreeze activity of the PVA molecular bottlebrush	68
4.3 Discussion	69
4.4 Conclusion	70
4.5 Materials and methods	71
4.6 References	74

Chapter 5

A new structural model of a 34 kDa dimeric type I antifreeze protein

5.1 Introduction	76
5.2 Results	77

5.2.1 Guinier and form factor analysis	77
5.2.2 Structural model of the protein complex	80
5.2.3 Rigid body modeling	81
5.3 Discussion	82
5.4 Conclusion	84
5.5 Materials and methods	85
5.6 References	88

Chapter 6

A calcium-induced conformational change of an ice-anchoring protein domain studied using small angle X-ray scattering

6.1 Introduction	92
6.2 Results	93
6.2.1 Validation of crystal structure	93
6.2.2 Impact of calcium binding	94
6.3 Discussion	96
6.4 Conclusion	97
6.5 Materials and methods	98
6.6 References	100
Summary	101
Curriculum Vitae	103
List of publications	104
Dankwoord	105

Chapter 1

General introduction

1.1 Towards freeze tolerant materials

Many industrial products and processes rely on antifreeze formulations to prevent ice formation (anti-icing) or facilitate ice removal (de-icing). For example, effective protection against ice formation and/or fast removal of ice on airplane wings before take-off prevents costly delays; prevention of attachment of ice to the rotor blades of windmills maximizes the efficiency; inhibition of hydrate plug formation avoids rupture of natural gas pipelines; and anti-icing of asphalt roads reduces frost damage. Typically, de-icing and anti-icing strategies involve the use of antifreeze mixtures of various compounds including salts and glycols such as methanol, glycerol and propylene glycol. These methodologies rely predominantly on a colligative depression of the freezing point of water (herein the freezing point depression is directly proportional to the additive concentration) or a kinetic inhibition of ice nucleation. While these methods are successful in various areas, they cannot be applied to most soft materials as they are toxic to biological materials and/or change the physical properties of soft matter since large antifreeze additive concentrations are needed.

Freezing is often detrimental to soft matter, as it perturbs colloidal stability through a reduction in free volume. For example, freezing of paints leads to irreversible coagulation of the components, which makes the paint unusable.¹ Furthermore, many foods deteriorate when stored for a long time at low temperatures. For example, the tastiness of ice cream diminishes after prolonged low temperature storage due to the formation of large ice crystals.² Also, biological materials such as human cells, tissues and organs have significantly reduced viability after cold-temperature storage, especially after repeated freeze-thawing.³ When the interstitial fluids of tissues partially freeze, solutes become concentrated and exert an osmotic pressure on cells, resulting in shrivelled cells and disintegrated blood vessels. Even when complicated cooling strategies are applied, organ transplants can only be stored for a few hours before deterioration.⁴ Therefore, avoiding ice formation and freeze damage of (hydrated) soft matter requires an approach which has negligible effect on osmotic pressure and the mechanical, structural and functional properties of the material.

1.2 Freeze protection in Nature

Organisms living in cold and ice-laden climates face the risk of freeze damage. Cold-adapted species use various protective mechanisms during winter time to become either freeze tolerant or freeze avoidant, such as dehydration of their peripheral body parts, production of high concentrations of glycols (sugars or glycerol), excretion of waxes on their skin, etc.⁵ Combinations of these survival strategies enable darkling beetles, *U. ceramboides*, from interior Alaska to survive temperatures below -60 °C.⁶ Snow fleas hop around on snow banks at -7 °C,⁷ and frogs have been found completely frozen and hard as a rock during hibernacula for over 6 months, but were able to recover without any tissue damage.⁸

Many freeze avoidant organisms produce antifreeze proteins (AFPs). Antifreeze glycoproteins (AFGPs) were first discovered in 1969 at McMurdo station in notothenioid fishes, and over the past 45 years AFPs have been isolated from different biological kingdoms (Figure 1).^{9,10} Although the name ‘antifreeze proteins’ suggests that ice formation is prevented, AF(G)Ps bind to ice crystal surfaces and rather modify ice growth than avoid ice formation altogether. As a result of direct ice-binding, AFPs were found to shape the growing ice crystal, inhibit recrystallization of ice, and depress the non-equilibrium freezing point without changing the melting point. This difference between the freezing and melting point is a non-colligative effect termed thermal hysteresis.¹¹ In contrast to highly concentrated solutions of colligative antifreeze agents such as salts and glycols, AFPs depress the freezing point with minimal effect on the osmolality of the organisms’ body fluids.

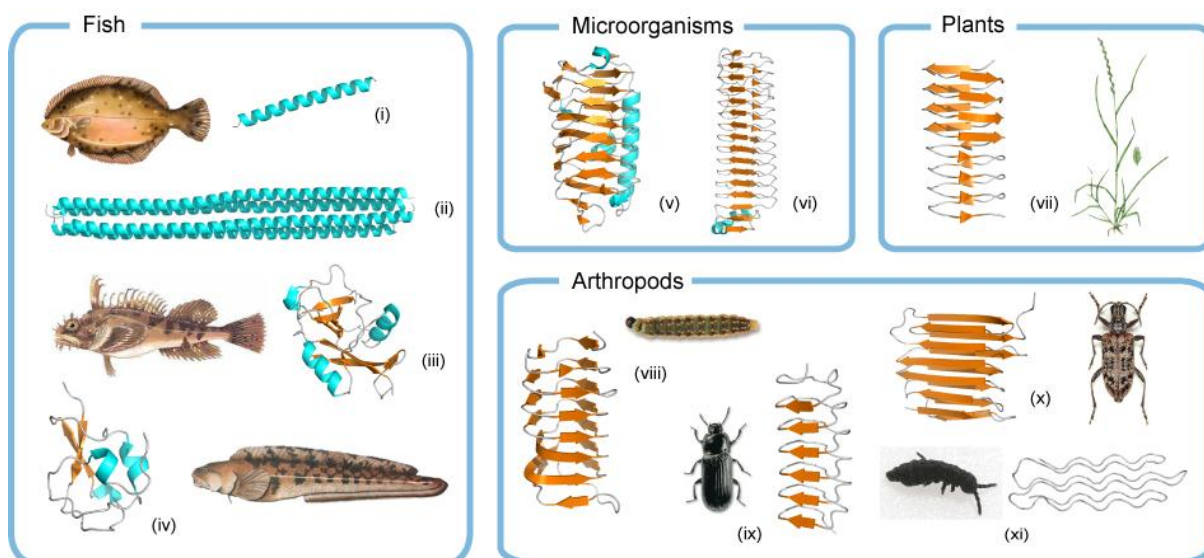


Figure 1: Overview of crystal structures of antifreeze proteins (α -helix, cyan; β -sheet, orange; coil, grey) and respective organism producing the AFP. (i) type I AFP from winter flounder (PDB: 1WFA), (ii) hypAFP1 or Maxi from winter flounder (PDB: 4KE2), (iii) type II AFP from sea raven (PDB: 2PY2), (iv) type III AFP from ocean pout (1HG7), (v) *Ti*AFP from grey snow mold (PDB: 3VN3), (vi) *Mp*AFP from an Antarctic bacterium (PDB: 3P4G), (vii) *Lp*AFP from winter ryegrass (PDB: 3ULT), (viii) *sbw*AFP from spruce budworm (PDB: 1M8N), (ix) *Tm*AFP from mealworm beetle (PDB: 1EZG), (x) *Ri*AFP from ribbed pine borer (PDB: 4DT5), (xi) *sf*AFP from snow flea (PDB: 2PNE).

1.3 Activity of antifreeze proteins

The activity of AFPs is evidenced on a macroscopic level by activity assays that monitor thermal hysteresis (TH), ice recrystallization inhibition (IRI) and/or dynamic ice shaping. In a classical TH assay, a small ice crystal suspended in a solution of AFP is slowly cooled, typically with a rate of 0.02 °C/min. The growth shape of the ice is changed due to the binding of AFPs onto the ice crystal surface (Figure 2A). These experiments performed using nanoliter cryoscopy show that the growth of an ice crystal can be completely arrested within the thermal hysteresis gap. Due to the dynamic ice shaping ability of AFPs, ice crystals with different morphologies are formed depending on the type of AFP used in the experiment, ranging from bipyramidal shapes to hexagonal plates and lemon shapes (Figure 2B). Using GFP-tagged AFPs in a microfluidic device, which allows for buffer exchange around the ice crystal, irreversible binding of AFPs to specific ice planes was demonstrated (Figure 2C).

In a typical IRI experiment, a sample solution is quickly frozen to -40 °C to form polycrystalline ice and the recrystallization process of the sample is monitored at a constant temperature (-6 °C) using an optical microscope.^{18,19} As a result of recrystallization processes, large ice crystals start to grow at the expense of small ice crystals. AFPs effectively immobilize the grain boundaries of ice crystals thereby decelerating the disproportionation process, which is termed ice recrystallization inhibition activity (Figure 3). The mechanism of ice recrystallization is quite complex and has been described in detail by Knight *et al.*^{18,19} In brief, grain boundaries of polycrystalline ice are interfaces of differently oriented ice microstructures. As a result of nucleation and migration processes, large ice crystals with more concave boundaries will form since these structures are energetically more favorable. AFPs that act as an impurity on the ice surface are proposed to interfere with the migration process of water molecules and disfavor the addition of new water molecules to grain boundaries. One major obstacle in the quantification of IRI is the lack of a high throughput method amenable to a broad concentration range.^{20,21}

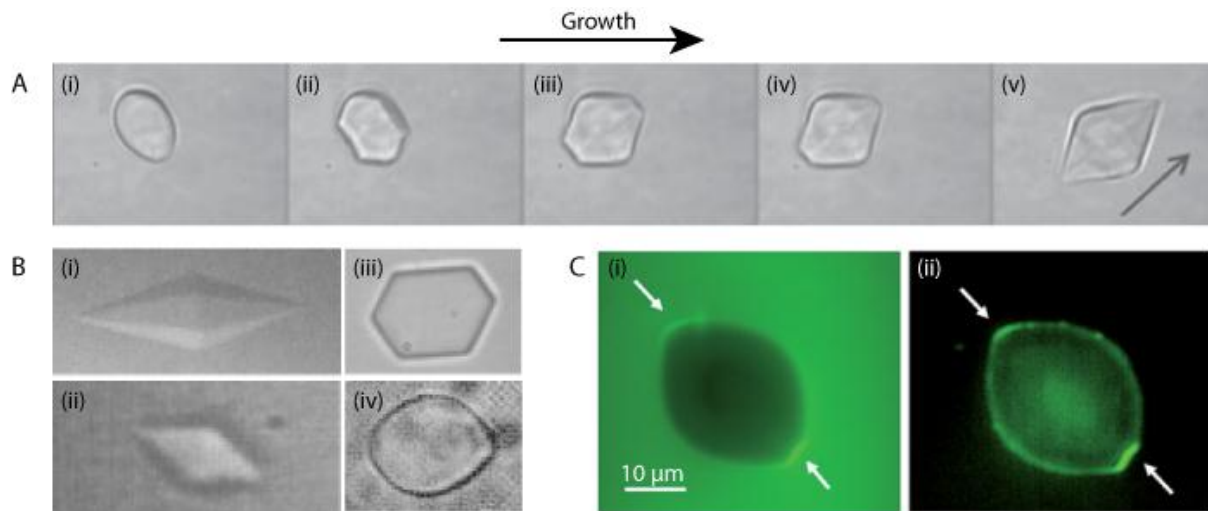


Figure 2: (A) In nanoliter cryoscopy, the growth of an ice crystal is monitored during slow cooling. In (i-v), snapshots are shown of dynamic ice shaping of an ice crystal suspended in a solution of AFGP cooled from T_m (i) down to $0.1\text{ }^\circ\text{C}$ below T_m (v). The time lapse between images (i - v) is 2 min, 3.5 min, 2 min, 40 s and 4 min respectively. The arrow in (v) denotes the c -axis.¹² (B) Ice crystal morphologies obtained using nanoliter cryoscopy in a solution of (i) AFP1,¹³ (ii) AFP-III,¹⁴ (iii) *Mp*AFP,¹⁵ (iv) *Tm*AFP.¹⁶ (C) Ice crystals incubated with GFP-tagged *Tm*AFP (i) before buffer exchange and (ii) after buffer exchange. Arrows indicate basal plane.¹⁷

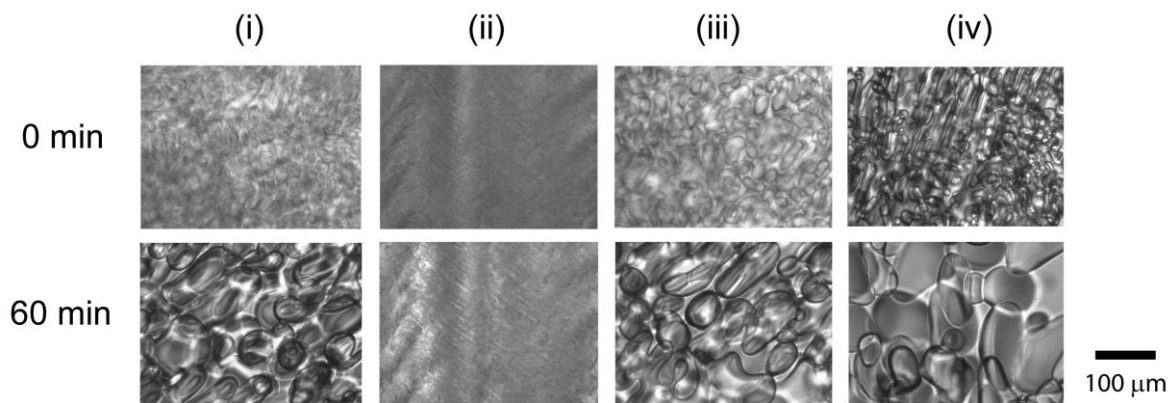


Figure 3: Ice recrystallization inhibition during annealing of (i) buffer, (ii) AFP-III 1 mg/ml, (iii) BSA 1 mg/ml, and (iv) ethylene glycol 1 v/v% at a constant temperature of $-6\text{ }^\circ\text{C}$. All samples are prepared in 20 mM Tris buffer, pH 7.5 with 20 w/w% sucrose.

1.4 Identifying the ice binding plane of antifreeze proteins

A major breakthrough in understanding the ice binding mechanism of AFPs was the development of ice etching and fluorescence ice plane affinity (FIPA) analysis. With these techniques, the specific ice binding plane of the AFPs to Ih ice could be determined. Both methods involve the slow growth of an ice hemisphere with known crystal orientation in a solution of AFPs. Ice etching involves the sublimation of the outer ice hemisphere surface to observe the ice bound proteins, from which the ice binding plane is determined (Figure 4C i). This laborious sublimation step is not necessary in FIPA analysis, and ice binding planes are readily observed from the fluorescence intensity (Figure 4C ii).

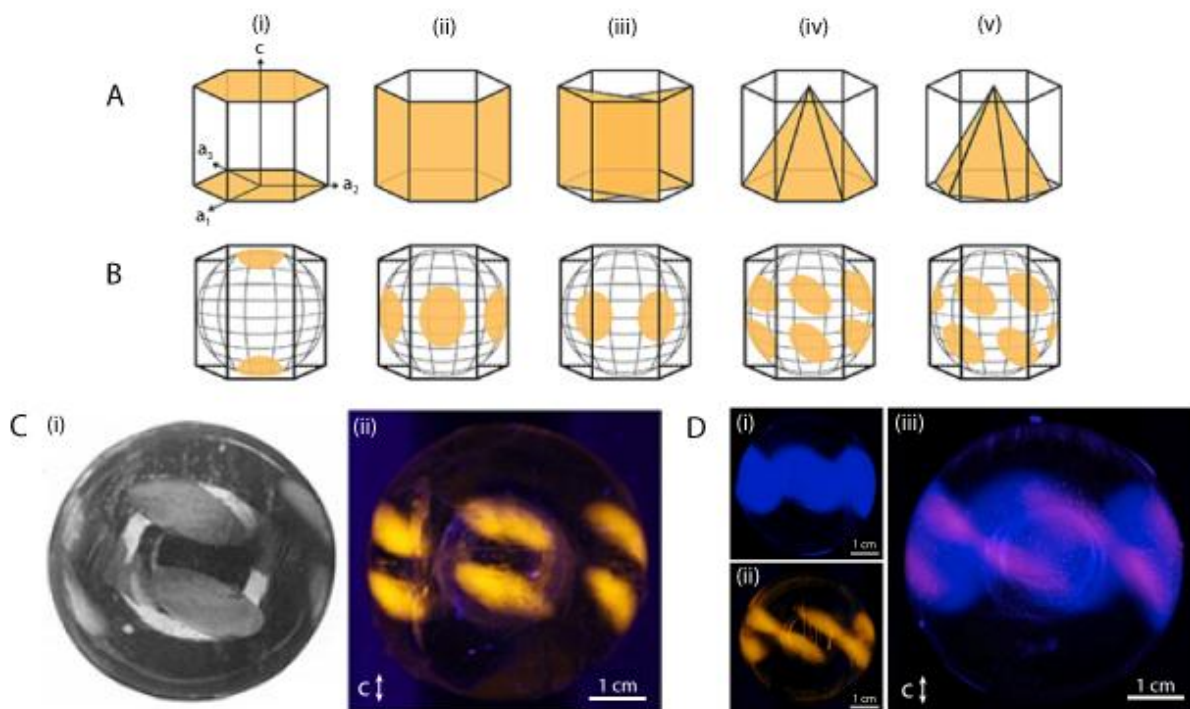


Figure 4: Ice etching and FIPA analysis. (A) Representation of ice planes of Ih ice, (i) basal plane, (ii) primary prism plane, (iii) secondary prism plane, (iv) pyramidal plane aligned with the a -axes, and (v) pyramidal plane offset to the a -axes. (B) Corresponding ice etching and FIPA analysis. (C) Ice etching experiment (i) of type I AFP (HPLC-6 isoform)²² and corresponding FIPA analysis using TRITC-labeled *wfAFP1*. (D) FIPA analysis of (i) pacific blue-labeled type III AFP (*nfeAFP8* isoform), (ii) TRITC-labeled *wfAFP1*, and (iii) visualization of type III and type I together.²³

1.5 Ice binding mechanism of antifreeze proteins

Despite the development of techniques to measure TH and IRI activity, and methods to determine the ice binding planes, the precise mechanism by which AFPs arrest ice growth is still largely unknown. Proposed adsorption-inhibition mechanisms include the protein acting as an impurity on the growing ice front and thereby sterically hindering the addition of water molecules, resulting in remodeling of the ice lattice (Figure 5). The adsorption of AFPs leads to the formation of a curved outer surface of the ice crystal, thereby increasing the specific surface area of the ice front. The increased interfacial energy of the system results in the formation of an energy barrier before further growth of the ice crystal can occur, which causes a lowering of the freezing point. This mode of action is known as the Gibbs-Thomson effect.²⁴⁻²⁷ Efforts have been made to describe the non-equilibrium freezing point depression qualitatively based on an increase in vapor pressure across a curved surface,²⁸⁻³⁰ however quantitative models yet have to be validated experimentally. In particular, the visual evidence of a single AFP bound on the ice surface is still lacking. Recent developments in super resolution microscopy may offer opportunities to visually examine the ice surface to obtain a molecular description of the ice-water interface in the future.

Another experimental challenge is to obtain detailed structural information on ice-bound AFPs. To date it has been impossible to obtain a crystal structure of ice-bound AFPs, which means that the exact conformation of ice-bound AFP is unknown. Hypothesized ice binding mechanisms have significantly changed over the years, driven largely by newly resolved crystal structures. The first crystal structure of the α -helical type I AFP resulted in the idea that a flat hydrophobic protein surface with regularly positioned threonine residues is driving the ice binding of AFPs via hydrogen bonding.^{22,31} The spatially separated hydroxyl groups of the threonine residues were argued to provide an exact match to the ice lattice. The hydrogen bonding hypothesis was supported after resolving the crystal structure of the β -helical AFP from spruce budworm (*sbw*AFP), which also showed very regularly positioned threonine residues on the putative flat ice binding face of the protein (Figure 6A).³² Soon after, molecular dynamics simulations gave rise to a new theory of anchored clathrate waters.³³ This model proposed that tightly bound ice-like waters on the protein surface are responsible for the proteins ‘freezing onto’ the growing ice surface. This idea was later supported by the observation of ice-like waters on the protein surface in the crystal structure of *Mp*AFP (Figure 6B).¹⁵ Recently, evidence was found for the presence of ice-like water layers at the ice binding site of type III AFP at temperatures above the freezing point by vibrational sum frequency generation (vSFG) experiments.³⁴

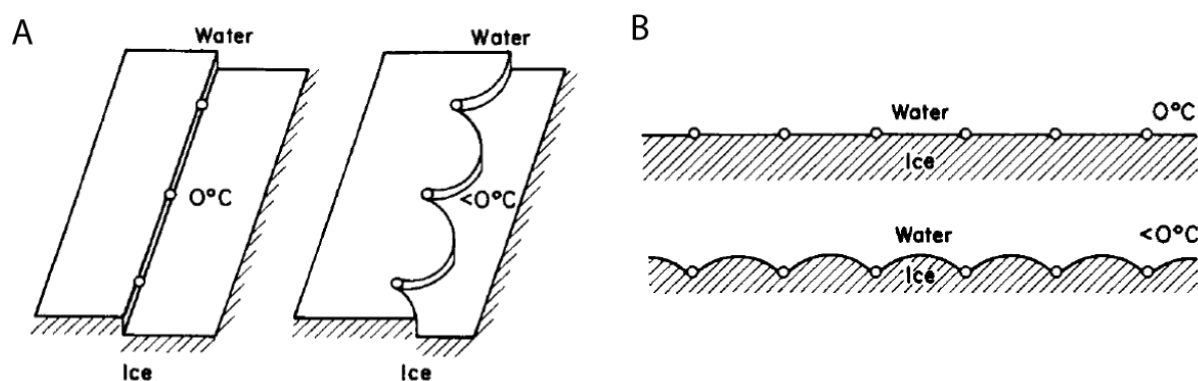


Figure 5: Proposed adsorption-inhibition models to describe the blocking of ice growth by AFPs. Adsorption of AFPs results in a frustrated ice growth; the ice front is forced to grow via the formation of a curved interface between adsorbed proteins. Ice growth in the direction of the adsorbing planes is prevented by either (A) step-growth inhibition (adsorbed proteins prevent ice growth advancing in steps across the adsorption plane), or by (B) surface-pinning (bulging of the ice-surface outward between adsorbed proteins). The large increase in specific surface area is energetically unfavorable, leading to the formation of an energy barrier which has to be overcome before further ice growth can occur after sufficient supercooling. This results in a lowering of the non-equilibrium freezing point as a sharp growth threshold.²²

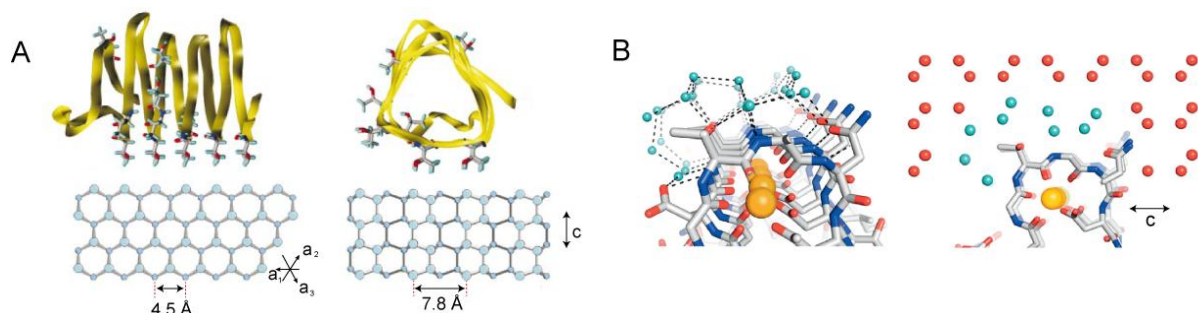


Figure 6: Two hypothesized ice binding mechanisms. (A) The earliest hypothesis was based on the surface complementarity of the ice binding face of AFPs to the ice surface. Regularly positioned threonine residues enable binding to the ice surface via hydrogen bonding of the hydroxyl groups. Illustrated is the binding of *sbw*AFP to the prism (left) and the basal plane (right).³² (B) A recent hypothesis was based on the formation of ice-like hydration waters on the protein surface, via which the protein adsorbs onto the ice surface. The crystal structure of *Mp*AFP shows ice-like waters (cyan spheres) on the protein surface (left). These anchored clathrate waters fit well to the primary prism plane of an ice lattice illustrated by the red spheres (right).¹⁵

1.6 Stopping ice growth with synthetic polymers

Widespread application of AFPs faces two major obstacles. Firstly, open questions regarding the underlying mechanism that governs TH and IRI activity and the mode of ice binding remain to be answered. Secondly, the lack of large quantities of AFPs and the high cost of protein-based materials hamper progress in the development of freeze tolerant soft materials.³⁵ Current research on the synthesis of AFP mimics has primarily focused on synthesizing mimics of AFGPs.³⁶⁻³⁸ Since this often involves complicated sugar chemistry, it is a fascinating academic challenge but will not lead to the realization of an inexpensive synthetic mimic of AFPs amenable to large scale production. Similarly, the naturally occurring polysaccharide xylomannan could be commercially exploited if it is possible to obtain in large quantities, but current synthesis strategies are very complicated.^{39,40} Perhaps the most promising synthetic material is poly(vinyl alcohol) (PVA).³⁵ PVA is known to inhibit the recrystallization of ice,⁴¹ and the beneficial use of PVA for the cryopreservation of human blood cells was recently demonstrated.⁴² Moreover, the synthesis of PVA is simple and possible on large scale. In fact, PVA is already employed in various materials on the market, such as coatings, contact lenses, thickener in latex paints, etc.

1.7 Advances in polymer sciences

Over the past century, the field of organic chemistry has greatly advanced such that organic chemists are able to synthesize (almost) every molecule possible.⁴³ Furthermore, major breakthroughs in polymer chemistry over the past two decades allow for controlled or living radical polymerization strategies (e.g., ATRP and RAFT) and synthesis of complex macromolecular architectures (e.g., block copolymers and brush polymers, Figure 7).^{44,45} In an ideal living polymerization, all chains are initiated simultaneously and grow with similar rate, without irreversible chain transfer or termination. However, in standard radical polymerization, this is not the case. In reversible deactivation radical polymerization, the addition of extra reagents enables the reversible deactivation of propagating radical species, such that the majority of the propagating polymer chains are in the dormant form. Each dormant polymer chain has the same probability to become reactivated and thus all polymer chains have the same propagation rate, resulting in a narrow molecular weight distribution and predetermined molecular weight. Atom transfer radical polymerization (ATRP) is an example of reversible deactivation radical polymerization.⁴⁴ ATRP employs a transition metal complex (usually a copper complex) to activate dormant polymer chains (P_n-X , with $X = \text{halogen, Cl or Br}$) via a one electron transfer process. Simultaneously, the transition metal is oxidized to a higher oxidation state, establishing an equilibrium in this reversible process. Reversible addition-fragmentation chain transfer (RAFT) is also a reversible deactivation radical polymerization technique, but employs a chain transfer agent (CTA) in the form of a thiocarbonylthio

compound.⁴⁵ The Z and R groups on the dithioester of the CTA are chosen according to compatibility with the monomer. The Z-group affects the stability of the C=S bond and the stability of the radical adduct ($P_n-S-C\bullet(Z)-S-R$), thereby modifying addition and fragmentation rates. The R-group must be a good homolytic leaving group and a good initiating species. Overall, the introduction of both ATRP and RAFT has led to a significant development of sophisticated macromolecular architectures (e.g., block copolymers, molecular brushes, etc.), compositions and chain-end functionalities using a wide variety of monomers.⁴⁶

The development of dendrimers and hyperbranched macromolecules led to another class of unique materials (Figure 7). Dendrimers are well-defined macromolecules with a highly branched three-dimensional structure and are synthesized through a stepwise, repetitive reaction sequence.⁴⁷ The monodispersity, lack of entanglement, large number of reactive end-groups, and possible interactions with guest molecules are some examples of the unique material properties of dendrimers. They have found application in drug delivery, catalysis and material science.⁴⁸ For example, the development of Astramol poly(propylene imine) dendrimers has led to a series of industrial applications that make use of the unique structures and properties of the material.⁴⁹ However, due to the high costs of the consecutive synthesis steps on large scale, well-defined hyperbranched macromolecules have gained more attention. For example, Hybrane (DSM, Geleen, Netherlands) has been found to have a profound effect on the crystallization of inorganic and organic compounds from solution.⁵⁰ Research at Shell (Amsterdam, Netherlands) found that some versions of Hybrane were able to suppress the formation of gas hydrates from water-hydrocarbon mixtures, and may be used to avoid hydrate plugs in gas pipelines.⁵¹

The introduction of non-covalent interactions in individual polymer chains has led to the development of (functional) supramolecular materials (Figure 7).⁵² The incorporation of reversible non-covalent bonds results in dynamic and self-healing polymeric materials with easy processability,⁵³ giving a unique interplay between intrinsic processability and material properties.⁵⁴ Advances in understanding supramolecular polymerization pathways and mechanisms further expands the opportunities for the development of a new classes of materials.^{55,56} Supramolecular polymerization of water-soluble benzene-1,3,5-tricarboxamides (BTAs) gave rise to ordered and dynamic supramolecular assemblies and soft materials such as hydrogels which may find use in biomedical applications.⁵⁷ Furthermore, the combination of controlled polymerization techniques and the addition of supramolecular motifs in polymer chains allows for the compaction and folding of single polymer chains in solution and the formation of secondary structures similar to protein folding.⁵⁸ The single polymer chain technology has developed to engineer macromolecules with well-defined compartmentalized architectures and catalytic centers giving rise to artificial enzymes.⁵⁹

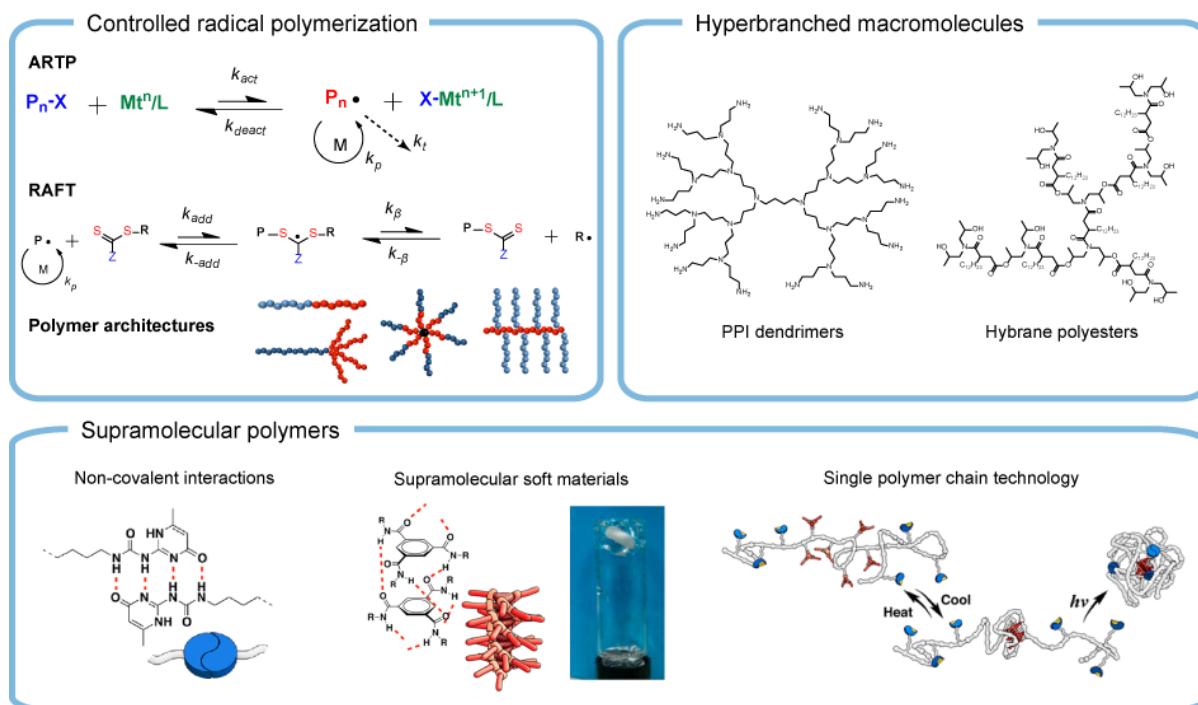


Figure 7: Methods from polymer and material science which could be applied to design antifreeze plastics. Controlled radical polymerization techniques allow for the synthesis of complex polymeric architectures (top left). Hyperbranched molecules form a class of densely packed macromolecules (top right). Combining non-covalent interactions in polymer chemistry allows for dynamic polymer constructs and the design of new soft materials (bottom).

1.8 Macromolecular structure determination using small angle X-ray scattering

Ice binding requires functional groups that adhere to specific ice planes, which must be accessible for docking onto ice. Therefore, it is important to determine the solution structure of (bio)macromolecular antifreezes. Traditionally, X-ray diffraction (XRD) is used to determine the structure and function of proteins at atomic resolution. For example, the crystal structure of *MpAFP* demonstrated the formation of ice-like waters on the protein surface.¹⁵ Unfortunately, it is often difficult - if not impossible - to obtain protein crystals. Moreover, the crystallization buffer is often a poor proxy of physiological conditions relevant for protein function. Also, the solid crystalline state rarely allows for observation of conformational transitions in protein structure induced by different buffer conditions (e.g., salts, pH), temperature or ligand binding. Furthermore, protein crystallography is not amenable to studies of protein (un)folding, aggregation, assembly state, flexible domains, etc., since these tend not to crystallize or remain invisible within crystals due to their mobility/flexibility. Therefore, small angle X-ray scattering is rapidly gaining ground as a complementary method to XRD, which does offer structural information in solution and thus under physiological conditions with no limit to molar mass. SAXS enables the determination of the structure of virtually all proteins with only modest sample preparation requirements since no protein crystals are needed. However, in

SAXS all phase information is lost due to the isotropic reorientation of the proteins in solution, which limits its resolution. Where X-ray crystallography can resolve interatomic distances at 1-3 Å resolution, SAXS cannot be used to describe proteins at the atomic level. Nevertheless, SAXS can be used to characterize the shape and conformation of both small proteins and large protein complexes directly in solution, bridging between the atomic resolution of NMR/XRD and (light/electron) microscopy techniques in terms of length scale.^{60,61}

In small angle X-ray scattering, monochromatic X-rays are scattered over small angles due to a difference in electron density between the protein and solvent (Figure 8). Scattered X-rays are detected and the scattering intensity is radially averaged to obtain a plot of scattering intensity versus scattering vector. Here, the scattering vector is defined as $|\vec{q}| = |\vec{k}_1 - \vec{k}_0|$ and is obtained after calibrating the scattering angle and sample-detector distance using a standard with known diffraction pattern (e.g., silver behenate). The scattering intensity as a function of scattering vector $I(q)$ depends on the electron density difference between sample and solvent (i.e., atomic composition), concentration, molecular weight and the angle dependent form $P(q)$ and structure factor $S(q)$. In general, the angular dependence arises from intra- and interparticle (de)constructive interference effects of the scattered X-rays. Whereas intraparticle interference effects lead to a shape-characteristic scattering curve (i.e., form factor $P(q)$, Figure 9), interparticle interference effects are generally avoided by measuring at low concentrations and optimal buffer conditions to prevent attractive and repulsive forces between proteins ($S(q)$). The difficulty in the data analysis lies within the reconstruction of a 3-dimensional macromolecular structure from a 1-dimensional scattering curve. Form factor analysis of the experimental data is used to derive information on the macromolecular shape and dimension of studied protein or polymer (Figure 9). Further advances in analysis software (ATSAS software package) enable the reconstruction of low resolution models, fitting of crystallographic data to scattering curves and rigid body modeling to reconstruct the 3D architecture of protein complexes.⁶²

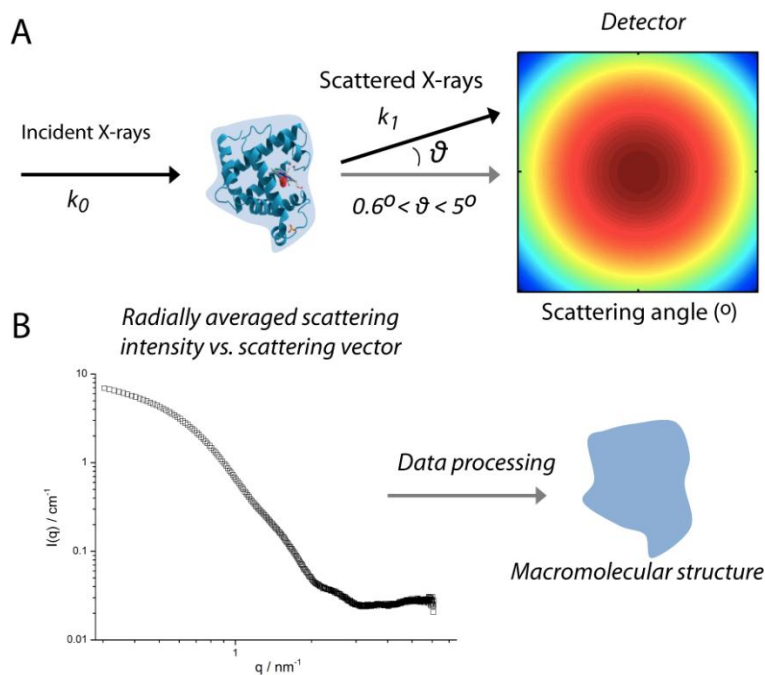


Figure 8: Principle of protein structure determination using small angle X-ray scattering. (A) X-rays are scattered due to an average electron density difference between the protein and solvent. X-rays scattered over small angles are collected on a detector, and (B) the 2D scattering profile is radially averaged to obtain a one-dimensional scattering curve. Advances in data processing techniques allow for the determination of the macromolecular structure of the protein in solution.

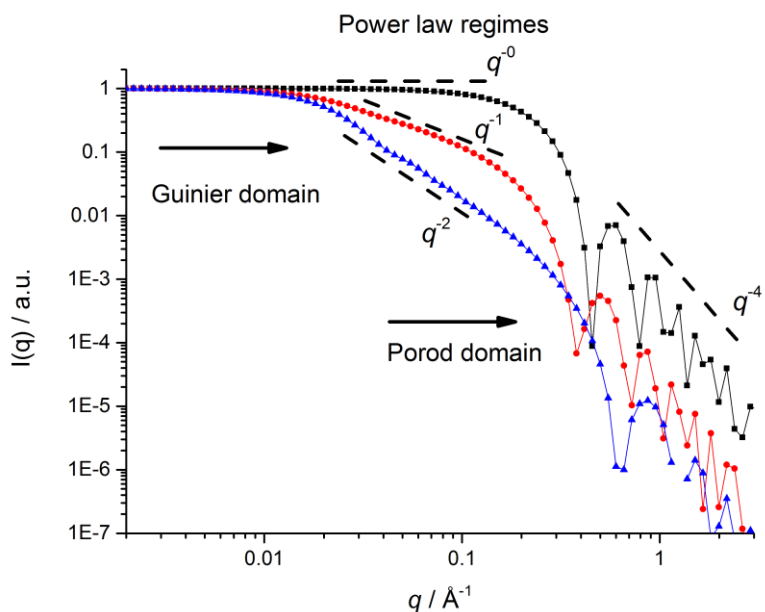


Figure 9: Simulated SAXS curves of homogeneous objects with different geometry (■ sphere, $R = 10$ nm; ● cylinder, $R = 10$ nm and $L = 200$ nm; ▲ lamellae, $D = 10$ nm and $L = 200$ nm). Due to (de)constructive intraparticle interference effects, distinct power law regimes can be identified in the scattering profile. Arrows indicate the start of Guinier and Porod domain, respectively.

1.9 Aim and outline

One major obstacle in the widespread application of both ‘antifreeze proteins’ and ‘antifreeze plastics’ is the limited understanding of the underlying mechanism how AFPs arrest ice growth. Central research questions that remain to be answered are: (1) how is thermal hysteresis (TH) activity related to ice recrystallization inhibition (IRI) activity; (2) what determines the large difference in TH activity of various AFPs; (3) is the ice binding mechanism of synthetic ice binders such as poly(vinyl alcohol) (PVA) similar to AFPs; (4) what is the required macromolecular architecture of synthetic AFP mimics; and (5) how can we determine their macromolecular structure in solution? The central research question in this thesis is: how can we benefit from the current understanding of antifreeze proteins and the advances in polymer sciences to develop antifreeze strategies for soft materials?

The research described in **chapter 2** focuses on the working mechanism of AFPs, aiming to elucidate which factors determine the non-equilibrium freezing point depression (TH) and ice recrystallization inhibition (IRI). All major classes of AFPs are studied using nanoliter cryoscopy, sonocrystallization and IRI activity assays. The results show a direct correlation between the specific ice binding plane, TH activity in sonocrystallization and IRI activity. We conclude that binding to fast growing non-basal planes is essential to stop rapid ice growth processes. Targeting these ice planes specifically will be a key design requirement for polymeric AFP mimics.

In **chapter 3**, the ice binding of poly(vinyl alcohol) is described. PVA is an inexpensive material which is known to inhibit the recrystallization of ice. However, questions remain if the mode of action is similar to AFPs, and how the multivalent adhesion of PVA onto ice is influenced by both polymer molecular weight and tacticity. In chapter 3, the synthesis of PVA via reversible addition-fragmentation chain-transfer (RAFT) polymerization is described, to gain control over molecular weight and tacticity using vinyl ester monomers with varying bulky substituents. Furthermore, the synthesis of fluorescently labeled PVA via a naphthalimide-substituted xanthogenate is reported. The naphthalimide end-functionalized PVA is used to study the ice binding of PVA by fluorescence microscopy.

Chapter 4 describes the synthesis of PVA molecular bottlebrushes by a combination of atom-transfer radical polymerization (ATRP) and RAFT polymerization. The PVA brushes are composed of a rigid backbone with densely grafted PVA side chains, which gives rise to an extended macromolecular topology, as determined using small angle X-ray scattering (SAXS). The effect of the chain architecture and the densely grafted PVA side chains on the multivalent ice-PVA interaction is studied by comparing IRI and TH activity of the PVA brush to the activity of linear PVA polymers.

Chapters 5 and 6 focus on the use of SAXS to study the macromolecular shape of highly asymmetric proteins in solution. In **chapter 5**, the size and shape of a highly active type

1 AFP (hypAFP1) is determined. The experiments demonstrate that the available molecular model of two fully stretched α -helices of 29 nm in length is incorrect. Instead, based on the SAXS data and *ab initio* modeling, a revised structural model of hypAFP1 is proposed consisting of an extended triple helix with a length of 20 nm. In **chapter 6**, the effect of calcium binding on the structural properties of the tetrameric RII protein (tetraRII) is studied. SAXS experiments are used to validate the crystal structure of tetraRII in the presence of calcium. No crystals could be obtained of tetraRII in the absence of calcium. However, SAXS studies reveal that tetraRII is much less rigid in the absence of calcium, providing valuable information on the functional role of the protein in the ice anchoring of the Antarctic bacterium *M. primoryensis*.

1.10 References

1. Zhao, C.L.; Porzio, S.; Smith, A.; Ge, H.; Davis, H.T.; Scriven, L.E. *J. Coating. Tech. Res.* **2006**, *3*, 109-115.
2. Petzold, G.; Aguilera, J.M. *Food Biophys.* **2009**, *4*, 378-396.
3. Carpenter, J.F.; Hansen, T.N. *Proc. Natl. Acad. Sci. USA* **1992**, *89*, 8953-8957.
4. Berendsen, T.A.; Bruinsma, B.G.; Puts, C.F.; Saeidi, N.; Usta, O.B.; Uygun, B.E.; Izamis, M.L.; Toner, M.; Yarmush, M.L.; Uygun, K. *Nat. Med.* **2014**, *20*, 790-793.
5. Duman, J.G. *Annu. Rev. Physiol.* **2001**, *63*, 327-357.
6. Walters, K.R.; Serianni, A.S.; Sformo, T.; Barnes, B.M.; Duman, J.G. *Proc. Natl. Acad. Sci. USA* **2009**, *106*, 20210-20215.
7. Graham, L.A.; Davies, P.L. *Science* **2005**, *310*, 461.
8. Larson, D.J.; Middle, L.; Vu, H.; Zhang, W.; Serianni, A.S.; Duman, J.; Barnes, B.M. *J. Exp. Biol.* **2014**, *217*, 2193-2200.
9. DeVries, A.L.; Wohlschlag, D.E. *Science* **1969**, *163*, 1073-1075.
10. Davies, P.L. *Trends Biochem. Sci.* **2014**, *39*, 548-555.
11. Knight, C.A.; DeVries, A.L.; Oolman, L.D. *Nature* **1984** *308*, 295-296.
12. Bar-Dolev, M.; Celik, Y.; Wettlaufer, J.S.; Davies, P.L.; Braslavsky, I. *J. R. Soc. Interface* **2012**, *9*, 3249-3259.
13. Davies, P.L.; Baardsnes, J.; Kuiper, M.J.; Walker, V.K. *Phil. Trans. R. Soc. Lond. B* **2002**, *357*, 927-935.
14. Baardsnes, J.; Davies, P.L. *Biochim. Biophys. Acta* **2002**, *1601*, 49-54.
15. Garnham, C.P.; Campbell, R.L.; Davies, P.L. *Proc. Natl. Acad. Sci. U.S.A.* **2011**, *108*, 7363-7367.
16. Graham, L.A.; Liou, Y.C.; Walker, V.K.; Davies, P.L. *Nature* **1997**, *388*, 727-728.
17. Drori, R.; Davies, P.L.; Braslavsky, I. *RSC Adv.* **2015**, *5*, 7848-7853.
18. Knight, C.A.; Hallett, J.; DeVries, A.L. *Cryobiology* **1988**, *25*, 55-60.
19. Knight, C.A.; Wen, D.; Laursen, R.A. *Cryobiology* **1995**, *32*, 23-34.
20. Budke, C.; Heggemann, C.; Koch, M.; Sewald, N.; Koop, T. *J. Phys. Chem. B* **2009**, *113*, 2865-2873.
21. Jackman, J.; Noestheden, M.; Moffat, D.; Pezacki, J.P.; Findlay, S.; Ben, R.N. *Biochem. Biophys. Res. Commun.* **2007**, *354*, 340-344.
22. Knight, C.A.; Cheng, C.C.; DeVries, A.L. *Biophys. J.* **1991**, *59*, 409-418.
23. Basu, K.; Garnham, C.P.; Nishimiya, Y.; Tsuda, S.; Braslavsky, I.; Davies, P.L. *J. Vis. Exp.* **2014**, *83*, e51185.
24. Raymond, J.A.; DeVries, A.L. *Proc. Natl. Acad. Sci. USA* **1977**, *74*, 2589-2593.
25. Knight, C.A.; DeVries, A.L. *Science* **1989**, *245*, 505-507.
26. Knight, C.A.; Wierzbicki, A. *Cryst. Growth Des.* **2001**, *1*, 439-446.
27. Knight, C.A.; DeVries, A.L. *Phys. Chem. Chem. Phys.* **2009**, *11*, 5749-5761.
28. Kristiansen, E.; Zachariassen, K.E. *Cryobiology* **2005**, *51* 262-280.

29. Yeh, Y.; Feeney, R. E. *Chem. Rev.* **1996**, *96*, 601-618.
30. Hall, D.G.; Lips, A. *Langmuir* **1999**, *15*, 1905-1912.
31. Yang, D.S.C.; Sax, M.; Chakrabartty, A.; Hew, C.L. *Nature* **1988**, *333*, 232-237.
32. Greather, S.P.; Kuiper, M.J.; Gagné, S.M.; Walker, V.K.; Jia, Z.; Sykes, B.D.; Davies, P.L. *Nature* **2000**, *406*, 325-328.
33. Nutt, D.R.; Smith, J.C. *J. Am. Chem. Soc.* **2008**, *130*, 13066-13073.
34. Meister, K.; Strazdaite, S.; DeVries, A.L.; Lotze, S.; Olijve, L.L.C.; Voets, I.K.; Bakker, H.J. *Proc. Natl. Acad. Sci. USA* **2014**, *111*, 17732-17736.
35. Gibson, M.I. *Polym. Chem.* **2010**, *1*, 1141-1152.
36. Garner, J.; Harding, M.M. *ChemBioChem* **2010**, *11*, 2489-2498.
37. Peltier, R.; Brimble, M.A.; Wojnar, J.A.; Williams, D.E.; Evans, C.W.; DeVries, A.L. *Chem. Sci.* **2010**, *1*, 538-551.
38. Capicciotti, C.J.; Trant, J.F.; Leclère, M.; Ben, R.N. *Bioconjugate Chem.* **2011**, *22*, 605-616.
39. Ishiwata, A.; Sakurai, A.; Nishimiya, Y.; Tsuda, S.; Ito, Y. *J. Am. Chem. Soc.* **2011**, *133*, 19524-19535.
40. Crich, D.; Rahaman, Y. *J. Org. Chem.* **2011**, *76*, 8611-8620.
41. Budke, C.; Koop, T. *Chem. Phys. Chem.* **2006**, *7*, 2601-2606.
42. Deller, R.C.; Vatish, M.; Mitchell, D.A.; Gibson, M.I. *Nat. Commun.* **2014**, *5*, 3244.
43. Grzybowski, B.A.; Bishop, K.J.M.; Kowalczyk, B.; Wilmer, C.E. *Nat. Chem.* **2009**, *1*, 31-36.
44. Matyjaszewski, K.; Xia, J. *Chem. Rev.* **2001**, *101*, 2921-2990.
45. Moad, G.; Rizzardo, E.; Thang, S.H. *Aust. J. Chem.* **2012**, *65*, 985-1076.
46. Gregory, A.; Stenzel, M.H. *Prog. Polym. Sci.* **2012**, *37*, 38-105.
47. Bosman, A.W.; Janssen, H.M.; Meijer, E.W. *Chem. Rev.* **1999**, *99*, 1665-1688.
48. Grayson, S.M.; Fréchet, J.M.J. *Chem. Rev.* **2001**, *101*, 3819-3867.
49. Jansen, J.F.; De Brabander-van den Berg, E.M.; Meijer, E.W. *Science* **1994**, *18*, 1226-1229.
50. Froehling, P. *J. Polym. Sci. A* **2004**, *42*, 3110-3115.
51. Shell International Research. PCT Patent WO 01/77270, April 7, 2000
52. Sijbesma, R.P.; Beijer, F.H.; Brunsveld, L.; Folmer, B.J.B.; Ky Hirschberg, J.H.K.; Lange, R.F.M.; Lowe, J.K.L.; Meijer, E.W. *Science* **1997**, *278*, 1601-1604.
53. Brunsveld, L.; Folmer, B.J.B.; Meijer, E.W.; Sijbesma, R.P. *Chem. Rev.* **2001**, *101*, 4071-4098.
54. Aida, T.; Meijer, E.W.; Stupp, S.I. *Science* **2012**, *335*, 813-817.
55. Korevaar, P.A.; George, S.J.; Markvoort, A.J.; Smulders, M.M.J.; Hilbers, P.A.J.; Schenning, A.P.H.J.; De Greef, T.F.A.; Meijer, E.W. *Nature* **2012**, *481*, 492-496.
56. Greef, T.F.A.; Smulders, M.M.J.; Wolffs, M.; Schenning, A.P.H.J.; Sijbesma, R.P.; Meijer, E.W. *Chem. Rev.* **2009**, *109*, 5687-5754.

57. Leenders, C.M.A.; Mes, T.; Baker, M.B.; Koenigs, M.M.E.; Besenius, P.; Palmans, A.R.A.; Meijer, E.W. *Mater. Horiz.* **2014**, *1*, 116-120.
58. Ouchi, M.; Badi, N.; Lutz, J.F.; Sawamoto, M. *Nat. Chem.* **2011**, *3*, 917-924.
59. Terashima, T.; Mes, T.; Greef, T.F.A.; Gillissen, M.A.J.; Besenius, P.; Palmans, A.R.A.; Meijer, E.W. *J. Am. Chem. Soc.* **2011**, *133*, 4742-4745.
60. Jacques, D.A.; Trehwella, J. *Protein Sci.* **2010**, *19*, 642-657.
61. Putnam, C.D.; Hammel, M.; Hura, G.L.; Tainer, J.A. *Q. Rev. Biophys.* **2007**, *40*, 191-285.
62. Petoukhov, M.V.; Franke, D.; Shkumatov, A.V.; Tria, G.; Kikhney, A.G.; Gajda, M.; Gorba, C.; Mertens, H.D.T.; Konarev, P.V.; Svergun, D.I. *J. Appl. Cryst.* **2012**, *45*, 342-350.

Chapter 2

Blocking rapid ice crystal growth through non-basal plane adsorption of antifreeze proteins

Abstract

Controlling ice crystal growth is a grand scientific challenge with major ramifications for a broad range of products and technologies. Some cold-adapted organisms such as fish and arthropods effectively avoid freezing by producing antifreeze proteins (AFPs) which adsorb onto endogenous embryonic ice crystals, which inhibits their growth. On a macroscopic level, this results in ice shaping, inhibition of ice recrystallization (IRI), and non-colligative freezing point depression which gives rise to thermal hysteresis (TH). In this study, we compare the TH and IRI activity of all major classes of AFPs, which reveals that binding to non-basal lattice planes is crucial to arrest fast ice-crystal growth. By contrast, binding to basal planes can be detrimental as it reduces the concentration of bound AFPs to the far more relevant prism planes. These novel insights into the working mechanism of AFPs may accelerate the development of innovative strategies for cryoprotection, cryopreservation, and anti-icing technologies.

This work has been submitted for publication:

Olijve, L.L.C.; Meister, K.; DeVries, A.L.; Duman, J.G.; Guo, S.; Bakker, H.J.; Voets, I.K.
(*submitted*)

2.1 Introduction

Ice formation is often detrimental for the structural integrity and performance of materials. The quality of frozen foods deteriorates when large ice crystals form upon prolonged low-temperature storage¹ and the consistency of water-based latex paints is irreversibly destroyed upon partial freezing.² Hypothermic storage effectively extends the preservation period of human organs, although freezing and freeze damage pose a considerable risk.³ Furthermore, icing of air-plane wings and wind turbine rotor blades is costly as well as dangerous; methane gas hydrate plugs impede oil and gas flows in pipelines; and frost weathering promotes unraveling of asphalt roads and pavements. Hence, a better understanding of ice crystal growth modifiers could support innovative strategies for cryoprotection, cryopreservation, de-icing, and anti-icing technologies.

Well-known classes of macromolecular ice crystal growth modifiers are antifreeze proteins (AFPs). AFPs enable various organisms, such as Antarctic fish to avoid freezing in ice-laden habitats at subzero temperatures.⁴ The efficacy of AFPs in freeze-protection is reflected in the wide distribution of AFPs among different biological kingdoms,⁵⁻⁷ and the benefits of their cryoprotective function have already found application in the hypothermic preservation of human blood cells⁸ and rat heart transplants,⁹ in the improvement of the texture of ice cream,¹⁰ and in the enhancement of the freeze-tolerance of crop plants.¹¹ Unlike their name suggests, AFPs do not prevent freezing in a colligative manner at physiological concentrations. Instead, AFPs recognize embryonic ice crystals in vast excess (55 M) of liquid water, and by binding onto specific crystal planes prevent further ice growth.¹² Based on their origin and structure, AFPs are categorized into different classes which are illustrated in Figure 1. Ice-etching assays demonstrate that different AFPs also target different – sometimes multiple – ice crystal planes, including prism, pyramidal and basal faces (Figure 1).¹³

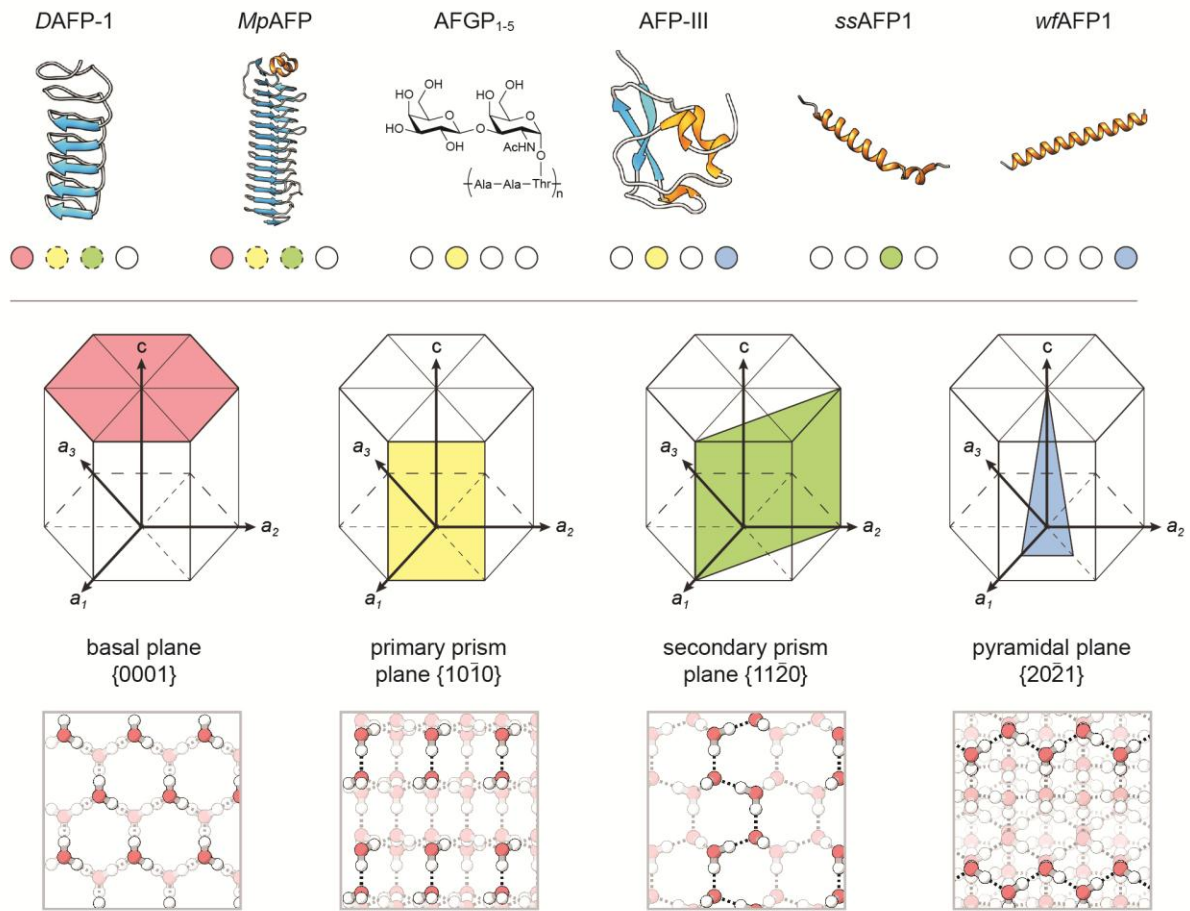


Figure 1: Overview of antifreeze proteins used in this study and their corresponding ice crystal binding plane (top row). AFPs are structurally very diverse and are found in a wide variety of organisms (*DAFP-1*: beetle *Dendroides canadensis*, *MpAFP*: Antarctic bacterium *M. primoryensis*, *AFGP₁₋₅*: various species of cod and notothenioid icefishes, *AFP-III*: ocean pout fish, *ssAFP1*: shorthorn sculpin fish, *wfAFP1*: winter flounder fish). Virtually all natural ice on earth is hexagonal ice (Ih). The AFPs adsorb to different ice planes, such as the slow growing basal plane and the faster growing prismatic fronts. The distinct growth rates appear to be correlated with the extent of the hydrogen-bonded water molecular network on the surface of the ice planes, as illustrated in the cartoon (lower panels). Red spheres represent oxygen atoms, white spheres represent hydrogen atoms, and dashed lines indicate hydrogen bonding.

AFPs exhibit two forms of activities. Well-known is the thermal hysteresis (TH) activity of AFPs, which is the ability of AFPs to lower the temperature at which existing ice crystals start to grow quickly. This threshold temperature at which ‘burst growth’ occurs is known as the non-equilibrium freezing point. The difference between the melting point and the non-equilibrium freezing point of a solution is defined as TH activity, and is commonly determined by viewing the melting and growth of single ice crystals using a nanoliter cryoscope.¹⁴ AFGPs and AFPs of fish usually exhibit a maximal TH of approximately 2 °C and are termed moderately active AFPs, whereas some insect AFPs can exhibit TH of over 5 °C and are referred to as hyperactive AFPs (hypAFPs). A unified understanding of the underlying mechanism that causes the large differences in thermal hysteresis is still lacking, but it appears that the targeted ice planes play a crucial role.¹⁵

The other activity of AFPs is the inhibition of the recrystallization of ice, which is a disproportionation process during which large ice crystals grow at the expense of small crystals. This mode of activity is referred to as ice recrystallization inhibition (IRI) activity and is defined as the visible deceleration of a change in ice texture during an annealing process just below the melting temperature of the sample.¹⁶⁻¹⁸ Recrystallization of ice involves both the nucleation of new ice crystals (or grains) and grain boundary migration,¹⁶ in which large ice crystals increase in size and small crystals disappear. AFPs inhibit grain boundary migration by stopping ice from growing and melting at the boundaries.¹⁹⁻²⁰ IRI is already significant at sub-micromolar AFP concentrations²¹ and ice crystals are maintained small in supercooled solutions, which is essential for survival in the cold and the preservation of frozen foods and other frozen hydrated materials.²²

Despite great progress in understanding TH and IRI activity of AFPs, the relation between these activities is still highly debated.²³⁻²⁶ Nonetheless, visual examination of crystals in the presence of AFPs^{27,28} as well as ice etching¹³ showed that direct ice-binding plays a crucial role in both types of activity. Further exploitation of ice crystal growth modulation by macromolecular antifreezes in industrial applications may lead to the development of inexpensive synthetic and polymeric material that can enhance or outperform its natural counterpart.²⁹ However, rational design of such a material can only be achieved if the underlying antifreeze function of AFPs is completely understood. Detailed knowledge on the specific adsorption to different ice planes and its relation to TH and IRI activity, thereby identifying how the TH and IRI activities are correlated, is crucial before AFPs will become widely applicable.

In this work, we investigate the antifreeze activity all major classes of AFPs via a comprehensive comparison of nanoliter cryoscopy, sonocrystallization and IRI activity assays. Nanoliter cryoscopy is the most commonly used method to measure the TH activity of AFPs.¹⁴ In cryoscopy, a nanoliter aqueous sample droplet is directly observed via a microscope. The sample solution is first flash-frozen and then melted back until a small single ice crystal is

obtained. Samples are then further cooled at a very slow rate, until the ice starts to grow in a sudden burst. The TH determined in this manner is defined as the difference between the melting point and the ice burst-growth temperature (i.e., the non-equilibrium freezing point). The major advantage of nanoliter cryoscopy is that a single measurement requires only several nanoliters of AFP solution. However, factors such as cooling and melting rate, annealing time and initial crystal size affect the determination of the TH activity.³⁰ To overcome these limitations, Gaede-Koehler et al. developed a highly accurate, time-independent method based on sonocrystallization to determine TH activity.³¹ In sonocrystallization, a sample solution is slowly supercooled until approximately -6 °C, after which ice nucleation is induced by a short ultrasound pulse resulting in a completely frozen sample solution. Slowly melting the sample allows for the determination of freezing and melting point within a single experiment. The sonocrystallization method provides control of the supercooling time and rate, excludes any observer-based bias, and is independent of initial ice crystal size. However, because the sample solution is not directly observed under a microscope, no information is obtained on the ice crystal morphology. We emphasize that these two methods to determine TH activity do so in a different manner: while cryoscopy involves slow cooling of an ice crystal until a sudden ice burst-growth is observed, sonocrystallization relies on slow melting of a rapidly frozen sample to determine the freezing and melting plateaus via direct readout of a thermocouple.

Besides cryoscopy and sonocrystallization, which are both used to assay the TH activity, the IRI activity of AFPs involves the observation of the ice recrystallization process of a thin wafer of sample solution by a polarized optical microscope. IRI is determined qualitatively as the threshold concentration below which no inhibition of the ice recrystallization process is apparent in consecutive polarized optical microscopy images taken at regular time intervals. Our results show a direct correlation between the specific planes to which AFPs adsorb on one hand and the TH activity measured using the sonocrystallization method and the IRI activity on the other hand. Using the sonocrystallization assay we find that basal plane binding in addition to prismatic and pyramidal plane binding does not give rise to higher TH activity. This finding contrasts to the TH activity based on nanoliter cryoscopy, that is highest for hyperactive (insect) AFPs that bind to both basal and non-basal planes. This apparent contradiction is due to the longer exposure time of nascent ice crystals to AFPs at a low ice volume fraction in cryoscopy as compared to sonocrystallization and IRI assays. We conclude that adsorption of AFPs to fast-growing prismatic and pyramidal ice planes (provided there is sufficient surface coverage) is decisive for both TH and IRI activity during a rapid ice growth process. In this scenario, there is a diminished role for basal plane binding, which becomes relevant only under conditions of very slow ice growth. These insights provide a deeper understanding of how AFPs arrest ice crystal growth, which is essential for the knowledge-based design of polymeric mimics and the development of freeze resistant soft materials.

2.2 Results

2.2.1 Freezing point determination using the sonocrystallization method

Figure 2 shows a typical sonocrystallization measurement of an aqueous solution of the recombinant QAE isoform of AFP-III (rQAE). After initiation of ice-nucleation by a short ultra-sound pulse, latent heat is released followed by the development of a stable freezing plateau. Slow melting of the sample allows the determination of the thermal hysteresis gap (Figure 2B) with high reproducibility (Figure 3). The TH activity of recombinant rQAE and AFP-III from a natural source (*op*AFP-III) is proportional to the square-root of the molar concentration (Figure 2C), which is in accordance with cryoscopy data.³² rQAE is slightly more active than *op*AFP-III due to the presence of inactive isoforms in the purified extract. We further determined the activity of rQAE mutants, proving that single mutations within the ice-binding site of the protein can have a marked impact on the TH activity, which underlines the delicate balance between the structure and activity of AFPs (Figure 4).

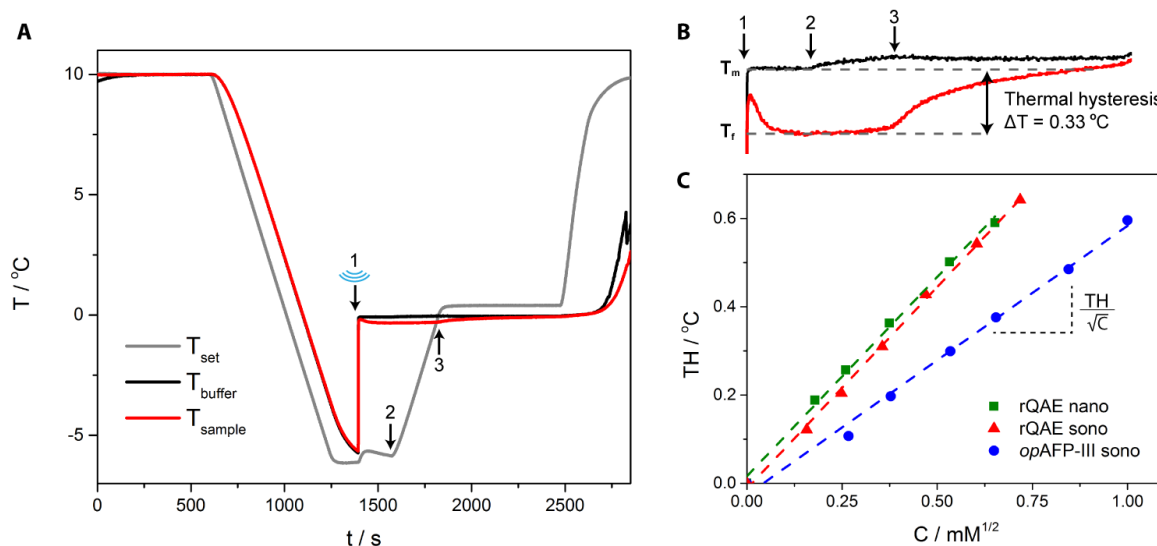


Figure 2: (A) Sonocrystallization measurement of the thermal hysteresis activity of recombinant type III AFP (rQAE, 1 mg/ml). The bold numbers indicate (1) application of the ultrasound pulse, (2) onset of heating and (3) cross-point where the set temperature passes the non-equilibrium freezing point of the sample. (B) Zoom-in of A, showing the development of freezing (T_f) and melting (T_m) plateaus. The TH is defined as the difference between the freezing point plateau of the buffer solution and the non-equilibrium freezing point of the AFP solution. The slight increase in temperature (~ 0.03 °C) of the buffer at point 2 is due to infrared irradiation from the heating unit after the onset of heating. (C) TH measurements of 0.025 – 1.0 mM solutions of type III AFP in cryoscopy (\blacksquare)³² and sonocrystallization (\blacktriangle , \bullet). rQAE is the recombinant expressed QAE-isoform (HPLC-12) and *op*AFP-III is from natural source (A/F Protein Inc.), which is a mixture of different isoforms. All samples were measured in 20 mM Tris, pH 7.5. The slope of the linear relation between TH (°C) and C ($\text{mM}^{1/2}$) gives the

ratio $\frac{TH}{\sqrt{c}}$ and is used as a measure to directly compare AFP activity of sonocrystallization with nanoliter cryoscopy.

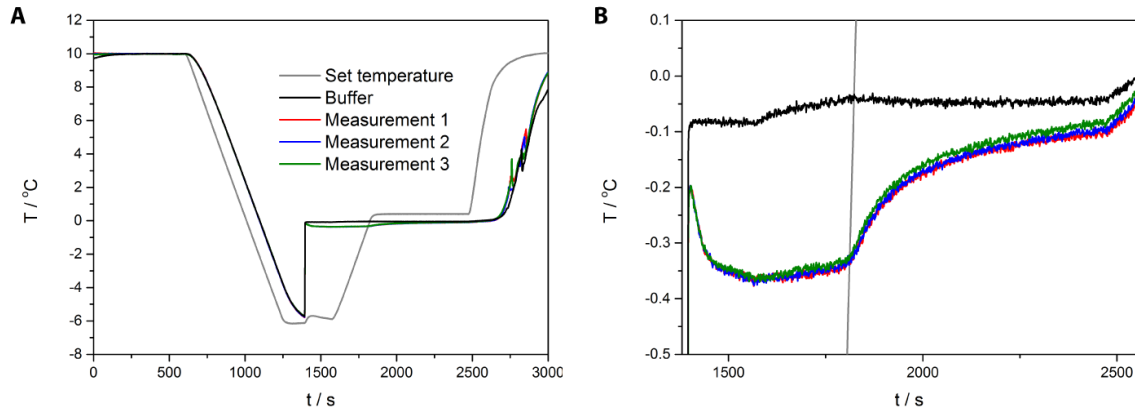


Figure 3: Triplo measurement of rQAE at a concentration of 1 mg/ml in 20 mM Tris, pH 7.5. The temperature read-out accuracy of the experimental set-up is within 0.01 °C. Measurements on the AFP samples have high reproducibility with a deviation in determining the non-equilibrium freezing temperature below < 0.02 °C.

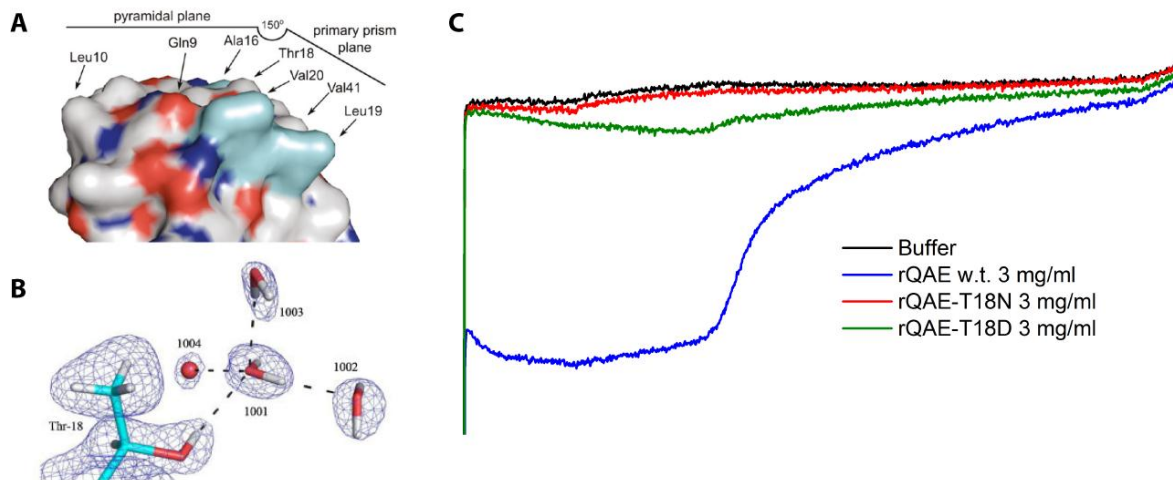


Figure 4: (A) Identified ice-binding face of type III AFP (QAE isoform), showing the central position of the Thr18 residue at the ice-binding face which recognizes the primary prism plane.³³ (B) Neutron crystal structure (PDB: 3QF6) shows the specific interaction of Thr18 with a tetrahedral water cluster.³⁴ (C) Sonocrystallization measurements of wild type rQAE and mutant rQAE with a single mutation on the Thr18 position. The T18D mutant shows a significant reduction in activity, while T18N has no freezing hysteresis activity at all. This shows that the adsorption of rQAE to the pyramidal or primary prism planes can be disrupted by a single mutation.

2.2.2 Activity ranking based on cryoscopy and sonocrystallization experiments

Table 1 shows the thermal hysteresis activities of six different AFPs obtained by nanoliter cryoscopy and sonocrystallization. The six AFPs vary significantly in terms of structure, putative ice-binding plane and TH activity. In cryoscopy, hyperactive *MpAFP* and *DAFP-1* show the highest maximum activities (TH = 5-6 °C) in accordance with their classification. Moderately active AFPs show comparable maximal activities with for instance TH = 0.6 °C for *wfAFP1* and *rQAE* at 5 and 3 mg/ml, respectively. These values are consistent with previously reported values for these proteins.^{32,35} However, in sonocrystallization, moderately active AFPs show TH ≤ 0.5 °C, while hyperactive AFPs exhibit TH ≤ 0.2 °C (Figure 5).

To directly compare the values for the thermal hysteresis activity from the two methods, we have determined the ratio $\frac{TH}{\sqrt{C}}$ corresponding to the slope of the linear relation between TH and the square root of the protein concentration as shown in Figure 2C and Figure 6. Ordering AFPs based on cryoscopy from the most to the least active gives: *MpAFP* (20.8) > *DAFP-1* (19.8) > *rQAE* (0.90) > *AFGP₁₋₅* (0.78) > *ssAFP1* (0.57) > *wfAFP1* (0.48). The ranking based on sonocrystallization is entirely different: *rQAE* (0.91) > *MpAFP* (0.85) > *AFGP₁₋₅* (0.48) > *DAFP-1* (0.32) > *ssAFP1* (0.13) > *wfAFP1* (0.07). Remarkably, the moderately active *rQAE* is in fact the most active AFP in the sonocrystallization assay with $\frac{TH_{sono}}{\sqrt{C}}$ equal to $\frac{TH_{nano}}{\sqrt{C}}$. Moreover, the hyperactive *MpAFP* is 25 times less active in sonocrystallization and shows only a small thermal hysteresis gap in sonocrystallization (Figure 5C). Also *DAFP-1* (0.32) displays a dramatic 62-fold decrease in activity. The small α -helical proteins *ssAFP1* (0.13) and *wfAFP1* (0.07) show only minimal activity in a sonocrystallization assay (Figure 5E-F).

Out of all investigated AFPs, only AFP-III and *AFGP₁₋₅* show a comparable TH activity in cryoscopy and sonocrystallization. Interestingly, ice etching revealed that both these proteins bind predominantly to the six equivalent $\{10\bar{1}0\}$ primary prism planes (Figure 1, Table 1). Ice etching studies on type I AFPs demonstrated binding of *wfAFP1* to the 12 equivalent $\{20\bar{2}1\}$ pyramidal planes and *ssAFP1* to the six equivalent $\{11\bar{2}0\}$ secondary prism planes. Most striking is the poor performance of hyperactive AFPs in sonocrystallization, even though these proteins have been reported to bind both prism and basal planes. This dual recognition is thought to be the basis for their hyperactive nature.^{15,36}

Table 1: Thermal hysteresis (TH) and ice recrystallization inhibition (IRI) activity of AFPs from nanoliter cryoscopy, sonocrystallization, and polarized optical microscopy measurements. The ratio $\frac{TH}{\sqrt{C}}$ is used as a quantitative measure of TH activity. It corresponds to the slope of the curve that describes the TH as a function of the square-root of the protein concentration as illustrated in Figure 2C. C_{IRI} is the lowest AFP concentration where IRI activity is observed (Figure 7). The tabulated cryoscopy values are from this work for rQAE, AFGP₁₋₅, DAFP-1 and from literature for wfAFP1,³⁷ MpAFP,³⁸ and ssAFP1.³⁹

	$\frac{TH_{nano}}{\sqrt{C}}$ (°C mM ^{-1/2})	$\frac{TH_{sono}}{\sqrt{C}}$ (°C mM ^{-1/2})	Ice crystal binding plane	$C_{IRI} < 10 \mu\text{M}$
rQAE	0.90	0.91	{10 $\bar{1}$ 0} Primary prism and {20 $\bar{2}$ 1} pyramidal planes ⁴⁰	Yes
AFGP ₁₋₅	0.78	0.48	{10 $\bar{1}$ 0} Primary prism planes ^{41,42}	Yes
MpAFP	20.8	0.85	Prism and basal planes ⁴³	Yes
DAFP-1	19.8	0.32	Prism and basal planes ⁴⁴	No
ssAFP1	0.57	0.13	{11 $\bar{2}$ 0} Secondary prism planes ¹³	No
wfAFP1	0.48	0.07	{20 $\bar{2}$ 1} Pyramidal planes ¹³	Yes

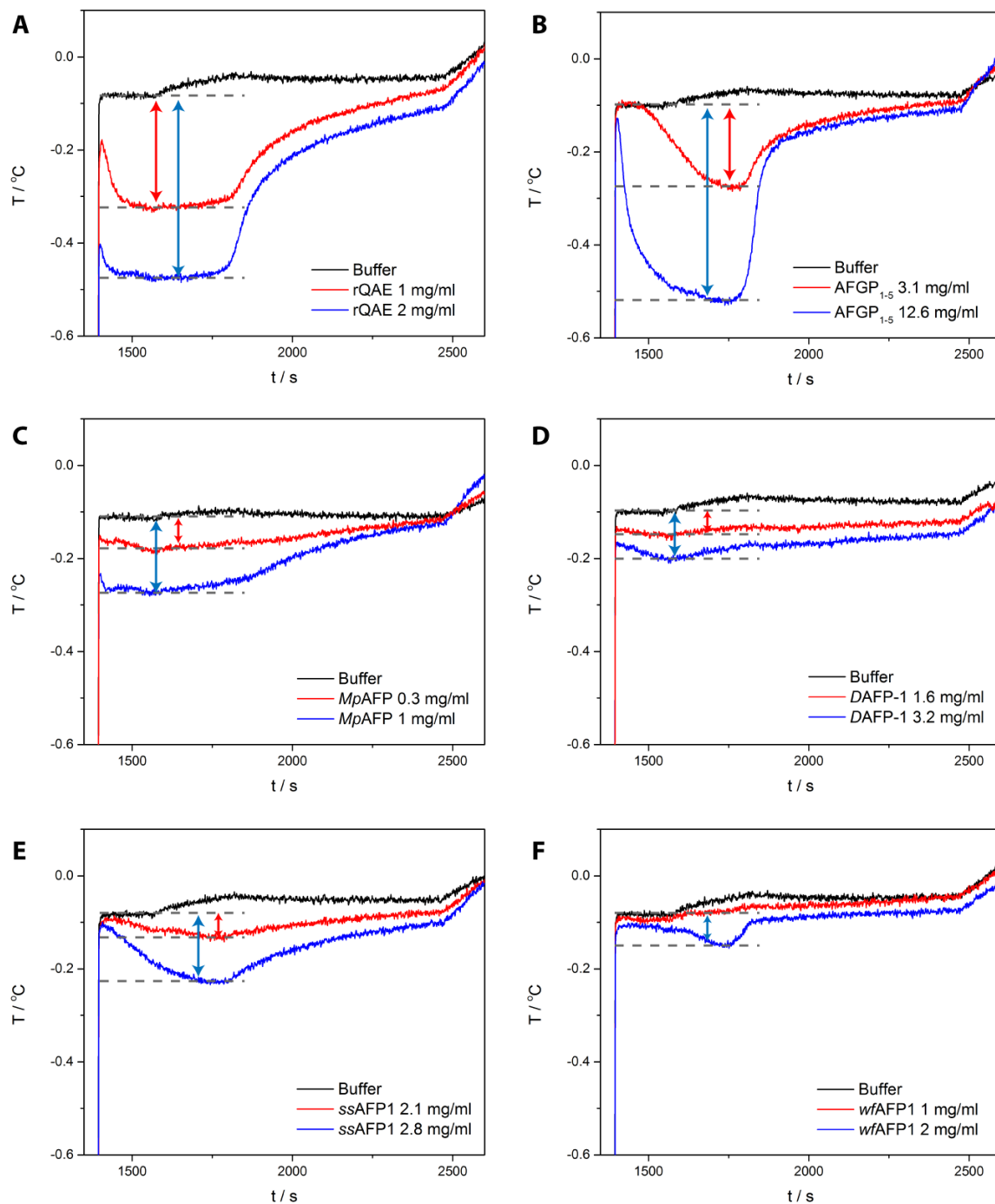


Figure 5: Sonocrystallization data of all AFPs. The freezing hysteresis gap is indicated by arrows. All proteins were measured in 20 mM Tris buffer, pH 7.5, except *MpAFP* which was measured in 20 mM Tris buffer and 2 mM CaCl₂, pH 7.5.

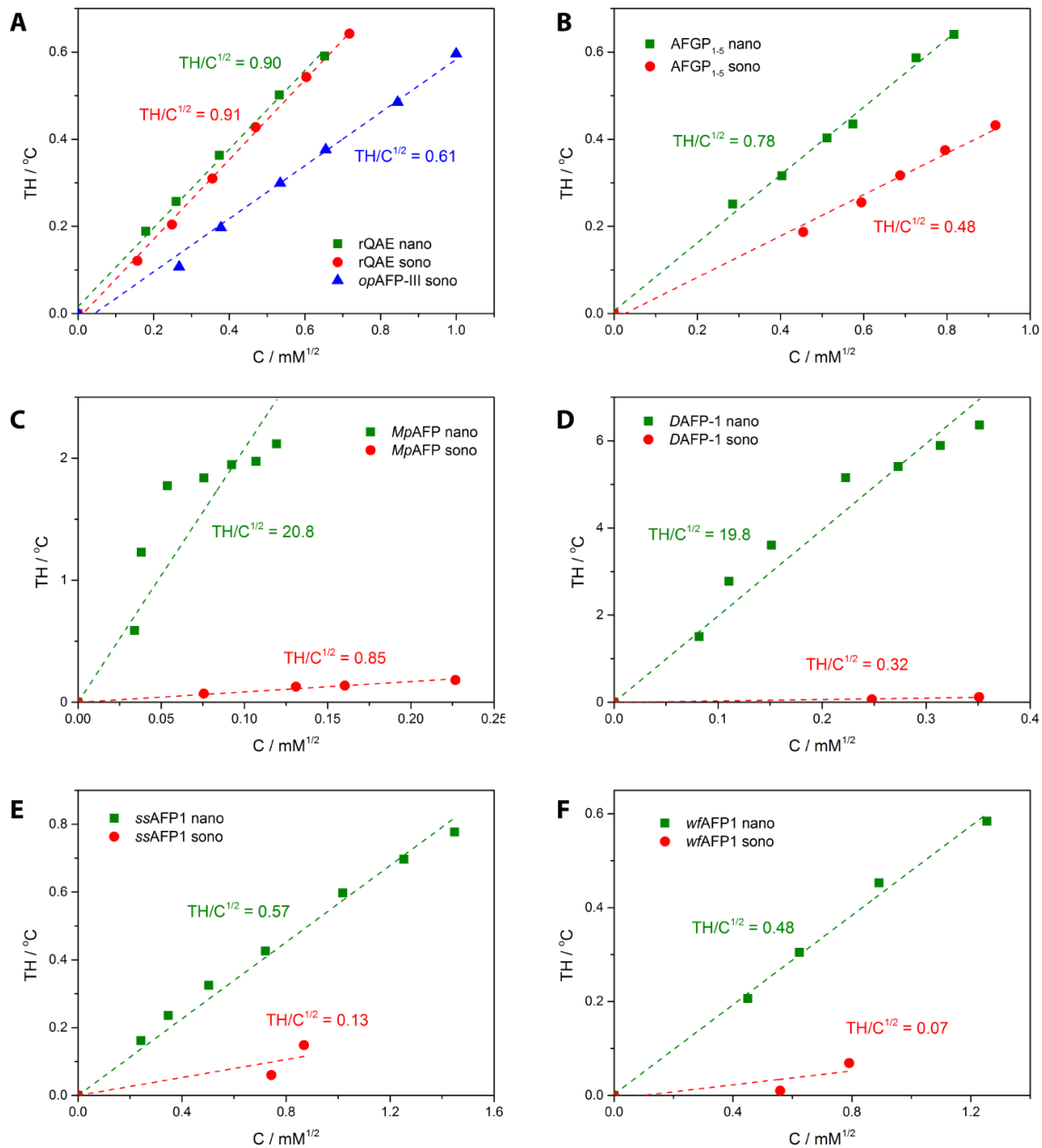


Figure 6: Concentration dependent TH activity from sonocrystallization and nanoliter cryoscopy. Dashed line illustrate a linear fit of the data points, of which the slope gives the ratio $\frac{TH}{\sqrt{C}}$ and is used as a measure to directly compare AFP activity of sonocrystallization with cryoscopy. An average molecular weight ($M_w = 15$ kDa) was assumed to compute the molar concentration of AFGP₁₋₅.

2.2.3 Sonocrystallization TH activity correlates to IRI activity

All investigated AFPs with confirmed TH activity show IRI activity at low (μM) concentrations, even the AFPs that show only minimal $\frac{TH_{\text{sono}}}{\sqrt{C}}$ activity (Table 1, Figure 7). IRI activity is observed below an AFP concentration of $10 \mu\text{M}$ for rQAE, AFGP₁₋₅, MpAFP and wfAFP1, whereas DAFP-1 and ssAFP1 are slightly less active, which is in good agreement with other studies.^{18,23,24} Especially striking is the fact that the hyperactive DAFP-1 with 20 to 40-fold higher $\frac{TH_{\text{nano}}}{\sqrt{C}}$ activities than the moderate active antifreeze proteins rQAE and wfAFP1, shows lower IRI activity. This contradictory observation has also been noted by other groups.^{23,24} The present direct comparison of the TH and IRI activity of all major classes of AFPs shows that $\frac{TH_{\text{sono}}}{\sqrt{C}}$ and IRI based activity rankings are highly similar, while cryoscopy yields an entirely different order. This clearly underlines the importance of sonocrystallization as a complementary thermal hysteresis assay for macromolecular antifreezes in addition to cryoscopy.

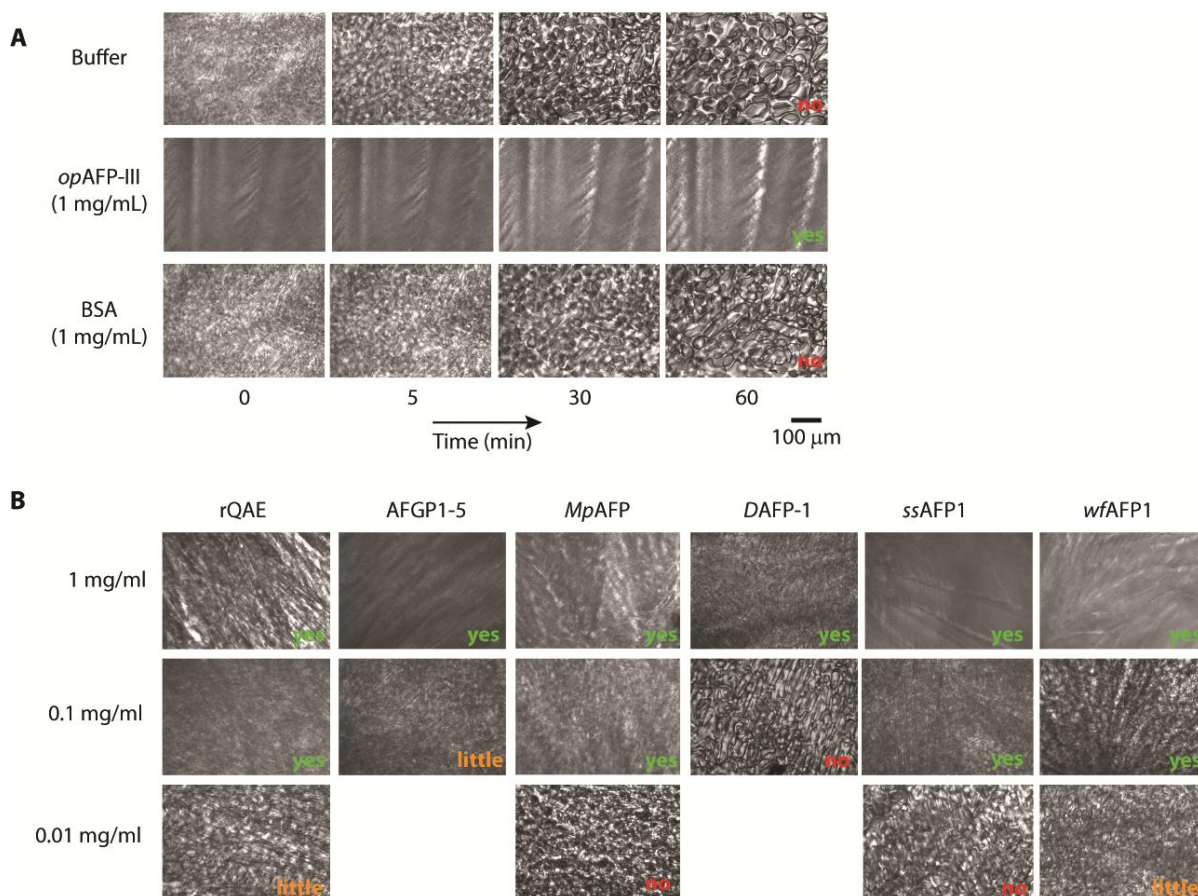


Figure 7: (A) Ice-recrystallization inhibition (IRI) measurements of buffer solution, type III AFP from natural source (*op*AFP-III), and bovine serum albumin (BSA) as control. Positive IRI activity is defined as no visible change in ice texture during the 1 h annealing period at $-6 \text{ }^{\circ}\text{C}$. (B) IRI measurements of all major classes of AFPs after 1 h annealing at $-6 \text{ }^{\circ}\text{C}$. The lowest molar concentration where IRI activity is observed (in μM): rQAE (1.4), AFGP₁₋₅ (6.4),

MpAFP (3), *DAFP-1* (40), *ssAFP1* (27), *wfAFP1* (3). All samples were measured in 20 w/w% sucrose.

2.3 Discussion

In this study, we report on nanoliter cryoscopy, sonocrystallization and ice-recrystallization inhibition experiments on all major classes of AFPs to investigate the factors that govern both TH and IRI activity. Using $\frac{TH}{\sqrt{C}}$ as a quantitative measure for TH activity, we have ranked AFPs by sonocrystallization to $rQAE > MpAFP > AFGP_{1-5} > DAFP-1 > ssAFP1 > wfAFP1$. This is well aligned with IRI activity, but differs significantly from the ranking based on cryoscopy. Notably, the $\frac{TH_{sono}}{\sqrt{C}}$ based ranking seems related to more than IRI activity alone - it appears to correlate with the ice-crystal binding plane of the antifreeze proteins. All AFPs that bind predominantly to prismatic planes (*rQAE*, *AFGP₁₋₅*, *MpAFP* and *DAFP-1*) give a significant non-colligative freezing point depression in sonocrystallization; these are ranked 1 to 4 out of 6. AFPs that solely target the secondary prism (*ssAFP1*) or pyramidal planes (*wfAFP1*) show on molar basis very little activity. Furthermore, only AFPs that predominantly bind to primary prism planes (*rQAE*, *AFGP₁₋₅*) exhibit highly similar activity in cryoscopy and sonocrystallization. Surprisingly, “hyperactive” AFPs perform poorly in sonocrystallization with a 25-fold (*MpAFP*) and 62-fold (*DAFP-1*) lower $\frac{TH_{sono}}{\sqrt{C}}$, which is even lower than the activity of the “moderate” *rQAE*. Adsorption of hyperactive AFPs onto both prism and basal planes has been suggested to enhance their ability to depress the non-equilibrium freezing point, making them more potent than their moderately active counterparts which target a single, non-basal ice crystal plane.¹⁵ Our findings clearly demonstrate that primary prism plane binding is a far more important determinant of $\frac{TH_{sono}}{\sqrt{C}}$ than basal-plane binding. This raises the question: why are ‘hyperactive’ AFPs potent in cryoscopy yet inefficient in sonocrystallization? We propose that the binding of the hyperactive AFPs to basal planes reduces their accumulation onto the prism planes. As a result, the concentration of hyperactive proteins onto prism planes is too limited to block rapid ice growth along this fast ice-growth direction.

The initiation of ice crystallization in a sonocrystallization assay results from many nucleation sites and ice growth is very fast. The most favorable and fastest growing ice lattice direction is along the *a*-axis direction $\{11\bar{2}0\}$.^{13,45} Therefore, binding to prism planes is crucial, as only adsorption onto this plane blocks the predominant growth mode. Ice grows fastest along the *a*-axis direction, because here, chains or networks of water molecules can cooperatively hydrogen bond to the ice-lattice, having one hydrogen bond per water molecule to attach to the ice surface. The frontal views of the specific ice crystal planes depicted in Figure 1 illustrate how the extensive hydrogen-bonding network of the water molecules in the ice-lattice favors

the attachment of new water molecules. Ice grows fast, but less fast, along the $\{10\bar{1}0\}$ direction since only pairs of water molecules can attach here, having one hydrogen bond per two water molecules interact with the ice surface. Ice growth along the c -axis requires two dimensional nucleation on the molecularly smooth basal plane, which makes ice growth there slow. HypAFP adsorption onto the slowly growing basal planes is thus irrelevant at moderate supercooling when rapid ice growth proceeds mainly by addition of water molecules at the prism planes. Ice-etching shows that hypAFPs also adsorb here, but little is known about the surface coverage.⁴⁶ We speculate that this adsorption leads to insufficiently high surface coverage to elicit significant activity. This may also explain why *ssAFP1* has only minor thermal hysteresis in sonocrystallization despite binding to the fast growing secondary prism planes.

A complete arrest of ice growth requires a sufficiently high surface coverage which is attainable if the rate of AFP adsorption (which is directly related to the AFP concentration in solution) is fast compared to the growth rate of the ice crystal plane.⁴⁷ If the AFP concentration and/or the AFP adsorption rate are too low, ice-bound proteins will get engulfed. Relatively slow AFP adsorption at the basal planes becomes relevant only during prolonged annealing at modest supercooling and thus modest ice growth rates. The large values of thermal hysteresis in nanoliter cryoscopy assays arise due to long exposure times at slow cooling rates and modest supercooling, which accommodates slow hypAFP adsorption onto basal planes. By contrast, ice growth is very rapid during a sonocrystallization assay at several degrees of supercooling, which warrants fast and significant AFP accumulation at the primary prism planes to arrest ice growth. Ice etching assays demonstrate that both rQAE and hypAFP adsorb onto prism planes, and a recent fluorescence study by Drori *et al.* reports similar adsorption rates for rQAE and *MpAFP* at the prism plane.⁴⁸ Apparently, rQAE accumulates at sufficiently high coverage on the prism plane to block rapid growth, whereas the amount of bound *MpAFP* does not exceed the required threshold to prevent engulfment.

The discrepancy between IRI and TH activity determined by cryoscopy still remains to be explained.²³ Particularly striking is the high TH yet low IRI activity of hyperactive proteins. The insights based on our sonocrystallization assays offer a way to reconcile this difference. As in sonocrystallization assays, ice growth in IRI experiments is initially very fast since growth is typically nucleated at $-40\text{ }^{\circ}\text{C}$. AFPs thus have to bind rapidly onto the fast-growing ice planes and produce sufficiently high surface coverage. Only then AFPs can inhibit recrystallization into larger ice crystals by interfering with migration processes of water molecules at the grain boundaries, which is the proposed mechanism of IRI by AFPs.^{Error! Reference source not found.,19,20} Slow basal plane binding of hypAFPs will result in (partial) engulfment which diminishes its inhibitory impact on the migration processes. Hence, rapid and strong prism plane binders inhibit ice-recrystallization most efficiently.

2.4 Conclusion

In conclusion, a comprehensive comparison of all major classes of AFPs shows that binding to fast-growing ice planes is a prerequisite for effective inhibition of ice-recrystallization and non-colligative freezing point depression at cooling rates favoring rapid ice growth. The so-called “hyperactive” AFPs that slowly accumulate on additional basal planes in fact perform less well than their “moderately” active counterparts, such as rQAE. The rapid adsorption of rQAE onto prism planes generates sufficiently high coverage to block ice growth in the fastest growth direction, which “hyperactive” AFPs fail to accomplish. These findings reveal that rational design strategies for synthetic ice-binders should not focus on compatibility with all ice crystal planes, but instead take into account that binding to fast-growing planes is essential. Furthermore, we propose to abandon the categorization of AFPs into moderate and hyperactive variants, as this is based on an activity ranking that is method- and protocol dependent. These new insights provide a deeper understanding of the underlying mechanism that governs IRI and TH activity, which supports the development of synthetic macromolecular antifreezes for cryoprotection, cryopreservation, de-icing, and anti-icing technologies.

2.5 Material and methods

Chemicals

(L)-Fmoc-protected amino acids and *O*-benzotriazole-*N,N,N',N'*-tetramethyl-uronium-hexafluoro-phosphate (HBTU) were purchased from Nova Biochem. Tentagel R RAM resin (loading 0.2 mmol/g) was purchased from Rapp Polymere. All other chemicals were reagent grade and used without further purification. All solvents used for RP-HPLC were HPLC grade.

Instrumentation

Mass spectroscopy was performed to determine the purity and exact mass of *wfAFP1* and *rQAE* using a Waters Xevo G2 Quadrupole Time of Flight (Q-ToF) Liquid Chromatography – Mass Spectrometry (LC-MS) with an Agilent Polaris C18A RP column, equipped with a ThermoScientific LCQ Fleet spectrometer with a Grace Smart RP-HPLC. Samples were measured at an approximate concentration of 0.1 mg/mL and deconvolution of the mass spectra was done using the MaxENT algorithm.

Solid phase peptide synthesis of wfAFP1

The HPLC-6 isoform of winter flounder type 1 AFP (*wfAFP1*) was synthesized by automated solid phase peptide synthesis on an Intavis Multi pep RSi peptide synthesizer using 9-fluorenylmethyl carbamate (Fmoc) protection chemistry. Synthesis was performed on a Tentagel R RAM resin to provide a C-terminal amidation, following the amino acid sequence as given by the crystal structure (PDB: 1WFA),⁴⁹ respectively: H-DTASDAAAAAALTAANAKAAAELTAANAAAAAATAR-CONH₂. Synthesis was performed on 200 μmol scale using double couplings of 1 h (8 eq. Fmoc-aa, 7.2 eq. HBTU, 16 eq. *N,N*-diisopropylethylamine (DIPEA)) with *N*-methylpyrrolidone (NMP) as solvent. The peptide was cleaved from the resin using trifluoroacetic acid (TFA)/ethanedithiol (EDT)/H₂O/triisopropylsilane (TIS) (92.5:2.5:2.5:2.5 v/v%) for 3 h, and precipitated into 30 mL cold diethylether:heptane (70:30 v/v%). The precipitate was centrifuged for 10 min at 2000 rpm and the pellet was washed with 30 mL of diethylether:heptane (70:30 v/v). Finally, the pellet was dried under vacuum, dissolved into acetonitrile (ACN)/H₂O and lyophilized. The peptide was purified by preparative reversed-phase (RP)-HPLC (Shimadzu HPLC) on a C18 column (Jupiter 5 μm C18 300 Å, LC Column, Phenomenex) using a gradient of 32-42 % ACN in H₂O with 0.1 v/v% TFA in 9 minutes, with a total flow rate of 20 mL/min and injection concentration of 3-5 mg/mL. Purity and exact mass were determined using Q-ToF mass spectroscopy.

Recombinant expression and purification of rQAE

The gene coding for type III AFP from ocean pout (*rQAE* isoform, M1.1HISPET20b)⁵⁰ was kindly provided by prof. Peter Davies (Queen's University, Kingston, Canada). The cDNA was

inserted in between the *NdeI/XhoI* restriction sites of the pET20b expression vector (Novagen) in frame with the His-tag sequence. The plasmid was transformed into competent *Escherichia coli* NiCo21(DE3) cells (New England Biolabs). Positive clones were selected and inoculated overnight at 37 °C and shaking at 250 rpm in a 25 mL pre-culture of LB-medium with 100 µg/mL ampicillin and 0.5 % glucose. The pre-culture was transferred to a 5 L culture flask and cells were grown in 1 L of ZYP-5052 auto-induction medium containing 100 µg/mL ampicillin at 37 °C under continuous shaking at 130 rpm.⁵¹ The temperature of the culture was reduced to 18 °C when OD_{600nm} reached 2-2.5, and overexpression of the protein was allowed overnight under shaking. Successful overexpression of the target protein was checked by SDS-PAGE. Cells were pelleted by centrifugation and lysed using BugBuster (Novagen) via 40 min shaking at room temperature. The cell lysate was spun down and the supernatant applied to a Ni-NTA agarose (Novagen) column equilibrated with bind buffer (20 mM Tris pH 8, 150 mM NaCl, 5 mM imidazole). The column was washed with four to five column volumes of wash buffer (20 mM Tris pH 8, 150 mM NaCl, 30 mM imidazole), and the protein was eluted with 400 mM imidazole. The fractions containing rQAE were collected and dialyzed overnight against 20 mM Tris pH 7.5 using 1 kDa MWCO dialysis membranes (Spectra/Por 6) and concentrated using 3 kDa Microsep Advance centrifugal devices (Pall). Purity was estimated by SDS-PAGE gel electrophoresis and the exact mass determined using Q-ToF mass spectroscopy. Protein concentration was determined by UV absorbance using the molar extinction coefficient $\epsilon_{280} = 1568 \text{ M}^{-1}\text{cm}^{-1}$ as reported in literature.⁵² Typical yields per liter of culture medium were ~ 80 mg.

Other protein samples

Recombinant expression and purification of DAFP-1⁵³ and MpAFP⁴³ was performed as described previously ssAFP1 was purified from shorthorn sculpin blood using gel filtration chromatography, AFGP₁₋₅ were obtained by ion exchange purification from Antarctic toothfish blood. opAFP-III was purchased from A/F Protein Inc. and used without further purification.

Thermal hysteresis

The Clifton nanoliter cryoscopy were performed as described elsewhere.³⁷ The sonocrystallization set-up was built according to the original design by Grunwald *et al.*³¹ The temperature-controlled sample chamber consist of a heating unit positioned inside an aluminum cooling block (CB), which is cooled using an external cooling bath (Julabo CF40) with 50/50 v/v% ethanol/water as coolant to -16 °C. The heating unit (HU) consists of a copper coil wrapped around a copper tube. Temperature is controlled by applying energy to the heating wire via an adjustable power supply unit. The sample (0.8-1 mL) is loaded in a 2 mL Eppendorf and inserted into the copper tube. A PTFE-coated stirring bar was inserted to ensure a homogenous temperature through the whole sample. Two Pt-100 resistance thermometers (JUMO, PG 1.0910.1) are used in the set-up, one inserted into the heating unit (T1) used to

control the temperature of the chamber, and the other inserted into the sample tube (T2) to monitor the heating profile of the sample. To ice crystallization is initiated by the application of a short ultrasound pulse (100 ms, 30 % amplitude) via the sonotrode (SONICS; VCX 130PB) inserted 0.5 cm deep into the sample. The temperature sensor (T2) inserted in to the sample was calibrated using an osmolality linearity set (Advanced Instruments) with five solution concentrations (0, 100, 250, 500 and 750 mOsm kg⁻¹) such that the difference between the calculated and measured freezing point of the solutions was within 0.02 °C. The temperature sensor of the heating unit (T1) was adjusted accordingly. Thermal hysteresis is determined from the T2 values at the two plateaus that develop upon setting T1 to -6 °C and 0.4 °C in a temperature ramp consisting of six steps. The starting temperature of each ramp is 10 °C (step 1), after which T1 is reduced to -6 °C at a rate of 1.5 °C/min (step 2). A short ultrasound pulse is hereafter applied and the temperature is held at 6 °C for 300 s (step 3), after which T1 is raised to 0.4 °C at a rate of 1.5 °C/min and kept constant at 0.4 °C for 650 s (step 5). Finally, T1 is further increased to the initial temperature of 10 °C (step 6). Throughout the temperature ramp, data are recorded using a home-written LabView program. All sonocrystallization samples were measured in 20 mM Tris, pH 7.5 buffer, except *MpAFP* which was measured in 20 mM Tris and 2 mM CaCl₂, pH 7.5 buffer. Protein concentrations were chosen in the 0.5 – 5 mg/mL range.

Ice-recrystallization inhibition

Polarized optical microscopy was used to evaluate whether the samples inhibit ice-recrystallization. Experiments were carried out on a Jeneval polarization microscope equipped with a Linkam THMS 600 heating device operating in transmission (bright field) mode. Samples were prepared in ultra pure water and measured in pre-filtered 20 w/w% sucrose, following the protocol described by Budke *et al.*¹⁷ Sample droplets (2 µL) were placed between two 12 mm coverslips (12 mm, Menzel Gläser) with a SecureSeal imaging spacer (9 mm ID, 0.12 mm depth, 18 mm × 18 mm OD, Grace Biolabs). Samples were placed on a temperature-controlled silver block inside the Linkam stage under a nitrogen stream to avoid water condensation from ambient air during the experiment. During the experiment, a sample is rapidly cooled to -40 °C at a rate of 20 °C/min to produce polycrystalline ice and held for 5 min at -40 °C. The frozen sample is then heated at the same rate to the annealing temperature of -6 °C where it is held for 60 min. Images were recorded at regular time intervals (0, 5, 30 and 60 min) at a magnification of 16× using a CMOS digital video camera (DFK 72AUC02, Imaging Source) at a resolution of 2592 × 1944.

2.6 References

1. Petzold, G.; Aguilera, J.M. *Food Biophys.* **2009**, *4*, 378-396.
2. Zhao, C.L.; Porzio, S.; Smith, A.; Ge, H.; Davis, H.T.; Scriven, L.E. *J. Coating. Tech. Res.* **2006**, *3*, 109-115.
3. Berendsen, T.A.; Bruinsma, B.G.; Puts, C.F.; Saeidi, N.; Usta, O.B.; Uygun, B.E.; Izamis, M.L.; Toner, M.; Yarmush, M.L.; Uygun, K. *Nat. Med.* **2014**, *20*, 790-793.
4. DeVries, A.L.; Wohlschlag, D.E. *Science* **1969**, *163*, 1073-1075.
5. Fletcher, G.L.; Hew, C.L.; Davies, P.L. *Annu. Rev. Physiol.* **2001**, *63*, 359-390.
6. Duman, J.G. *Annu. Rev. Physiol.* **2001**, *63*, 327-357.
7. Davies, P.L. *Trends Biochem. Sci.* **2014**, *39*, 548-555.
8. Deller, R.C.; Vatish, M.; Mitchell, D.A.; Gibson, M.I. *Nat. Commun.* **2014**, *5*, 3244.
9. Amir, G.; Rubinsky, B.; Horowitz, L.; Miller, L.; Leor, J.; Kassif, Y.; Mishaly, D.; Smolinsky, A.K.; Lavee, J. *Ann. Thorac. Surg.* **2004**, *77*, 1648-1655.
10. Regand, A.; Goff, H.D. *J. Dairy Sci.* **2006**, *89*, 49-57.
11. Worrall, D.; Elias, L.; Ashford, D.; Smallwood, M.; Sidebottom, C.; Lillford, P.; Telford, J.; Holt, C.; Bowles, D. *Science* **1998**, *282*, 115-117.
12. Sharp, K.A. *J. Chem. Phys.* **2014**, *141*, 22D510.
13. Knight, C.A.; Cheng, C.C.; DeVries, A.L. *Biophys. J.* **1991**, *59*, 409-418.
14. Knight, C.A.; DeVries, A.L.; Oolman, L.D. *Nature* **1984** *308*, 295-296.
15. Scotter, A.J.; Marshall, C.B.; Graham, L.A.; Gilbert, J.A.; Garnham, C.P.; Davies, P.L. *Cryobiology* **2006**, *53*, 229-239.
16. Knight, C.A.; Duman, J.G. *Cryobiology* **1986**, *23*, 256-262.
17. Budke, C.; Heggemann, C.; Koch, M.; Sewald, N.; Koop, T. *J. Phys. Chem. B* **2009**, *113*, 2865-2873.
18. Budke, C.; Dreyer, A.; Jaeger, J.; Gimpel, K.; Berkemeier, T.; Bonin, A.S.; Nagel, L.; Plattner, C.; DeVries, A.L.; Sewald, N.; Koop, T. *Cryst. Growth Des.* **2014**, *14*, 4285-4294.
19. Knight, C.A.; Hallett, J.; DeVries, A.L. *Cryobiology* **1988**, *25*, 55-60.
20. Knight, C.A.; Wen, D.; Laursen, R.A. *Cryobiology* **1995**, *32*, 23-34.
21. Tomczak, M.M.; Marshall, C.B.; Gilbert, J.A.; Davies, P.L. *Biochem. Biophys. Res. Commun.* **2003**, *311*, 1041-1046.
22. Venketesh, S.; Dayananda, C. *Crit. Rev. Biotechnol.* **2008**, *28*, 57-82.
23. Yu, S.O.; Brown, A.; Middleton, A.J.; Tomczak, M.M.; Walker, V.K.; Davies, P.L. *Cryobiology* **2010**, *61*, 327-334.
24. Capicciotti, C.J.; Poisson, J.S.; Boddy, C.N.; Ben, R.N. *Cryobiology* **2015**, *70*, 79-89.
25. Sidebottom, C.; Buckley, S.; Pudney, P.; Twigg, S.; Jarman, C.; Holt, C.; Telford, J.; McArthur, A.; Worrall, D.; Hubbard, R.; Lillford, P. *Nature* **2000**, *406*, 256.
26. Singh, P.; Hanada, Y.; Singh, S.M.; Tsuda, S. *FEMS Microbiol. Lett.* **2014**, *35*, 14-22.

27. Pertaya, N.; Marshall, C.B.; DiPrinzio, C.L.; Wilen, L.; Thomson, E.S.; Wettlaufer, J.S.; Davies, P.L.; Braslavsky, I. *Biophys. J.* **2007**, *92*, 3663-3673.
28. Celik, Y.; Drori, R.; Pertaya-Braun, N.; Altan, A.; Barton, T.; Bar-Dolev, M.; Groisman, A.; Davies, P.L.; Braslavsky I. *Proc. Natl. Acad. Sci. USA* **2013**, *110*, 1309-1314.
29. Gibson, M.I. *Polym. Chem.* **2010**, *1*, 1141-1152.
30. Takamichi, M.; Nishimiya, Y.; Miura, A.; Tsuda, S. *FEBS* **2007**, *274*, 6469-6476.
31. Gaede-Koehler, A.; Kreider, A.; Canfield, P.; Kleemeier, M.; Grunwald, I. *Anal. Chem.* **2012**, *84*, 10229-10235.
32. Baardsnes, J.; Davies, P.L. *Biochim. Biophys. Acta* **2002**, *1601*, 49-54.
33. Garnham, C.P.; Natarajan, A.; Middleton, A.J.; Kuiper, M.J.; Braslavsky, I.; Davies, P.L. *Biochemistry* **2010**, *49*, 9063-9071.
34. Howard, E.I.; Blakeley, M.P.; Haertlein, M.; Petit-Haertlein, I.; Mitschler, A.; Fisher, S.J.; Cousido-Siah, A.; Salvay, A.G.; Popov, A.; Muller-Dieckmann, C.; Petrova, T.; Podjarny, A. *J. Mol. Recogn.* **2011**, *24*, 724-732.
35. Chao, H.; Houston, M.E.; Hodges, R.S.; Kay, C.M.; Sykes, B.D.; Loewen, M.C.; Davies, P.L.; Sönnichsen, F.D. *Biochemistry* **1997**, *36*, 14652-14660.
36. Bar-Dolev, M.; Celik, Y.; Wettlaufer, J.S.; Davies, P.L.; Braslavsky, I. *J. R. Soc. Interface* **2012**, *9*, 3249-3259.
37. Meister, K.; Duman, J.G.; Xu, Y.; DeVries, A.L.; Leitner, D.M.; Havenith, M. *J. Phys. Chem. B* **2014**, *118*, 7920-7924.
38. Garnham, C.P.; Gilbert, J.A.; Hartman, C.P.; Campbell, R.L.; Laybourn-Parry, J.; Davies, P.L. *Biochem. J.* **2008**, *411*, 171-180.
39. Baardsnes, J.; Jelokhani-Niaraki, M.; Kondejewski, L.H.; Kuiper, M.J.; Kay, C.M.; Hodges, R.S.; Davies, P.L. *Prot. Sci.* **2001**, *10*, 2566-2576.
40. Antson, A.A.; Smith, D.J.; Roper, D.I.; Lewis, S.; Caves, L.S.D.; Verma, C.S.; Buckley, S.L.; Lillford, P.J.; Hubbard, R.E. *J. Mol. Biol.* **2001**, *305*, 875-889.
41. Raymond, J.A.; Wilson, P.; DeVries, A.L. *Proc. Natl. Acad. Sci. U.S.A.* **1989**, *86*, 881-885.
42. Wilson, P.W.; Beaglehole, D.; DeVries, A.L. *Biophys. J.* **1993**, *64*, 1878-1884.
43. Garnham, C.P.; Campbell, R.L.; Davies, P.L. *Proc. Natl. Acad. Sci. U.S.A.* **2011**, *108*, 7363-7367.
44. Liou, Y.C.; Tocilj, A.; Davies, P.L.; Jia, Z. *Nature* **2000**, *406*, 322-324.
45. Hobbs, P.V. *Ice Physics* **1974** Oxford University Press.
46. Drori, R.; Davies, P.L.; Braslavsky, I. *RSC Adv.* **2015**, *5*, 7848-7853.
47. Knight, C.A.; DeVries, A.L. *Phys. Chem. Chem. Phys.* **2009**, *11*, 5749-5761.
48. Drori, R.; Celik, Y.; Davies, P. L.; Braslavsky, I. *J. R. Soc. Interface* **2014**, *11*, 20140526.
49. Yang, D.S.C.; Sax, M.; Chakrabartty A.; Hew, C.L. *Nature* **1988**, *333*, 232-237.
50. Chao, H.; Davies, P.L.; Sykes, B.D.; Sönnichsen, F.D. *Prot. Sci.* **1993**, *2*, 1411-1482.

51. Studier, F.W. *Protein Expr. Purif.* **2005**, *41*, 207–234.
52. Salvay, A.G.; Gabel, F.; Pucci, B.; Santos, J.; Howard, E.I.; Ebel, C. *Biophys. J.* **2010**, *99*, 609-618.
53. Amornwittawat, N.; Wang, S.; Duman, J.G.; Wen, X. *Biochim. Biophys. Acta* **2008**, *1784*, 1942–1948.

Chapter 3

Ice binding of poly(vinyl alcohol)

Abstract

Antifreeze proteins (AFPs) are a class of biomacromolecules able to control and modify ice crystal growth, but they are relatively expensive to produce and available in small quantities only. The development of inexpensive ice binding materials which can be produced at large scale would allow for controlling ice growth in a broad range of products and technologies. Poly(vinyl alcohol) (PVA) is one of the few hydrophilic polymers which shows ice recrystallization inhibition (IRI) activity comparable to AFPs. At present, it is not known whether PVA and AFPs bind ice through a similar mechanism. Therefore, a series of PVA polymers was prepared by reversible addition-fragmentation chain-transfer (RAFT) polymerization to gain control over both polymer molecular weight and tacticity by using vinyl ester monomers with varying bulky substituents. The polymer tacticity influences the crystallinity of PVA, which can be an important factor for its ice binding properties. Furthermore, a fluorescent label was incorporated via a single terminal naphthalimide group to study ice binding using fluorescent microscopy.

3.1 Introduction

The development of inexpensive, degradable and biocompatible polymeric ice binding materials will widely broaden the application perspective of non-colligative antifreezes. The major advantage of non-colligative freeze protection is the negligible impact on the physical, structural and functional properties of the surrounding materials, since much lower concentrations are required than for colligative antifreeze agents. This may hold great potential for the cryopreservation of human cells and organs transplants, stabilization of microemulsions and dispersions, etc.^{1,2} Controlling ice growth with synthetic AFP mimics has recently gained a lot of attention.³ Primary focus has been the synthesis of structural analogues of antifreeze glycoproteins (AFGP).^{4,5} Since this often involves complicated sugar and peptide chemistry, the realization of an inexpensive synthetic mimic of AFPs amenable to large scale production seems unfeasible via this route. On the other hand, poly(vinyl alcohol) (PVA) is an inexpensive polymer and is known to inhibit ice-recrystallization (IRI).^{6,7} Congdon *et al.* demonstrated that PVA requires a minimal degree of polymerization $DP > 20$ and degree of hydrolysis $> 80\%$ to elicit IRI activity (Figure 1).⁸ PVA has been used in the cryopreservation of human blood cells,⁹ and in the application of ice slurries for refrigeration.¹⁰ Inada *et al.* proposed that PVA binds to the pyramidal planes based on direct observation of the growth habit of a single ice crystal suspended in a PVA solution.¹¹ On the other hand, Budke *et al.* proposed binding to prism planes since the conformation of an atactic PVA segment adsorbed on primary and secondary prism planes matches well with the ice lattice via multiple hydrogen bonding (Figure 2).⁶ The spacing between neighboring C-O bonds in PVA is $S_{PVA} = 2.52 \text{ \AA}$, while the spacing between every O-atom in the unit cell of ice is $S_{ice} = 7.36 \text{ \AA}$, which is approximately $3 \times S_{PVA} = 7.56 \text{ \AA}$. Since the number and accessibility of the OH groups for hydrogen bonding to the ice are influenced by molecular weight and polymer tacticity, it is of interest to study the impact of these two characteristics on ice binding.

Polymer tacticity describes the stereochemistry of adjacent chiral centers of the monomer subunits in a polymer, and significantly affects the physical properties of the polymer. Two adjacent units in a polymer constitute a diad, which are termed meso (*m*) if the substituents of the units are identically oriented, and racemic (*r*) if the chirality is oriented in opposite. However, simultaneous control over molecular weight and polymer tacticity of PVA is a synthetic challenge. Usually PVA is prepared via the hydrolysis of a poly(vinyl acetate) precursor, resulting in atactic PVA ($r \sim 52\text{-}54\%$). The stereospecific polymerization of vinyl esters is affected by using fluorinated (co)-solvents, monomers with bulky or fluorinated substituents, or the used catalyst in (non-living) polymerization strategies.¹²⁻¹⁴ Up to now the highest isotacticity reported ($m \sim 78\%$) was obtained using non-living cationic polymerization of *tert*-butyl vinyl ether (*t*BVE) using $\text{BF}_3 \cdot \text{OEt}_2$ as initiator in toluene at $-78 \text{ }^\circ\text{C}$ ($M_n = 74,200$, $M_w/M_n = 2.02$).¹⁴ The highest reported syndiotacticity of PVA is $r \sim 69\%$, which was obtained using non-living radical polymerization of the fluorinated vinyl ester monomer vinyl 2,2-bis(trifluoromethyl)propionate in tetrahydrofuran (THF) at $0 \text{ }^\circ\text{C}$ with benzoyl peroxide (BPO)

as initiator ($M_n = 950$, $M_w/M_n = 1.46$),¹² but also by the polymerization of vinyl acetate (VAc) with hexafluoroisopropanol (HFIP) as co-solvent with tri-*n*-butylborane ($n\text{Bu}_3\text{B}$) as initiator at $-78\text{ }^\circ\text{C}$ ($M_n = 83.000$, $M_w/M_n = 1.5$).¹⁵

In this study, the synthesis of PVA is described via reversible addition-fragmentation chain-transfer (RAFT) polymerization of vinyl ester monomers with different (bulky) substituents aiming to alter the tacticity of the polymer. RAFT is used as a controlled radical polymerization strategy to have predetermined molecular weight and low dispersity, since atom-transfer radical polymerization (ATRP) of vinyl monomers is challenging due to the very low ATRP equilibrium constant, $k_{eq} = k_{act}/k_{deact}$ (i.e., low dissociation of the dormant species). Moreover, RAFT polymerization allows for facile introduction of chain-end functionalities by modification of the chain-transfer agent (CTA) to provide a terminal fluorescent group on the PVA polymer, which can be used to study the ice binding of PVA.

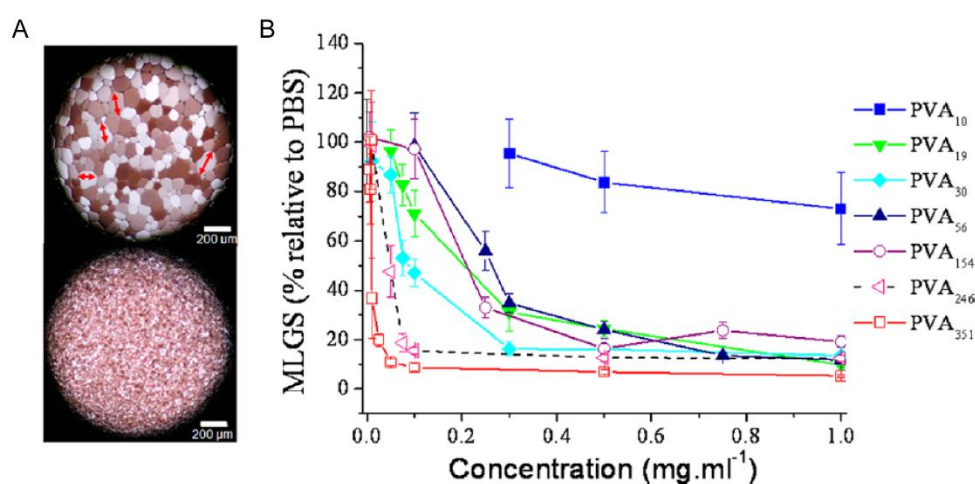


Figure 1: Ice recrystallization inhibition activity of PVA measured using the splat assay in PBS buffer. (A) PBS buffer (top) and with PVA₃₅₁, 1 mg/ml (bottom). (B) IRI activity of PVA with varying degrees of polymerization, demonstrating the minimal requirements for IRI activity of PVA (DP > 20). MLGS is the mean largest grain size relative to PBS buffer.⁸

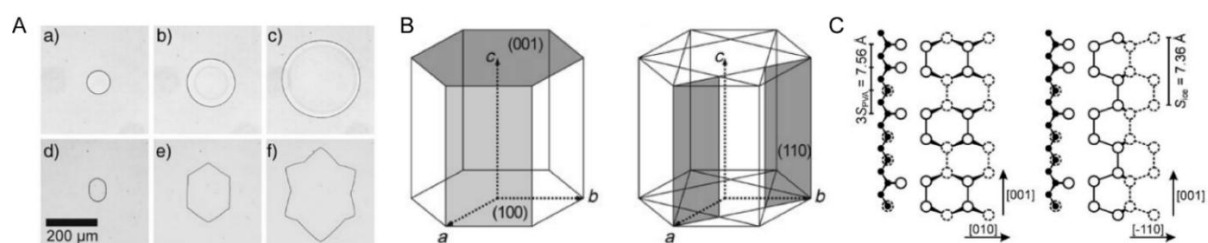
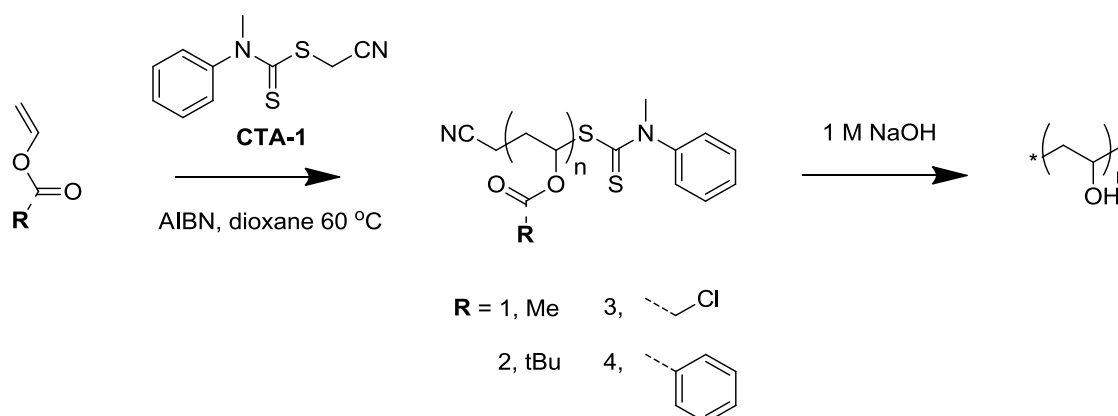


Figure 2: Ice growth habit experiment of PVA. (A) Habit of single ice crystal growing at $-0.3\text{ }^\circ\text{C}$ in pure water (a-c) and in the presence of PVA₂₇ (d-f, 10 mg/ml). (B) Suggested adsorption planes of PVA. (C) Visualization of an adsorbed atactic PVA segment onto primary prism face (left) and secondary prism face (right) of hexagonal ice.⁶

3.2 Results

3.2.1 Kinetics of RAFT polymerization of vinyl ester monomers

Four vinyl ester monomers with different substituents were used in this study; vinyl acetate (VAc), vinyl pivalate (VPi), vinyl chloroacetate (VClAc), and vinyl benzoate (VBz). RAFT polymerization of the vinyl ester monomers was performed using cyanomethyl methyl(phenyl)carbamodithioate (CTA-1), suitable for electron-rich monomers such as vinyl esters and vinyl amides, with AIBN as initiator in 10 v/v% dioxane at 60 °C (Scheme 1). First, the kinetics of the polymerization reactions of the vinyl ester monomers was studied by following the monomer conversion by ^1H NMR (Figure 3A). A significant retardation (~ 6-7h) is observed for all vinyl monomers. VPi and VAc showed a fast monomer conversion rate, reaching ~ 65 % conversion after 9 and 14 h, respectively. The polymerization rate of the electron deficient VClAc was slower, reaching a conversion of ~ 65 % after 36 h. Polymer dispersities are between $M_w/M_n = 1.3$ and 1.5 (Table 1), which is typical for controlled radical polymerization of vinyl esters. The significantly lower polymerization rate of VBz has been reported before, and is attributed to the formation of stable aryl adduct radicals, leading to degradative chain transfer and termination reactions.¹⁷⁻²⁰ This is in line with the higher dispersity ($M_w/M_n = 1.67$) of the resulting PVBz polymer (Figure 4D).



Scheme 1: RAFT polymerization of vinyl esters monomers using commercially available CTA-1.

Table 1: Overview of RAFT polymerization of vinyl ester monomers with varying substituents (1-4). Polymerization condition: $[M]_0 : \text{CTA} : \text{AIBN} = 250 : 1 : 0.2$, 60 °C, 10 v/v% dioxane.

	Monomer	t (h)	NMR			GPC	
			Conv. (%)	M_n (kDa)	DP	M_n (kDa)	M_w/M_n
1	VAc	14	71	15.500	178	16.700	1.37
2	VPi	9	72	23.300	180	21.900	1.45
3	VClAc	43	74	22.200	185	24.300	1.46
4	VBz	120	59	22.100	148	12.200	1.67

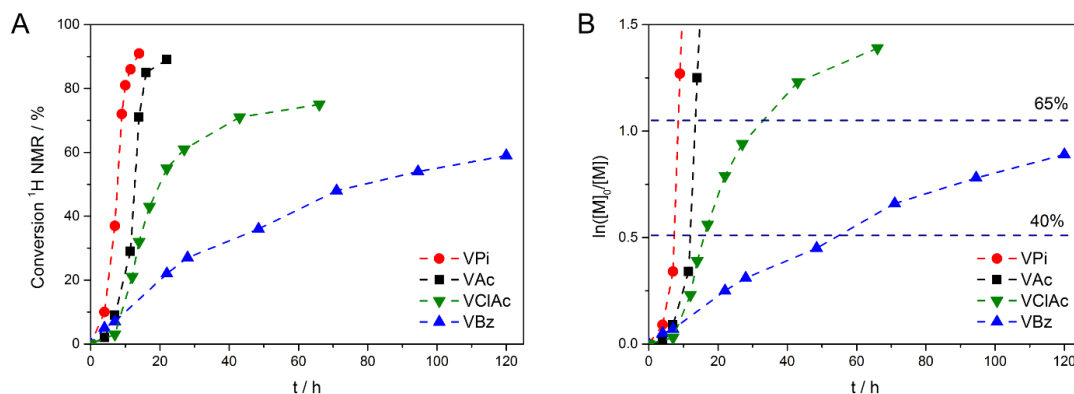


Figure 3: (A) Monomer conversion as determined by ^1H NMR (CDCl_3), and (B) semilogarithmic kinetic plot of the monomer conversion. The two dotted lines correspond to 40 % and 65 % monomer conversion respectively.

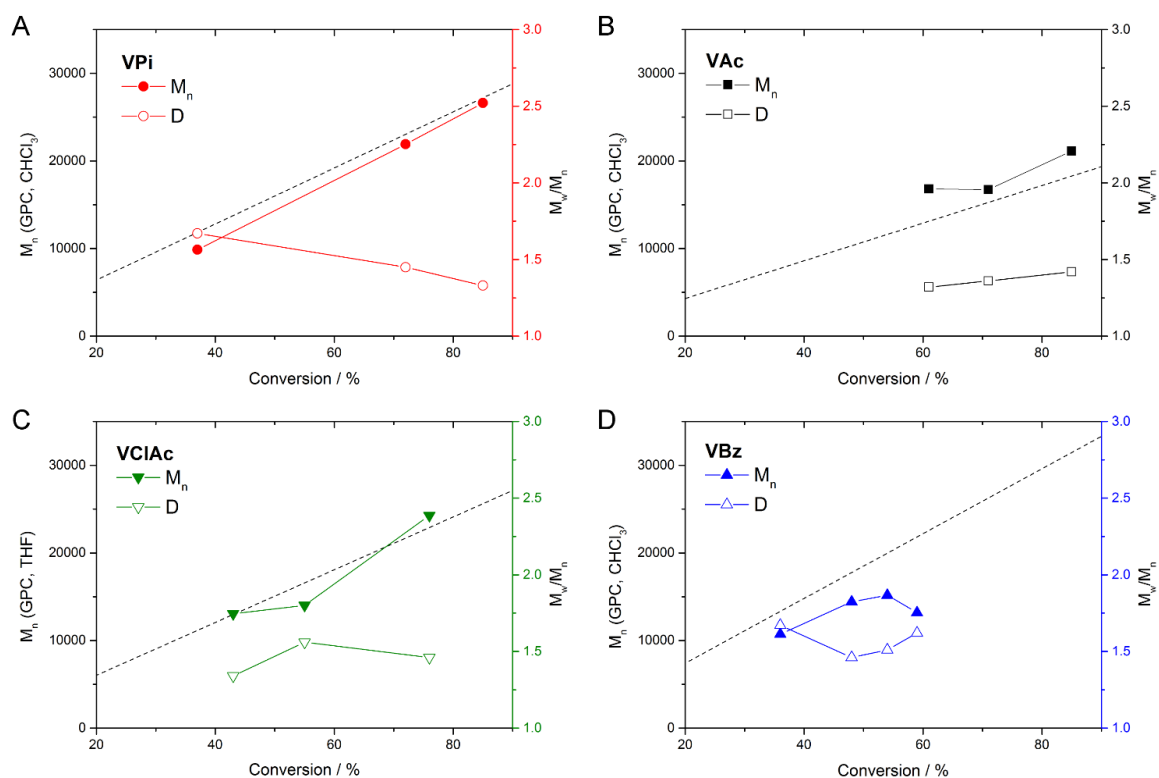


Figure 4: Evolution of M_n and M_w/M_n as a function of monomer conversion. The dashed lines illustrate the theoretical M_n as a function of monomer conversion.

3.2.2 Hydrolysis of poly(vinyl esters) to poly(vinyl alcohol)

Based on the kinetics studies of the polymerization reactions, PVA syntheses were set-up and quenched at approximately 65 % monomer conversion. The vinyl ester polymers were precipitated in pentane and subsequently hydrolyzed in 1 M NaOH to yield PVA. The diad tacticity is calculated from the triad tacticity using ^1H NMR in d_6 -DMSO (Figure 5). Hydrolysis of PVAc and PVPi results in a diad syndiotacticity of respectively $r = 54\%$ and $r = 60\%$ (Table 2), which is similar to the reported values from bulk free radical polymerization of the vinyl monomers at $60\text{ }^\circ\text{C}$.¹⁶ With PVBz as precursor, a slightly lower syndiotacticity $r = 49\%$ was obtained, while hydrolysis of PVClAc yielded a similar tacticity to PVAc ($r = 54\%$).

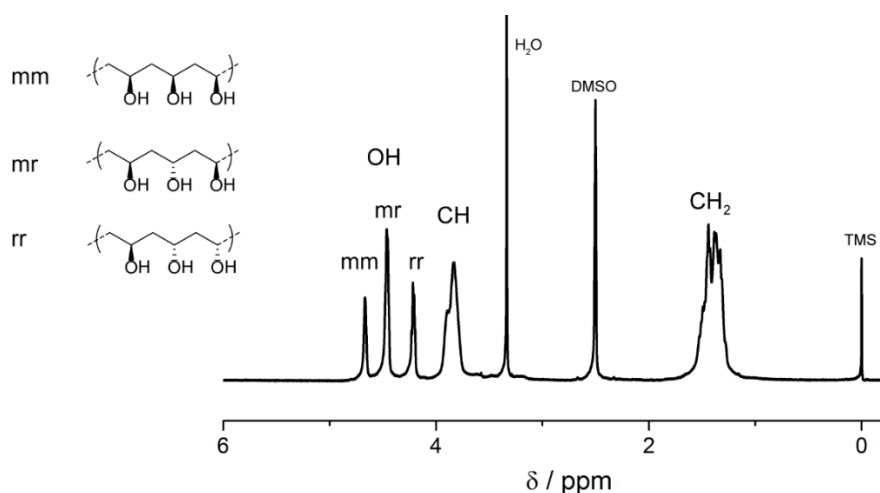


Figure 5: ^1H NMR (d_6 -DMSO) showing the triad tacticity of PVA-1.

Table 2: Triad tacticity of the hydrolyzed of poly(vinyl ester) determined using ^1H NMR (d_6 -DMSO), and diad syndiotacticity calculated via $r = rr + \frac{mr}{2}$.

	Polymer precursor	mm (%)	mr (%)	rr (%)	$\frac{rr}{mm}$	r (%)
PVA-1	PVAc	21	50	29	1.43	54
PVA-2	PVPi	15	50	35	2.36	60
PVA-3	PVClAc	21	49	30	1.39	54
PVA-4	PVBz	27	48	25	0.91	49

3.2.3 Antifreeze activity of poly(vinyl alcohol)

The antifreeze activity of PVA-1 ($r = 54\%$, PVAc precursor) was measured using ice recrystallization inhibition (IRI) experiments. Samples were measured in PBS buffer to directly compare the results with IRI activity experiments reported by Congdon *et al.*⁸ In a typical IRI experiment, a 1 μL sample is placed between two cover slides and is quickly frozen to $-40\text{ }^\circ\text{C}$. After 5 min. the sample is heated to $-6\text{ }^\circ\text{C}$ and held at that temperature for 30 min. Micrographs were taken at regular time intervals to follow the grain boundary migration process. IRI activity of PVA-1 is observed down to a concentration of 0.2 mg/ml (Figure 6), which is in line with reported values for PVA with a degree of polymerization of $\text{DP} \sim 178$.⁸

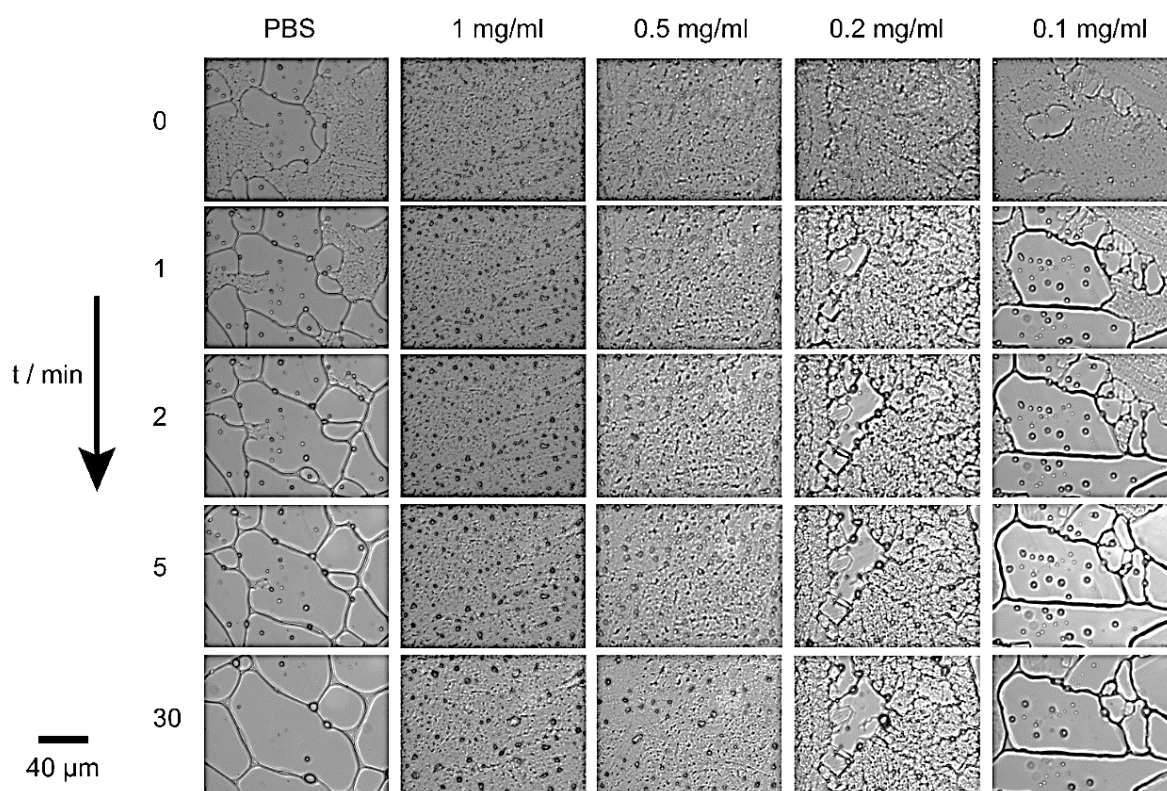


Figure 6: Ice recrystallization inhibition (IRI) measurements of PVA-1 ($M_n \sim 7.800$, $\text{DP} = 178$). All samples were measured in PBS buffer, and annealed for 30 min at $-6\text{ }^\circ\text{C}$. The small dots in the micrographs are air bubbles.

The thermal hysteresis (TH) activity of PVA-1 was measured using the sonocrystallization method. While 0.2 mg/ml solutions of PVA-1 inhibit ice recrystallization, no thermal hysteresis activity is observed for PVA-1 solutions at a concentration of 5 mg/ml (Figure 7A). Instead, the temperature profile of a 5 mg/ml solution (red line) resembles that of the buffer (black line), which means that PVA-1 does not produce a TH gap. Also when mixed with type III AFP (rQAE isoform), the $\sim 0.02\text{ }^\circ\text{C}$ reduction of the non-equilibrium freezing point is insignificant; i.e. within experimental uncertainty. For comparison, the pyramidal plane binding type I AFP

from winter flounder (*wfAFP1*) which shows only minimal TH activity, does significantly enhance the TH activity of rQAE by 0.19 °C (Figure 7B).

The IRI and TH activity of PVA-2 ($r = 60\%$, PVPi precursor) was also tested. Again, IRI was observed at and above a concentration of 2 mg/ml, while no TH was detected in the presence or absence of rQAE. Apparently the 6 % difference in tacticity does not result in appreciable difference in activity. Also, the current difficulties to quantify the IRI activity does not allow for reliably assessing the influence of only a minimal ($\sim 6\%$) difference in tacticity on the antifreeze properties of PVA.

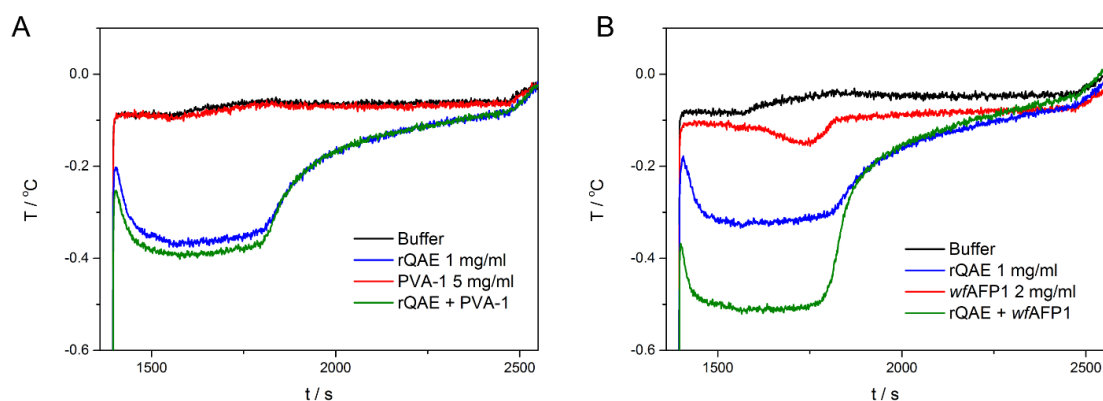
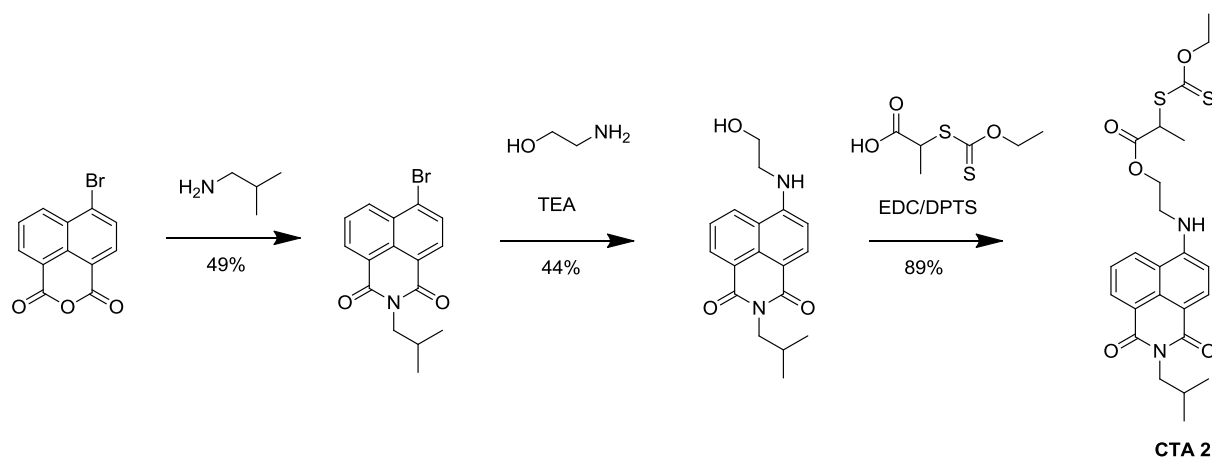


Figure 7: (A) Sonocrystallization measurement of PVA-1 (5 mg/ml) and PVA-1 (5 mg/ml) mixed with type III AFP (rQAE, 1 mg/ml). (B) Sonocrystallization measurement of winter flounder type I AFP *wfAFP1* (2 mg/ml), and *wfAFP1* (2 mg/ml) mixed with type III AFP (rQAE, 1 mg/ml). All samples were measured in 20 mM Tris, pH 7.5.

3.2.4 Synthesis of fluorescently labeled pol(vinyl alcohol)

As demonstrated in chapter 2, the specific ice adsorption plane of AFPs determines the TH activity measured using sonocrystallization. Only AFPs that bind fast and in sufficiently large amounts to fast growing ice crystal planes are able to block rapid ice crystal growth. Hence, we aim to probe to which ice crystal plane PVA binds by fluorescent microscopy to better understand why PVA is IRI active but shows no TH activity.

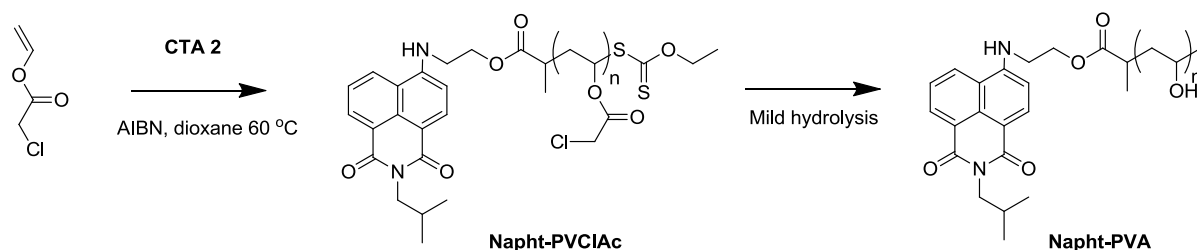
A terminal naphthalimide dye can be readily introduced into PVA prepared by RAFT/MADIX polymerization via a naphthalimide-substituted xanthate. Naphthalimide dyes have strong fluorescence and good photo-stability, and have been used to prepare fluorescent single chain nanoparticles.²¹ A xanthate with a naphthalimide substituent (CTA-2) was synthesized following the procedure described by Bardajee *et al.*²² The synthesis involves a condensation reaction of naphthalimide anhydride with isobutyl amine, followed by a nucleophilic aromatic substitution reaction and esterification with xanthogenic acid via EDC/DPTS coupling (Scheme 2).



Scheme 2: Synthesis of CTA-2, following the procedure of Bardajee *et al.*²²

Polymerization of VClAc using CTA-2 (Scheme 3), using AIBN as initiator in dioxane at 60 °C showed a very slow propagation rate and low conversion (Figure 8). The reaction was stopped after 116 h at 22 % conversion. This corresponds to a theoretical molecular weight of $M_n = 7.100$ Da (DP ~ 55), calculated from the starting monomer concentration and ratio $[M]_0/[CTA] = 250$. GPC analysis shows a molecular weight $M_{n,GPC} = 6.200$ (DP ~ 48) with a dispersity $M_w/M_n = 1.34$. The low monomer conversion rate can be attributed to the formation of radical adducts with the naphthalimide. In an attempt to obtain higher molecular weights, V-40 was used as initiator at a reaction temperature of 88 °C to obtain a higher radical flux. However, this resulted in an even lower conversion (Figure 8) and after 4 days the color of the reaction mixture changed from green to dark red-brown, suggesting the formation of adducts

of the naphthalimide group. Therefore, no further polymerizations were conducted with V-40 as initiator.



Scheme 3: RAFT/MADIX polymerization of VClAc using CTA-2.

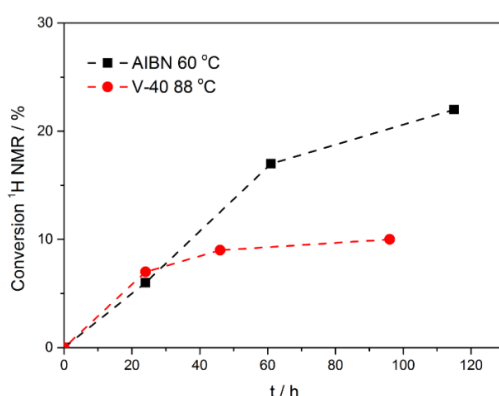


Figure 8: Plot of monomer conversion followed by ^1H NMR with AIBN (■) and V-40 (●) as radical initiator.

After precipitation in pentane and drying under high vacuum, the naphthalimide-substituted PVClAc (Napht-PVClAc) had a yellow-green color. The ^1H NMR spectrum of Napht-PVClAc shows aromatic signals ($\delta = 7-9$ ppm) and a doublet ($\delta = 0.97$ ppm) from the isopropyl group of the naphthalimide substituent (Figure 9). Napht-PVClAc was hydrolyzed under mild conditions²² to yield orange colored PVA with a terminal naphthalimide group (Napht-PVA). The ^1H NMR spectrum shows a degree of hydrolysis near 100 %. The degree of labeling can be calculated from the integrals of the NMR signals of **e** and **g**, showing that there is approximately one naphthalimide group per 59 monomers ($M_n \sim 3.100$, $DP = 59$), which is closely corresponding to the DP calculated from the monomer conversion and GPC analysis.

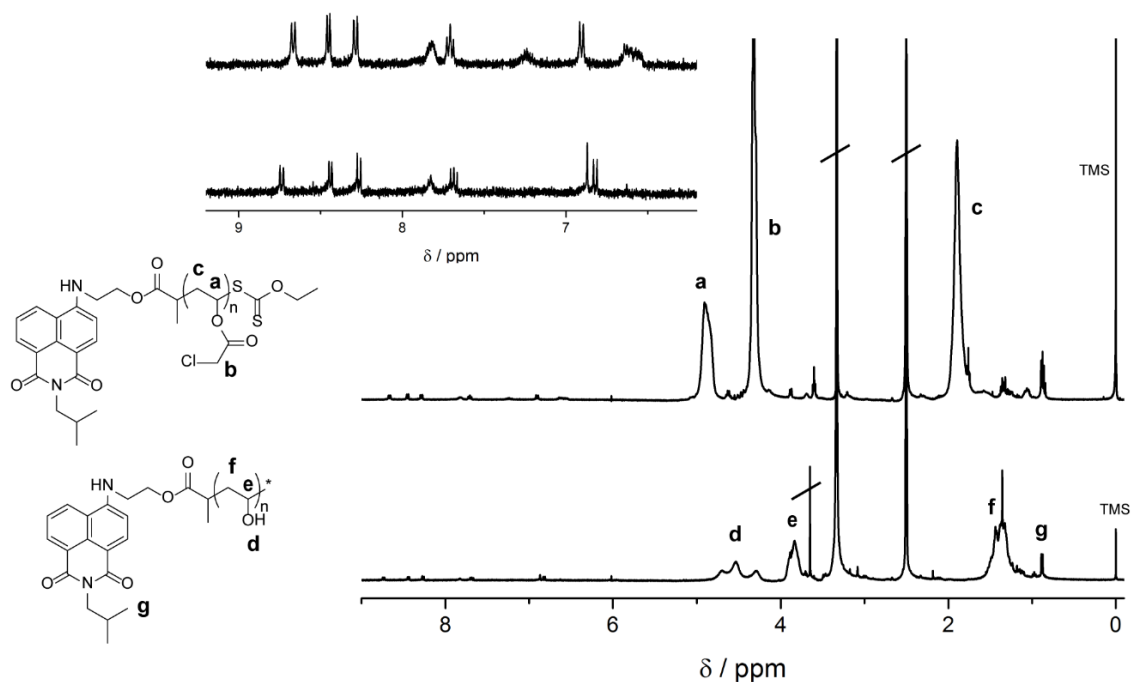


Figure 9: ¹H NMR (*d*₆-DMSO) spectrum of Napht-PVClAc (top) and Napht-PVA (bottom). Inset shows the aromatic signals from the naphthalimide group ($\delta = 7-9$ ppm).

3.2.5 Characterization of fluorescently labeled pol(vinyl alcohol)

Absorption and emission spectra of Napht-PVA show a maximum absorbance and emission intensity at wavelengths $\lambda_{\text{Abs,max}} = 445$ nm and $\lambda_{\text{Em,max}} = 547$ nm (Figure 10), and an extinction coefficient of $\epsilon = 1.922 \text{ M}^{-1} \text{ cm}^{-1}$ calculated using the Lambert-Beer law. These agree well with reported values for naphthalimide dyes in organic solvents, taking into account that in water wavelengths of maximum absorbance and emission intensity show a red-shift compared to organic solvents and a ten-fold lower extinction coefficient.²³

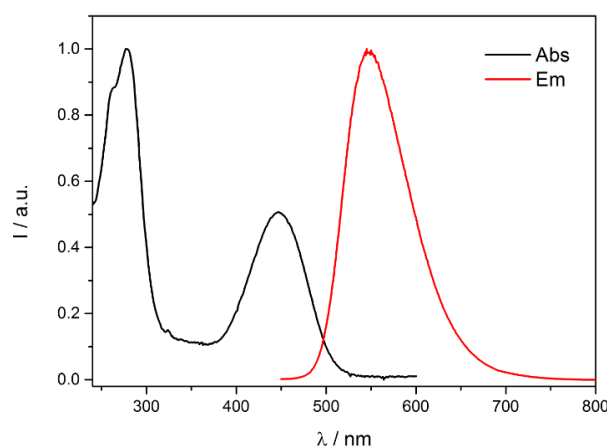


Figure 10: Normalized absorption and emission spectra of Napht-PVA measured in PBS buffer. $\lambda_{\text{Abs,max}} = 445$ nm, $\lambda_{\text{Em,max}} = 547$ nm ($\lambda_{\text{exc}} = 440$ nm), $c = 1$ mg/ml, $l = 0.2$ cm, $\epsilon = 1922 \text{ M}^{-1} \text{ cm}^{-1}$.

In ice recrystallization inhibition experiments (bright field, Figure 11A-C), Napht-PVA is IRI active down to a concentration of 1 mg/ml. This shows that Napht-PVA is slightly less active than PVA-1, which can arise from the difference in the degree of polymerization; DP = 48 for Napht-PVA and DP = 178 for PVA-1. Previous work by Congdon *et al.* has revealed that longer PVAs are active at lower concentrations (Figure 1).⁸

The inhibition of grain boundary migration processes by Napht-PVA can be observed using fluorescence IRI (FL-IRI) experiments (Figure 11B-D), during an annealing process of 45 min at -6 °C. The centers of the large ice grains show minimal fluorescence, which may indicate that the Napht-PVA becomes excluded from the large growing ice grains during the recrystallization process. However, the grain boundaries could not be well resolved under high magnification due to the presence of many air bubbles, which appear brightly fluorescent due to the preferential localization of the hydrophobic naphthalimide group at the air-water interface. The Napht-PVA was also used in an ice growth habit experiment as described by Budke *et al.* (Figure 2A),⁶ in order to observe the ice shaping ability of PVA using fluorescence microscopy. However, these experiments proved to be too challenging with the current experimental set-up due to limited temperature control.

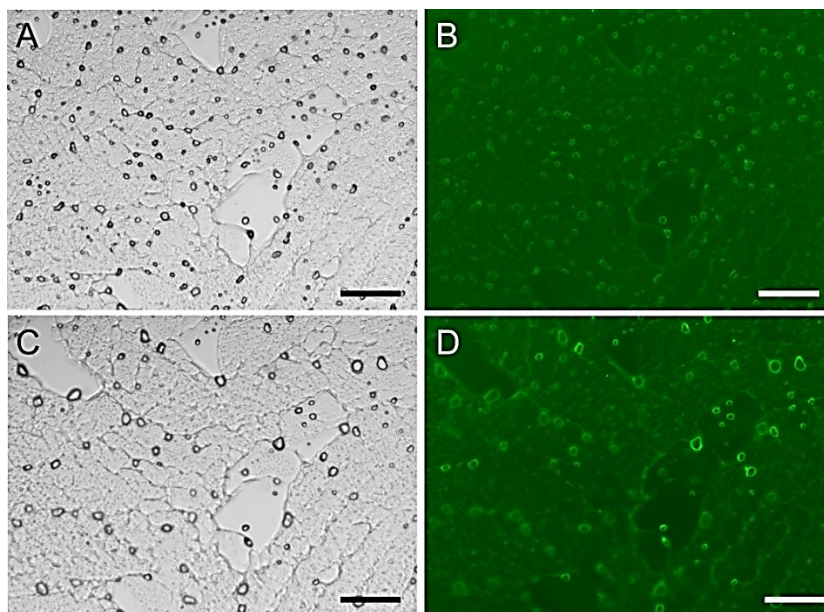


Figure 11: Brightfield (A-C) and fluorescence (B-D) micrographs of the ice recrystallization inhibition experiments of Napht-PVA (1 mg/ml) measured in PBS buffer, after 10 min (A-B) and 45 min (C-D) annealing at -6 °C. Scale bar represents 100 μm .

3.3 Discussion

3.3.1 Controlled radical polymerization of poly(vinyl alcohol)

Advances in controlled radical polymerization techniques allow for the synthesis of well-defined polymers with predefined molecular weight and narrow molecular weight distribution. The molecular weight of a polymer has a significant effect on the material properties, such as its mechanical properties, crystallinity, solubility, etc. As has been demonstrated by Congdon *et al.*, also the antifreeze activity of poly(vinyl alcohol) determined by IRI experiments is proportional to molecular weight, and a minimal number of 20 monomer subunits ($DP > 20$) is required in order to inhibit the recrystallization of ice. In addition to molecular weight, the physical properties of polymeric materials are also influenced by tacticity. Tacticity describes the relative orientation of the side groups of adjacent subunits along the polymer backbone, which is particularly important for vinyl polymers. In addition, Budke *et al.* proposed a good match of atactic PVA to the prism planes of ice,⁶ suggesting that the tacticity of PVA could also influence its antifreeze properties. However, controlling both molecular weight and polymer tacticity of poly(vinyl esters) remains a challenge. To further investigate the effect of polymer tacticity on the ice binding properties of PVA, we have used four vinyl ester monomers with different bulky substituents for the preparation of poly(vinyl esters) using RAFT polymerization as precursors for PVA.

Hydrolysis of PVAc obtained via RAFT polymerization gives an atactic polymer with $r \sim 54$ %. With PVPi as a precursor, PVA with a slightly higher syndiotacticity $r = 60$ % is obtained, due to steric hindrance of the bulky *tert*-butyl group during the polymerization reaction of VPi. Hydrolysis of PVClAc yields a tacticity similar to PVAc ($r \sim 54$ %), while hydrolysis of PVBz resulted in a slightly lower syndiotacticity $r = 49$ %. Despite the use of monomers with different bulky substituents, the difference in polymer tacticity of PVA is only small (5-6 %). Other co-solvents (such as HFIP or heptane) instead of dioxane did not yield a different tacticity (HFIP) or resulted in decreased solubility of the CTA (heptane). Clearly, tacticity is difficult to control in radical polymerization reactions. The energy difference between two enantiomers of an active radical species is low, especially compared to the thermal energy of the reaction temperature (60 °C). Even though bulky substituents of vinyl ester monomers can alter the energy difference via steric hindrance, reaction temperature is probably a more dominant factor. Hence, PVA with high iso- or syndiotacticity is mostly obtained at very low polymerization temperatures (e.g., -78 °C).^{14,15} Furthermore, the type of catalyst and co-solvent used will also influence the resulting polymer tacticity. Since it is difficult to accurately quantify IRI activity, a tacticity difference of at least 20 % is required to reliably assess the influence of polymer tacticity on the ice binding of PVA. Hence, low temperature polymerization strategies have to be applied in order to obtain high iso- and syndiotactic PVA.

3.3.2 Conformation of poly(vinyl alcohol) at the ice-water interface

Antifreeze proteins are shown to have a wide variety in structural complexity. Poly(vinyl alcohol) on the other hand, has no particular structure in solution, but is able to inhibit the recrystallization of ice similar to AFPs. This raises the question if the underlying mechanism that governs the antifreeze activity of PVA and AFPs is identical. Crystallographic data and site-directed mutation studies suggest that AFPs have an ice binding face which is relatively flat, hydrophobic and rich in threonine residues. This amphipathic character results in high surface activity of the proteins. Recent vibrational sum frequency generation (vSFG) experiments demonstrated the accumulation of a β -helical AFP (DAFP-1) at the air-water interface with its threonine rich ice binding face pointing towards the air.²⁴

Similar to AFPs, PVA is an amphiphilic macromolecule with high surface activity. Molecular dynamics simulations at the water-vacuum interface showed that monodisperse atactic oligomers (DP = 30) of PVA display two different states at low and high concentration.²⁵ At low concentration, PVA chains display elongated, rigid structures at the interface, while networks are formed at high concentrations via intra- and intermolecular hydrogen bonding, along with substantial slowing of polymer and water dynamics at the interface. Furthermore, preliminary vSFG measurements at the air-water interface suggested the orientation of the OH groups of PVA pointing up in the air, while the hydrophobic backbone is pointed towards the water phase.²⁴ Possibly, PVA adopts a conformation at the ice-water interface where OH groups hydrogen bond to clathrate waters and the hydrophobic backbone points towards the water phase, similar to AFPs.²⁷

Why then is PVA not able to lower the non-equilibrium freezing point? Arresting rapid ice growth requires fast binding to fast growing non-basal ice planes (chapter 2), with sufficient surface coverage, to effectively hinder the addition of water molecules to the growing ice surface. Possibly, the thin and flexible polymer backbone of PVA is limiting its ability to sterically hinder the growing ice front to give rise to the Gibbs-Thomson effect. Further characterization of the conformation of PVA at both air-water and ice-water interface might give a more complete explanation of how PVA adsorbs to ice crystal planes and if the molecular recognition event is similar to AFPs.

3.4 Conclusion

A molecular description of the ice-PVA interaction and knowledge on which factors govern ice binding of PVA is currently still missing. It is likely that the multivalent interaction is influenced by both the molecular weight and tacticity of the polymer. Controlling both molecular weight and tacticity of poly(vinyl esters) is currently still a major synthetic challenge. In this study, vinyl ester monomers with varying bulky substituent have been used to alter the tacticity of PVA using RAFT polymerization. However, only a syndiotacticity difference of ~ 5-6 % was obtained. Polymerization at lower reaction temperatures or with other catalysts may allow gaining control over both polymer properties to test their effect on the antifreeze activity of PVA. Moreover, PVA end-functionalized with a naphthalimide group was prepared via the synthesis of a naphthalimide substituted xanthate. The naphthalimide substituted PVA (Napht-PVA) will be used for FIPA analysis in order to determine the ice binding planes of PVA.

3.5 Materials and methods

Chemicals and materials

All commercial reagents were purchased from Sigma Aldrich and used as received without further purification, unless stated otherwise. Vinyl ester monomers were purified by passing through basic alumina prior to polymerization. Azobisisobutyronitril (AIBN, Sigma Aldrich) was recrystallized from methanol. N-ethyl-N'-(3-dimethylaminopropyl)carbodiimide hydrochloride (EDC) was purchased from Iris Biotech. Triethyl amine (TEA) was stored over KOH pellets. Deuterated solvents were obtained from Cambridge Isotope Laboratories and dried over molsieves. All solvents were of AR quality and purchased from Biosolve. All polymerization reactions were performed using a 10 mL Schlenk flask (Chemglass, AF-0520-20). Reactions were followed by thin-layer chromatography (precoated 0.25 mm, 60-F254 silica gel plates from Merck).

Instrumentation

Flash chromatography was performed using an automatic flash chromatography instrument Biotage Isolera One equipped with biotage SNAP KP-Sil silica cartridges. NMR spectroscopy was performed on a Varian Mercury Vx 400 MHz and/or Varian 400MR, operating at 400 MHz for ^1H and 100 MHz for ^{13}C . Chemical shifts are reported in ppm (δ) values relative to tetramethylsilane (TMS) or residual solvent. Splitting patterns are labeled as s, singlet; d, doublet; dd, double doublet; t, triplet; q, quartet; q, quintet; m, multiplet and b stands for broad. Matrix assisted laser desorption/ionisation (MALDI) mass spectra were obtained on a PerSeptive Biosystems Voyager DE-PRO spectrometer or Bruker autoflex speed spectrometer using α -cyano-4-hydroxycinnamic acid (CHCA) and *trans*-2-[3-(4-tert-butylphenyl)-2-methyl-2-propenylidene]malononitrile (DCTB) as matrices. Electron Spray Ionization Liquid Chromatography mass spectra (ESI-LCMS) were obtained on a LCQ Fleet from Thermo Scientific on a C18 column, Surveyor AS and PDA. IR spectra were recorded on a Perkin-Elmer FTIR Spectrum 2 spectrometer equipped with a Perkin-Elmer Universal ATR Sampler Accessory. THF-GPC measurements were performed on a Shimadzu-system (Prominence i LC-2030C 3D) equipped with two Agilent Technology columns in series (PLgel 5 μm mixed C [200-2.000.000 Da] and PLgel 5 μm mixed D [200-40.000 Da]), a RI detector and a PDA detector, with THF as eluent at 40 $^\circ\text{C}$ and a constant flow rate of 1 mL/min. The system was calibrated with polystyrene (PS) samples with a range of 580-100.000 Da (Polymer Laboratories). CHCl_3 -GPC measurements were performed on a Shimadzu-system (Prominence i LC-2030C 3D) equipped with a Agilent Technology Resipore column [200-400.000 Da], a RI detector and a PDA detector, with CHCl_3 as eluent at 40 $^\circ\text{C}$ and a constant flow rate of 1 mL/min. The system was calibrated with polystyrene (PS) samples with a range of 92-371.000 Da (Polymer Laboratories). UV/vis absorption spectra were recorded on a Varian Cary 50 spectrometer. Fluorescent emission spectra were recorded on a Varian Cary Eclipse

fluorometer. Fluorescence microscopy was performed using a Zeiss Axio observer D1 equipped with an AxioCam Mrm camera and Zeiss Axiovision software (Carl Zeiss), with an adapted temperature controlled stage (Nanoliter osmometer, Otago instruments).

Preparation of 4-(dimethylamino)pyridinium 4-toluenesulfonate, DPTS

Hydrated *p*-toluenesulfonic acid (PTSA, 1.96 g, 16 mmol) in toluene was dried by azeotropic distillation by using a Dean-Stark trap. An equimolar solution of 4-dimethylaminopyridine (DMAP, 3.04 g, 16 mmol) in warm toluene was added dropwise to the hot mixture. The resulting suspension is cooled and the solid collected by filtration. The crude product was purified by recrystallization from hot acetone.

Xanthogenic acid, XA

To a 250 mL round bottom flask were added potassium ethyl xanthogenate (20 g, 125 mmol), 2-bromopropionic acid (7.4 mL, 82 mmol) and 150 mL acetone, and stirred for 24 h at RT. The salt was filtered from the solution and the solvent removed under reduced pressure, yielding the final product as a yellow oil at 95 % purity. ¹H NMR (CDCl₃, 400 MHz): δ 10.52 (s, 1H, COOH), 4.61 (q, *J* = 7.1 Hz, 2H, OCH₂CH₃), 4.31 (q, *J* = 7.4, Hz, 1H, (CO)CH(CH₃)S), 1.54 (d, *J* = 7.4 Hz, 3H, (CO)CH(CH₃)S), 1.41 (t, *J* = 7.1 Hz, 3H, OCH₂CH₃). ¹³C NMR (CDCl₃, 100 MHz): 213.4, 176.5, 70.1, 49.7, 18.0, 13.8.

Typical procedure for RAFT polymerization of vinyl esters

A clean and dry 10 mL Schlenk flask was charged with 5 mL of vinyl ester monomer (250 eq.), cyanomethyl methyl(phenyl)carbamdithioate (CTA-1, 1 eq.), AIBN (0.2 eq.) and dioxane (10 v/v%, 0.56 mL). The flask was deoxygenated by three freeze-pump-thaw cycles, back-filled with argon and immersed in an oil bath at 60 °C. The monomer conversion was checked by ¹H NMR (CDCl₃) and the reaction stopped at ~ 65 % conversion by exposure to air. The reaction mixture was diluted with THF and the polymer precipitated three times in pentane, except PVPi which was precipitated in MeOH/water. The product was dried under high vacuum for 3-4 h. The molecular weights were checked by GPC. **PVAc** GPC (CDCl₃, PMMA standard): M_n = 16.700, DP = 189, D = 1.37. ¹H NMR (CDCl₃, 400 MHz): δ 4.87 (b, 1H, CH₂CHO), 2.03 (t, *J* = 7.6 Hz, 3H, CH₃(C=O)O), 1.76 (b, 2H, CH₂CHO). **PVPi** GPC (CDCl₃, PMMA standard): M_n = 21.900, DP = 170, D = 1.45. ¹H NMR (CDCl₃, 400 MHz): δ 4.80 (b, 1H, CH₂CHO), 1.73 (b, 2H, CH₂CHO), 1.17 (s, 9H, (CH₃)₃C(C=O)O). **PVCIAc** GPC (THF, PMMA standard): M_n = 24.300, DP = 202, D = 1.46. ¹H NMR (CDCl₃, 400 MHz): δ 4.96 (b, 1H, CH₂CHO), 4.10 (b, 2H, ClCH₂(C=O)), 1.93 (b, 2H, CH₂CHO). **PVBz** GPC (CDCl₃, PMMA standard): M_n = 12.200, DP = 82, D = 1.67. ¹H NMR (CDCl₃, 400 MHz): δ 7.74-7.13 (b, 5H, benzyl), 5.23 (b, 1H, CH₂CHO), 2.02 (b, 2H, CH₂CHO).

The poly(vinyl esters) were hydrolyzed by dissolving 0.5 g of polymer in 20 mL of THF, except PVAc which was dissolved in MeOH. A 10 mL solution of 1.2 g NaOH in MeOH/water (9:1 v/v%) was added dropwise and the reaction mixture was stirred overnight at 40 °C. The reaction mixture was neutralized by the addition of 2.5 mL HCl solution (37 %), after which the hydrolyzed polymer precipitated. The solution was decanted and the precipitate washed with methanol four times. Residual salt was removed via dialysis. The polymers were dried under high vacuum at RT for 3-4 h. The degree of hydrolysis and tacticity of the resulting poly(vinyl alcohol) was checked by ^1H NMR (d_6 -DMSO). ^1H NMR (d_6 -DMSO, 400 MHz): δ 4.67 mm, 4.47 mr, 4.22 rr (triad, 1H, OH), 3.83 (b, 1H, CH_2CHOH), 1.37 (b, 2H, CH_2CHOH).

4-bromo-N-isobutylnaphthalimide

4-bromo-1,8-naphthalic anhydride (2 g, 7.22 mmol) was dissolved in dioxane (20 mL) and isobutyl amine (2.9 mL, 28.9 mmol) was slowly added to the mixture at RT. The solution was refluxed for 4 h. The solvent was evaporated under reduced pressure and the product was separated by column chromatography (SiO_2 , heptane/acetone 3:1, $R_f = 0.45$, first fraction). The final product was obtained as a yellow solid (1.18 g, 49 %). ^1H NMR (CDCl_3 , 400 MHz): δ 8.65 (dd, $J = 1.2, 7.3$ Hz, 1H), 8.57 (dd, $J = 1.2, 8.5$ Hz, 1H), 8.41 (d, $J = 7.9$ Hz, 1H), 8.04 (d, $J = 7.8$ Hz, 1H), 7.84 (dd, $J = 7.3, 8.5$ Hz, 1H), 4.03 (d, $J = 7.5$ Hz, 2H), 2.24 (m, 1H), 0.98 (d, $J = 7.0$ Hz, 6H). ^{13}C NMR (CDCl_3 , 100 MHz): δ 163.9, 133.2, 132.1, 131.3, 131.1, 130.6, 130.1, 129.0, 128.1, 123.1, 122.2, 47.3, 27.3, 20.3. IR (ATR) ν_{max} : 2959, 1704, 1662, 1343, 1236, 780 cm^{-1} . MALDI-TOF: calcd. for $\text{C}_{16}\text{H}_{14}\text{BrNO}_2$ 332.02, found 332.07 (M+H).

4-(2-hydroxyethyl)amino-N-isobutylnaphthalimide

4-bromo-N-isobutylnaphthalimide (800 mg, 2.41 mmol) was dissolved in dioxane (20 mL) and 2-aminoethanol (1.5 mL, 24.1 mmol) and triethylamine (1.7 mL, 12 mmol) were added dropwise at RT. The reaction mixture was refluxed overnight. The solvent was evaporated under vacuum and the product separated by column chromatography (SiO_2 , heptane/acetone 1:1, $R_f = 0.30$, second fraction). The final product was obtained as a yellow solid (330 mg, 44 %). ^1H NMR (d_6 -DMSO, 400 MHz): δ 8.66 (d, $J = 8.6$ Hz, 1H), 8.39 (d, $J = 7.6$ Hz, 1H), 8.22 (d, $J = 9.1$ Hz, 1H), 7.72 (m, 1H), 7.65 (t, $J = 8.1$ Hz, 1H), 6.78 (d, $J = 8.3$ Hz, 1H), 4.88 (m, 1H), 3.84 (d, $J = 7.5$ Hz, 2H), 3.67 (m, 2H), 3.44 (m, 2H), 2.10 (m, 1H), 0.85 (d, $J = 6.7$ Hz, 6H), ^{13}C NMR (d_6 -DMSO, 100 MHz): δ 164.5, 163.7, 151.3, 134.8, 131.3, 129.9, 129.0, 124.7, 122.3, 120.6, 118.4, 108.0, 104.3, 59.2, 46.5, 46.0, 27.3, 20.7. IR (ATR) ν_{max} : 3383, 2959, 1683, 1638, 1581, 1395, 1374, 1353, 1246 cm^{-1} . MALDI-TOF: calcd. for $\text{C}_{18}\text{H}_{20}\text{N}_2\text{O}_3$ 312.15, found 313.21 (M+H).

4-(2-propionyloxyethylxanthateethyl)amino-N-isobutylnaphthalimide, CTA-2

4-(2-hydroxyethyl)amino-N-isobutylnaphthalimide (250 mg, 0.8 mmol), XA (466 mg, 2.4 mmol) and DPTS (236 mg, 0.8 mmol) were dissolved in 20 mL DMF. EDC (414 mg, 2.16

mmol) was dissolved in 10 mL chloroform and added dropwise on ice. The reaction mixture was left to stir at RT under argon overnight. The DMF was removed under reduced pressure, and 150 mL chloroform was added. The organic layer washed with 1 % NaHCO₃ twice and three times with water (100 mL). The organic layer was dried over MgSO₄ and the chloroform removed under reduced pressure. The product was purified by column chromatography (SiO₂, heptane/acetone 1:1, R_f = 0.55). The final product was obtained as an orange/brown oil (390 mg, 89 %). ¹H NMR (CDCl₃, 400 MHz): δ 8.59 (d, J = 7.3 Hz, 1H), 8.47 (d, J = 8.5 Hz, 1H), 8.09 (d, J = 8.5 Hz, 1H), 7.66 (t, J = 7.6 Hz, 1H), 6.71 (d, J = 8.2 Hz, 1H), 5.74 (m, 1H), 4.64-4.45 (m, 5H), 4.02 (d, J = 7.1 Hz, 2H), 3.71 (q, J = 4.7, 5.1 Hz, 2H), 2.25 (m, 1H), 1.59 (d, J = 7.3 Hz, 3H), 1.33 (t, J = 6.6 Hz, 3H), 0.97 (d, J = 6.5 Hz, 6H). ¹³C NMR (CDCl₃, 100 MHz): δ 212.2, 207.2, 172.6, 164.9, 164.4, 148.8, 134.3, 131.3, 130.2, 129.7, 126.1, 125.9, 123.2, 120.4, 111.2, 104.2, 70.6, 63.5, 47.2, 46.9, 43.2, 27.4, 20.3, 16.4, 13.6. IR (ATR) ν_{\max} : 3385, 2959, 1738, 1683, 1649, 1582, 1549, 1380, 1352, 1228, 1046 cm⁻¹. ESI-LCMS: calcd. for C₂₄H₂₈N₂O₅S₂ 488.14, found 489.17 (M+H).

RAFT polymerization of VClAc using CTA-2, Napht-PVA

A clean and dry 10 mL Schlenk flask was charged with 2 mL of VClAc (250 eq., 19.8 mmol), CTA-2 (1 eq., 39 mg, 0.079 mmol), initiator (0.2 eq., 0.016 mmol, AIBN) and dioxane (10 v/v%, 0.22 mL). The flask was deoxygenated by three freeze-pump-thaw cycles, back-filled with argon and immersed in an oil bath at 60 °C. The monomer conversion was checked by ¹H NMR (CDCl₃) and the reaction stopped by exposure to air after 116 h at 22 % conversion. The reaction mixture was diluted with THF and the polymer precipitated in pentane three times. GPC (THF, PMMA standard): M_n = 6200, DP = 47, D = 1.34. ¹H NMR (CHCl₃, 400 MHz): δ 8.60 (d, J = 7.4 Hz, 1H), 8.48 (d, J = 8.6 Hz, 1H), 7.67 (t, J = 7.4 Hz, 1H), 6.72 (m, 2H), 4.93 (b, 103H), 4.66 (m, 3H), 4.11 (b, 232H), 1.93 (b, 237H), 0.98 (d, J = 6.8 Hz, 6H).

The polymer was hydrolyzed by dissolving 50 mg in 5 ml THF/MeOH followed by addition 10 mg K₂CO₃ and stirred for 2 h at RT. The solvent was removed under reduced pressure. The yellow-orange product was redissolved in water and dialyzed (CE, 100-500 Da MWCO) to remove residual salt. ¹H NMR (*d*₆-DMSO, 400 MHz): δ 8.75 (d, J = 7.7 Hz, 1H), 8.45 (d, J = 7.1 Hz, 1H), 8.28 (d, J = 8.0 Hz, 1H), 7.83 (m, 1H), 7.69 (t, J = 7.7 Hz, 1H), 6.83 (d, J = 8.8 Hz, 1H), 4.54 (b, 54H), 3.84 (b, 59H), 1.37 (b, 139), 0.98 (d, J = 6.6 Hz, 6H).

3.6 References

1. Venketesh, S.; Dayananda, C. *Crit. Rev. Biotechnol.* **2008**, *28*, 57-82.
2. Buckley, S.L.; Lillford, P.J. *Modern Biopolymer Science - Chapter 3*, **2009**, Elsevier, ISBN 978-0-12-374195-0.
3. Gibson, M.I. *Polym. Chem.* **2010**, *1*, 1141-1152.
4. Garner, J.; Harding, M.M. *Chem. Bio. Chem.* **2010**, *11*, 2489-2498.
5. Peltier, R.; Brimble, M.M.; Wojnar, J.M.; Williams, D.E.; Evans, C.W.; DeVries, A.L. *Chem. Sci.* **2010**, *1*, 538-551.
6. Budke, C.; Koop, T. *Chem. Phys. Chem.* **2006**, *7*, 2601-2606.
7. Inada, T.; Lu, S.S. *Cryst. Growth Des.* **2003**, *3*, 747-752.
8. Congdon, T.; Notman, R.; Gibson, M.I. *Biomacromolecules* **2013**, *14*, 1578-1586.
9. Deller, R.C.; Vatish, M.; Mitchell, D.A.; Gibson, M.I. *Nat. Commun.* **2014**, *5*, 3244.
10. Inada, T.; Modak, P.R. *Chem. Eng. Sci.* **2006**, *61*, 3149-3158.
11. Inada, T.; Lu, S.S. *Chem. Phys. Lett.* **2004**, *394*, 361-365.
12. Yamada, K.; Nakano, T.; Okamoto, Y. *Polym. J.* **1998**, *30*, 641-645.
13. Shim, S.H.; Ham, M.K.; Huh, J.; Kwon, Y.K.; Kwark, Y.J. *Polym. Chem.* **2013**, *4*, 5449-5455.
14. Ohgi, H.; Sato, T. *Macromolecules* **1999**, *32*, 2403-2409.
15. Nagara, Y.; Yamada, K.; Nakano, T.; Okamoto, Y. *Polym. J.* **2001**, *33*, 534-539.
16. Imai, K.; Shiomi, T.; Tezuka, Y.; Kawanishi, T.; Jin, T. *J. Polym. Sci. A* **1988**, *26*, 1961-1968.
17. Morrison E.D.; Gleason, E.H.; Stannett, V. *J. Polym. Sci.* **1959**, *36*, 267-273.
18. Santee, G.F.; Marchessault, R.H.; Clark, H.G.; Kearny, J.J.; Stannett, V. *Die Makromolekulare Chemie* **1964**, *73*, 177-187.
19. Litt, M.; Stannett, V. *Die Makromolekulare Chemie* **1960**, *37*, 19-24.
20. Kamachi, M.; Satoh, J.; Liaw, D.J. *Polymer Bulletin* **1979**, *1*, 581-584.
21. Stals, P.J.M. *Single-chain polymeric nanoparticles: from design to function*. PhD thesis, Eindhoven University of Technology, The Netherlands.
22. Repollet-Pedrosa, M.H.; Weber, R.L.; Schmitt, A.L.; Mahanthappa, M.K. *Macromolecules* **2010**, *43*, 7900-7902.
23. Bardajee, G.R.; Li, A.Y.; Haley, J.C.; Winnik, M.A. *Dyes and Pigments* **2008**, *79*, 24-32.
24. Meister, K.; Lotze, S.; Olijve, L.L.C.; DeVries, A.L.; Duman, J.G.; Voets, I.K.; Bakker, H.J. *J. Phys. Chem. Lett.* **2015**, *6*, 1162-1167.
25. Tesei, G.; Paradossi, G.; Chiessi, E. *J. Phys. Chem. B* **2014**, *118*, 6946-6955.
26. Konrad Meister, personal communication (unpublished).
27. Todde, G.; Hovmöller, S.; Laaksonen, A. *J. Phys. Chem. A* **2015**, *119*, 3407-3413.

Chapter 4

A molecular bottlebrush that blocks ice growth

Abstract

Molecular bottlebrushes are densely grafted copolymers with an extended brush-like shape. In this study, the synthesis of molecular brushes with poly(vinyl alcohol) (PVA) side chains is described, via a combination of atom-transfer radical polymerization (ATRP) and reversible addition-fragmentation chain-transfer (RAFT) polymerization. The facile preparation of PVA brushes is performed via the selective hydrolysis of the chloroacetate esters of the poly(vinyl chloroacetate) (PVClAc) side chains of a PVClAc precursor brush. Small angle X-ray scattering (SAXS) experiments and atomic force microscopy (AFM) demonstrate a highly extended topology of the PVA brush. Analysis of the antifreeze activity shows that densely grafting PVA side chains on a rigid polymer backbone does not increase the ice recrystallization inhibition (IRI) activity significantly compared to linear PVA.

4.1 Introduction

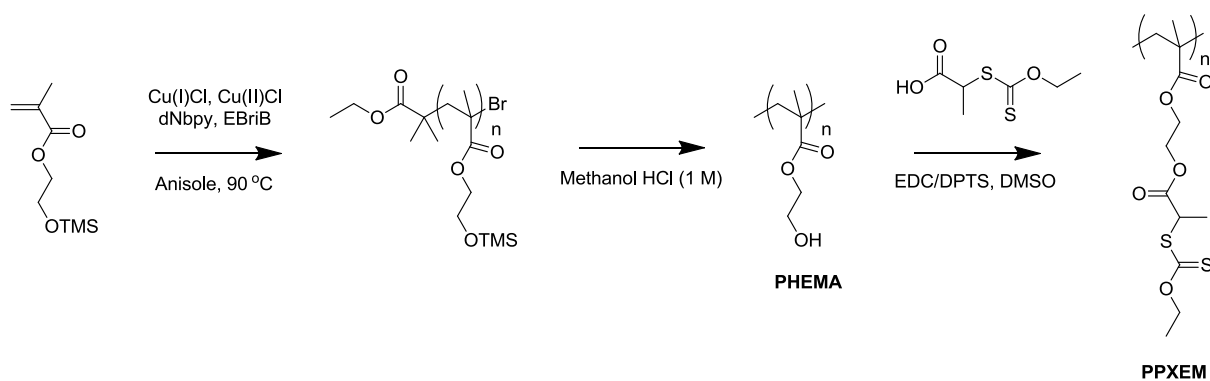
Molecular bottlebrushes are a class of copolymers with an extended rod-like topology due to steric repulsion of the densely grafted side-chains.^{1,2} These brush polymers have gained a lot of interest for applications ranging from super soft elastomers³ to stimuli responsive molecules,^{4,5} because of their unique macromolecular architecture. Nese *et al.* developed an efficient procedure to prepare molecular brushes of vinyl acetate (VAc) and other vinyl monomers, using a combination of atom-transfer radical polymerization (ATRP) and reversible addition-fragmentation chain-transfer (RAFT) polymerization.^{6,7} However, the PVAc side chains of the molecular brush could not be hydrolyzed to prepare poly(vinyl alcohol) (PVA) bottlebrushes due to the presence of multiple ester bonds.

This study describes the synthesis of PVA molecular bottlebrushes via the selective hydrolysis of chloroacetate esters of grafted poly(vinyl chloroacetate) (PVClAc) side chains. As a precursor for the brush backbone, poly(2-hydroxyethyl methacrylate) (PHEMA) with narrow molecular weight distribution was prepared by ATRP, followed by esterification of the hydroxyl groups with xanthate moieties to form the macroCTA poly(2-propionyloxyethylxanthateethyl methacrylate) (PPXEM). Poly(vinyl chloroacetate) (PVClAc) side chains were grafted on the PPXEM backbone using RAFT to generate PPXEM-*g*-PVClAc brushes. The rate of chloroacetate ester cleavage is known to be 760 times faster than the cleavage rate of acetate esters,⁸ which allows for the selective hydrolysis of the PPXEM-*g*-PVClAc brush precursor under mild conditions for the preparation of PVA brushes. The macromolecular structure of the PVA brushes in solution is characterized using small angle X-ray scattering (SAXS) and atomic force microscopy (AFM), showing that the PVA brushes have a rod-like topology. Furthermore, the antifreeze activity of the PVA brushes is studied to determine the effect of densely grafted PVA side chains on the multivalent ice-PVA interaction compared to linear PVA polymers.

4.2 Results

4.2.1 ATRP of TMS-hydroxyethyl methacrylate and preparation of macro-CTA

The reaction conditions and stoichiometry of reagents for the ATRP polymerization of HEMA-TMS were chosen according to an adapted procedure from the Matyjaszewski group. The original procedure was developed to target high molecular weight, involving halogen exchange to improve initiation efficiency. The initial stoichiometry of the reagents was: [HEMA-TMS] : [EBriB] : [CuCl] : [CuCl₂] : [dNbpy] = 400 : 1 : 2 : 0.2 : 4.4, with 10 v/v% anisole at $T = 90$ °C (Scheme 1). Monomer conversion was monitored by ¹H NMR (Figure 1), showing a constant concentration of active propagating species based on the linearity of a semilogarithmic kinetic plot of $\ln([M]_0/[M])$ vs. time (Figure 1B). Once the polymerization kinetics were determined, a new polymerization reaction was set-up, which was quenched at 42 % monomer conversion. The copper catalyst was removed by passing the reaction mixture through a silica column. Deprotection of the TMS-groups in methanolic HCl yielded PHEMA with a molecular weight of $M_n = 17.000$, DP = 129 and $M_w/M_n = 1.08$.



Scheme 1: Synthesis of the macro-CTA poly(2-propionyloxyethylxanthateethyl methacrylate) (PPXEM).

The esterification of PHEMA with xanthogenic acid (XA) into PPXEM was performed via EDC/DPTS coupling (Scheme 1). Nearly full conversion was observed from the ¹H NMR spectrum (Figure 2), and the GPC analysis yielded a molecular weight of $M_n = 37.400$, DP = 121 and $M_w/M_n = 1.56$. The increase in dispersity arises from a shoulder towards shorter retention time in the GPC trace, probably due to a very small amount of crosslinking (not observable with ¹H NMR) or interactions of PPXEM with the column.

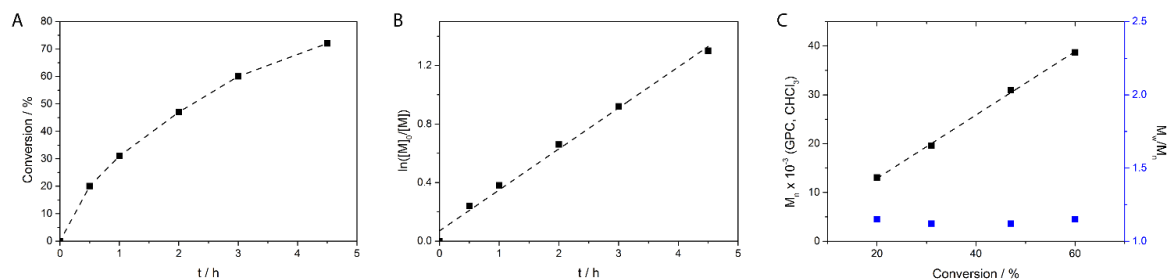


Figure 1: ATRP of HEMA-TMS, with (A) monomer conversion determined by ^1H NMR, (B) semilogarithmic kinetic plot and (C) evolution of M_n and M_w/M_n as a function of monomer conversion.

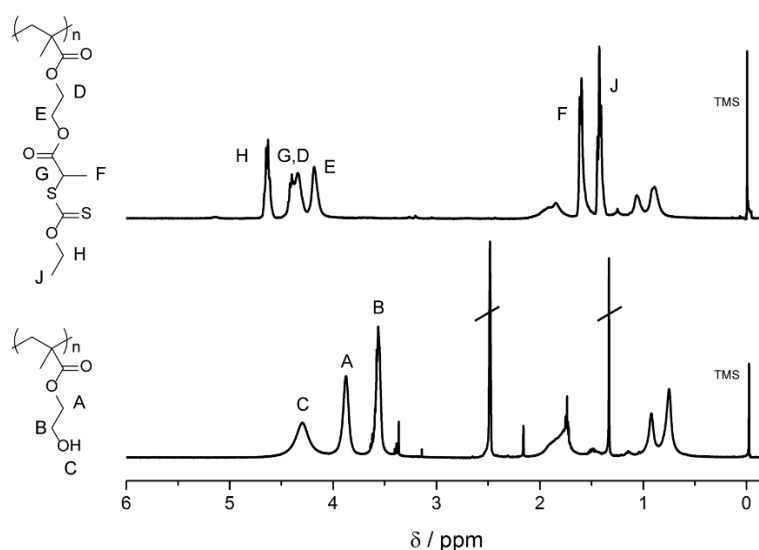
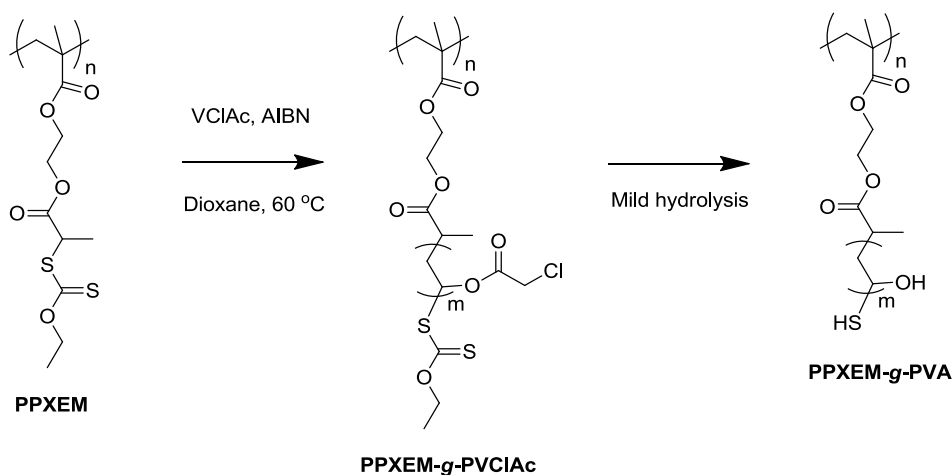


Figure 2: ^1H NMR of PPXEM (top) and PHEMA (bottom) measured in CDCl_3 and d_6 -DMSO respectively.

4.2.2 Preparation of PPXEM-g-PVA polymer brushes

PVA bottlebrushes were synthesized by the selective hydrolysis of the PVClAc side chains of PPXEM-g-PVClAc brushes. RAFT polymerization of the PVClAc side chains using PPXEM as macro-CTA was performed using AIBN (0.2 eq. per XA, **3**) as initiator and 250 eq. of monomer per XA in 10 v/v% dioxane. The reaction was allowed to continue for 6 h at 60 °C until 42 % conversion, corresponding to a theoretical degree of polymerization of $\text{DP} \sim 105$ of the PVClAc side chains. The reaction mixture was already highly viscous at 42 % conversion. The polymer was precipitated in pentane and dialyzed (THF, 12-14 kDa MWCO). The GPC (THF) shows two peaks with peak maxima at $t_{\text{top}} = 11.02$ min (AUC = 6.9 %, $M_n = 471.800$, $M_w/M_n = 1.07$) and $t_{\text{top}} = 14.16$ min (AUC = 93.1 %, $M_n = 11.500$, $M_w/M_n = 1.94$). The first peak ($M_n = 471.800$) corresponds to the apparent molecular weight of the molecular brush. Even though the estimated molecular weight calculated from the monomer conversion is $M_n =$

1.672.000. This rather low apparent M_n in GPC was also observed for PPXEM-*g*-PVAc molecular brushes by Nese *et al.*, in which they found $M_{n,NMR} = 1.880.000$ and $M_{n,GPC} = 315.000$.⁶ The origin of the second peak in the GPC trace at $t_{top} = 14.16$ min ($M_n = 11.500$) might originate from the brush-like structure and/or interactions of the chlorine groups of the polymer side chains with the column.



Scheme 2: Synthesis of PVA brush (PPXEM-*g*-PVA), with degree of polymerization of the polymer backbone $n \sim 129$ and side chains $m \sim 105$.

Table 1: Molecular weight and polymer dispersity data of the polymer backbone and PVA brush precursor. Molecular weights^a were calculated from monomer conversion by ¹H NMR. GPC data with DMF^b (relative to PEO standards) and THF^c (relative to PMMA standards) as eluent.

		M_n MNR ^a	M_n GPC	DP	M_w/M_n
1	PHEMA	16.800	17.000 ^b	129	1.08
2	PPXEM	39.700	37.400 ^c	121	1.56
3	PPXEM- <i>g</i> -PVClAc	1.672.000	471.800 ^c	129 – 105 ^a	1.07

Next, the PPXEM-*g*-PVClAc brush was hydrolyzed under mild conditions using THF/MeOH/K₂CO₃ at room temperature to yield PPXEM-*g*-PVA (Scheme 2). ¹H NMR spectra of the initial PPXEM-*g*-PVClAc show quantitative hydrolysis of the chloroacetate groups **a** and **b** ($\delta = 4.88$ and 4.31 ppm), and the OH triad **d** ($\delta = 4.58$ ppm) of the final PPXEM-*g*-PVA brush (Figure 3). Using the length of the polymer backbone consisting of 129 monomers each with a graft comprising 105 units, the molecular weight of the PVA bottlebrush is calculated to be $M_n = 635.700$.

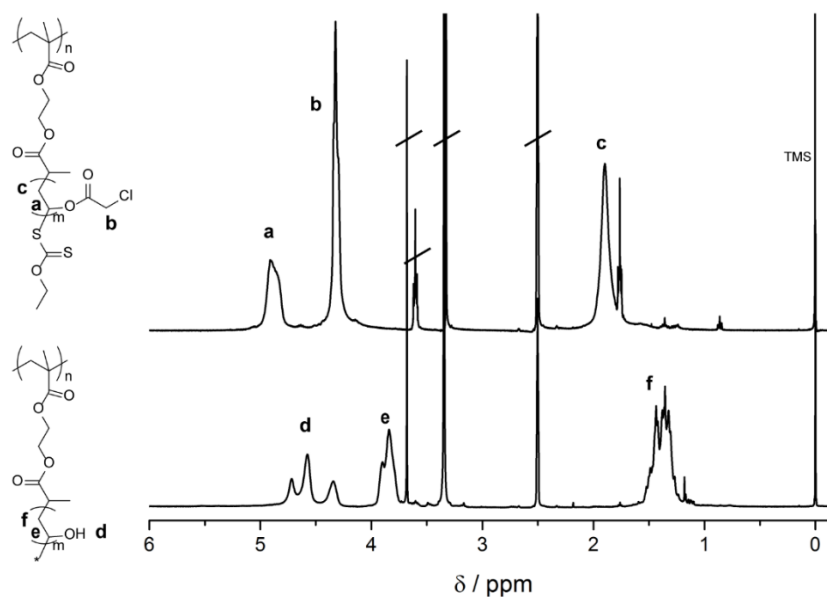


Figure 3: ^1H NMR of PPXEM-*g*-PVClAc (top) and PPXEM-*g*-PVA (bottom) measured in d_6 -DMSO.

4.2.3 Structural characterization of the PVA molecular bottlebrush

The macromolecular structure and dimensions of the PVA bottlebrushes were further characterized using small angle X-ray scattering (SAXS). Based on the length of the C-C-C monomeric unit in tetrahedral configuration ($l_0 = 0.25 \text{ nm}$)⁶ and a backbone DP = 129, the estimated number-average contour length of the PVA brush is approximately $l_n = 32 \text{ nm}$. Synchrotron SAXS data of the PVA molecular bottlebrush were obtained on the BM29 beamline (ESRF, Grenoble, France) (Figure 4). The accessible q -range does not cover the full scattering profile of the PVA brush, and low- q data points needed to provide a reliable Guinier analysis to extract the radius of gyration (R_g) and molecular weight ($M_{w,SAXS}$) are missing. However, two power law regimes are apparent in the scattering profile: a low q regime where the intensity falls off with $q^{-0.6}$, followed by an intermediate regime where the intensity falls off with $q^{-1.7}$, indicative of a highly elongated object. The experimental SAXS data can be described by an elliptical cylinder model, with a minimal length $l = 26.4 \pm 0.2 \text{ nm}$, semiminor axis $a = 0.15 \pm 1.1 \text{ nm}$ and semimajor axis $b = 3.8 \pm 28.9 \text{ nm}$. Even though the estimated length of the form factor analysis is close to the number-average contour length of the PVA brush, essential low q data points are missing to give an exact estimation. Also, we cannot yet exclude a significant contribution of polydispersity, which could explain the large error on the estimated parameters of the form factor modeling of the SAXS profiles. Furthermore, low contrast of the PVA side chains, which makes them less visible by X-ray scattering, could give rise to an underestimation of the cylinder cross-section.

In atomic force microscopy (AFM) experiments, conglomerates of highly extended, stiff rods with a length of approximately $l = 100 \text{ nm}$ are observed (Figure 5). The height profile

of a single rod (Figure 5B) shows a width of $b = 15$ nm and height of $h = 1$ nm. Single polymer rods are difficult to observe in the AFM images, which may be due to the sticky and crystalline nature of the PVA side chains, resulting in the formation of conglomerates during sample preparation.

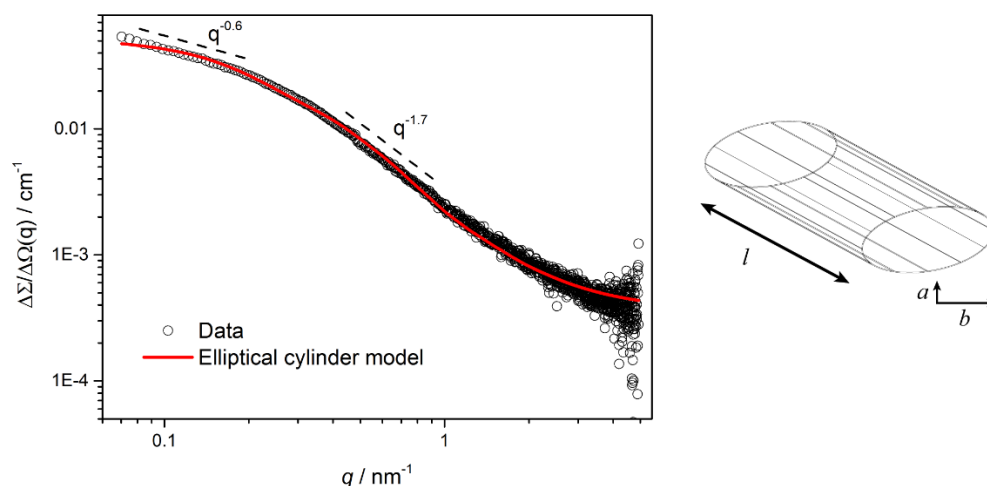


Figure 4: Small angle X-ray scattering data (symbols) and fit of an elliptical cylinder model (red line), with length l and elliptical cross section with semiminor axis a and semimajor axis b .

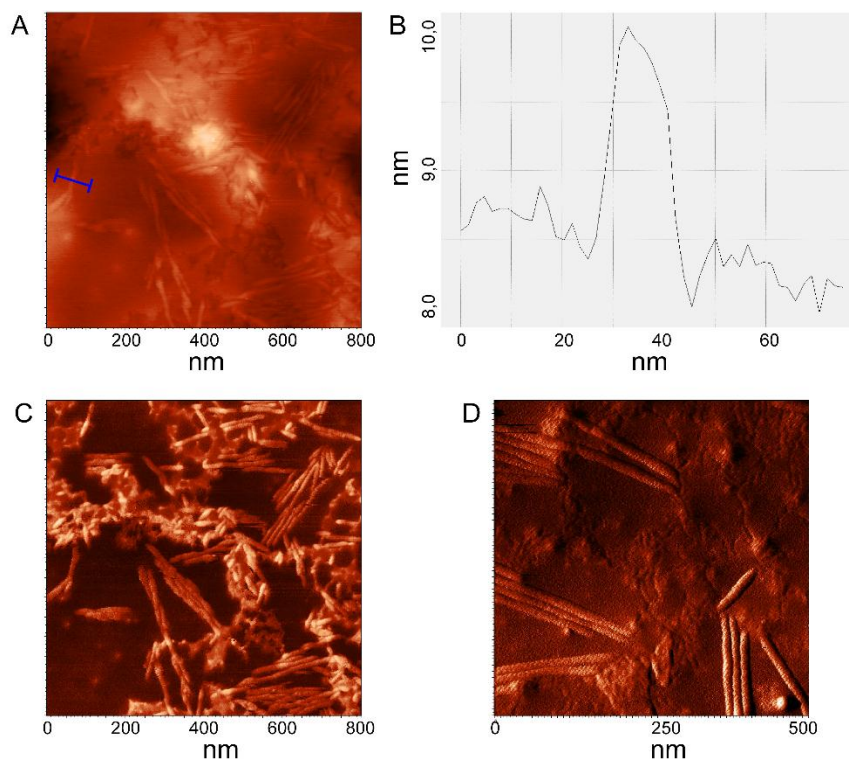


Figure 5: Atomic force microscopy (AFM) images of the PVA brushes. (A) Height image with in blue the marked region which is used to plot the height profile of single rod (B), (C) phase image, and (D) zoomed-in phase image. PVA brushes (0.1 mg/ml in pure water) were cast on a highly ordered pyrolytic graphite (HOPG) substrate and the solvent was evaporated under a nitrogen stream.

4.2.4 Antifreeze activity of the PVA molecular bottlebrush

The antifreeze activity of PPXEM-*g*-PVA was studied using ice recrystallization inhibition (IRI) experiments (Figure 6) and sonocrystallization measurements (Figure 7). PPXEM-*g*-PVA effectively inhibits the recrystallization of ice down to a concentration of 0.5 mg/ml (concentration VA monomers $c_{VA} = 11$ mM). This shows that on weight basis, the PVA brush (DP PVA side chain = 109) is slightly less active than the linear PVA-1 (DP = 178), which is active down to ~ 0.2 mg/ml ($c_{VA} = 5$ mM). This implies that if the PVA chain is long enough (DP > 100), the affinity of PVA to the ice surface is sufficient to inhibit ice recrystallization, and is hardly influenced by polymer architecture.

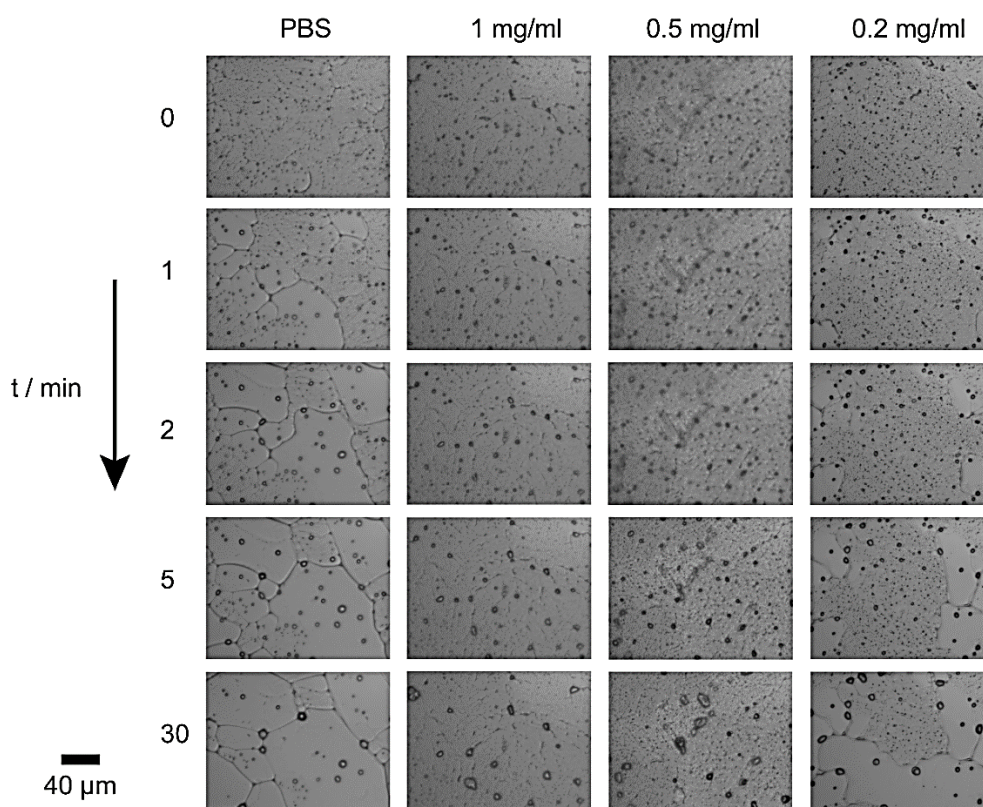


Figure 6: Ice recrystallization inhibition experiments of PPXEM-*g*-PVA, measured in PBS buffer.

Sonocrystallization measurements of PPXEM-*g*-PVA at concentrations of 1, 3 and 5 mg/ml show a stable freezing plateau similar to a buffer solution after initiation of the ice nucleation, and no lowering of the non-equilibrium freezing point (Figure 7A). Mixed with 1 mg/ml type III AFP (rQAE isoform), only minimal lowering of non-equilibrium freezing plateau is observed; 0.03, 0.07 and 0.09 °C for 1, 3 and 5 mg/ml of PVA brush, respectively (Figure 7B). The non-existence of TH activity of the PVA brushes in sonocrystallization experiments is in line with linear PVA polymers (chapter 3).

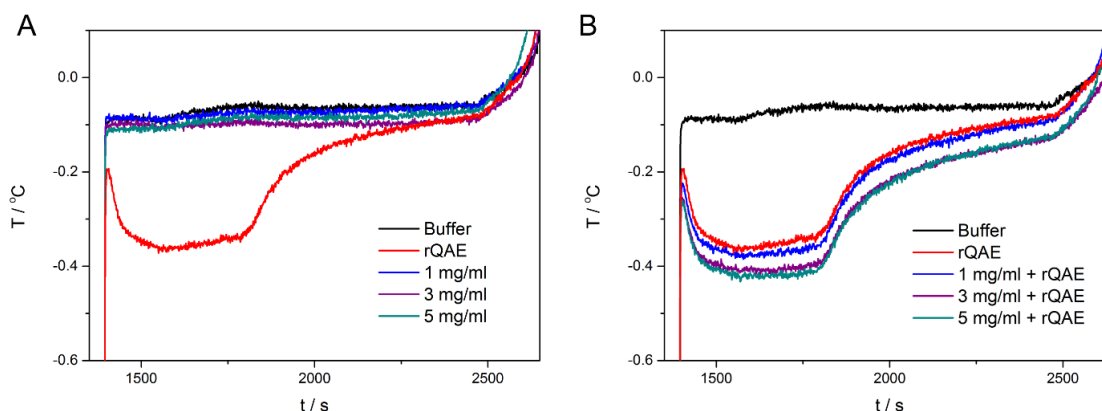


Figure 7: Sonocrystallization experiments of (A) PPXEM-*g*-PVA and (B) PPXEM-*g*-PVA mixed with 1 mg/ml type III AFP (rQAE isoform). All samples are measured in 20 mM Tris pH 7.5.

4.3 Discussion

Linear polymer chains of poly(vinyl alcohol) effectively inhibit the recrystallization of ice (chapter 3). The ice-PVA interaction is proposed to occur via multiple hydrogen bonds, with longer polymer chains binding stronger to ice than shorter chains. In an attempt to enhance the adhesion of PVA to ice surfaces, in this study we prepared PVA molecular bottlebrushes with densely grafted PVA side chains on a rigid polymer backbone using a combination of atom-transfer radical polymerization (ATRP) and reversible addition-fragmentation chain-transfer (RAFT) polymerization. PVA molecular bottlebrushes were successfully prepared via the selective hydrolysis of chloroacetate esters of a PVCIAc precursor brush. The macromolecular structure of the PVA brush in solution was characterized using small angle X-ray scattering (SAXS) and atomic force microscopy (AFM), showing a highly extended topology.

The PVA brush was found to inhibit the recrystallization of ice down to a concentration of 0.5 mg/ml, which is on molar concentration of the VA monomers ($c_{VA} = 11$ mM) less active than linear PVA ($c_{VA} = 5$ mM). These results show that the length of the PVA chain is important for IRI activity, and thus the interaction between PVA and the ice surface. A polymer architecture of densely grafting PVA side chains on a rigid polymer backbone hardly influences the antifreeze activity of PVA. This conclusion might be confirmed by synthesizing PVA brushes with a side chain length of DP = 20.

4.4 Conclusion

Molecular brushes are a special class of copolymers with densely grafted side chains, resulting in a rigid topology. In this study, the synthesis of a poly(vinyl alcohol) molecular brush is described. A macro-CTA was prepared using ATRP, and subsequently PVClAc side chains were polymerized via RAFT, followed by mild hydrolysis of the chloroacetate esters. The macromolecular structure of the PVA molecular brushes in solution was characterized using SAXS, showing the formation of a highly elongated object. The densely grafted PVA side chains of the bottlebrush were proposed to enhance the ice-PVA interaction via multivalent hydrogen bonding of the hydroxyl groups. However, compared to linear PVA no significant increase in antifreeze activity was observed.

4.5 Materials and methods

Chemicals and materials

All commercial reagents were purchased from Sigma Aldrich and used as received without further purification, unless stated otherwise. Vinyl ester monomers were purified by passing through basic alumina prior to polymerization. Azobisisobutyronitril (AIBN, Sigma Aldrich) was recrystallized from methanol. N-ethyl-N'-(3-dimethylaminopropyl)carbodiimide hydrochloride (EDC) was purchased from Iris Biotech. Deuterated solvents were obtained from Cambridge Isotope Laboratories and dried over molsieves. All solvents were of AR quality and purchased from Biosolve. All polymerization reactions were performed using a 10 mL Schlenk flask (Chemglass, AF-0520-20). Reactions were followed by thin-layer chromatography (precoated 0.25 mm, 60-F254 silica gel plates from Merck).

Instrumentation

Flash chromatography was performed using an automatic flash chromatography instrument Biotage Isolera One equipped with biotage SNAP KP-Sil silica cartridges. NMR spectroscopy was performed on a Varian Mercury Vx 400 MHz and/or Varian 400MR, operating at 400 MHz for ^1H and 100 MHz for ^{13}C . Chemical shifts are reported in ppm (δ) values relative to tetramethylsilane (TMS) or residual solvent. Splitting patterns are labeled as s, singlet; d, doublet; dd, double doublet; t, triplet; q, quartet; q, quintet; m, multiplet and b stands for broad. Matrix assisted laser desorption/ionisation (MALDI) mass spectra were obtained on a PerSeptive Biosystems Voyager DE-PRO spectrometer or Bruker autoflex speed spectrometer using α -cyano-4-hydroxycinnamic acid (CHCA) and *trans*-2-[3-(4-tert-butylphenyl)-2-methyl-2-propenyldiene]malononitrile (DCTB) as matrices. IR spectra were recorded on a Perkin-Elmer FTIR Spectrum 2 spectrometer equipped with a Perkin-Elmer Universal ATR Sampler Accessory. DMF-GPC measurements were carried out on a PL-GPC-50 plus from Polymer Laboratories (Agilent Tech.) with refractive index detector working in DMF containing 10 mM LiBr at 50 °C at a constant flow rate of 1 mL/min on a Shodex GPC-KD-804 column (exclusion limit = 400 kDa; 0.8 cm i.d. \times 300 mL), which was calibrated with polyethyleneoxide (PEO) standards with a range from 282 – 77350 Da (Polymer Laboratories, Agilent Tech.). THF-GPC measurements were performed on a Shimadzu-system (Prominence i LC-2030C 3D) equipped with two Agilent Technology columns in series (PLgel 5 μm mixed C [200-2.000.000 Da] and PLgel 5 μm mixed D [200-40.000 Da]), a RI detector and a PDA detector, with THF as eluent at 40 °C and a constant flow rate of 1 mL/min. The system was calibrated with polystyrene (PS) samples with a range of 580-100.000 Da (Polymer Laboratories). The morphology of the molecular brushes are investigated by Atomic Force Microscopy (AFM) by means of topography as well as phase imaging. The material is drop cast on a Highly Ordered Pyrolytic Graphite (HOPG). The measurements are performed in tapping mode on a NTegra Aura (NT-MDT) using a Hi'Res C14/Cr-Au cantilever

(Micromasch) with a typical spike radius of 1nm, spring constant 5N/m and resonance frequency of 160KHz. Synchrotron radiation X-ray scattering data was collected at the BM29 BioSAXS beamline of the ESRF (Grenoble, France) operating at 12.5 keV. The scattering intensity was measured as a function of momentum transfer vector $q = 4\pi(\sin\theta)/\lambda$, where $\lambda = 0.992 \text{ \AA}$ is the radiation wavelength and 2θ is the scattering angle. The beamsize was set about $700 \mu\text{m} \times 700 \mu\text{m}$ and two-dimensional scattering profiles were collected using a Pilatus 1M detector. Samples were measured at a fixed sample-to-detector distance of 2.867 m to cover an angular range of $0.03 - 5 \text{ nm}^{-1}$. Samples were loaded via an automated sample changer and flowed through a quartz capillary 1.8 mm in diameter, while collecting 10 frames of 0.1 s with a reduced flux of 10^{12} ph/s. The averaged value of buffer scattering measured before and after the sample measurements was subtracted from the averaged sample scattering curve. Samples were measured at 5 mg mL^{-1} and the scattering profiles were brought to absolute scale using the known scattering cross-section per unit sample volume, $d\Sigma/d\Omega(0)$, of water and verified using a BSA protein standard.

Preparation of copper chlorides

Copper(I) chloride - In a 100 mL beaker, a solution was prepared of 6 g of powdered $\text{CuSO}_4 \cdot 5\text{-hydrate}$ and 1.8 g of NaCl in 20 mL of hot water. A solution of 1.4 g of NaHSO_3 and 0.9 g of NaOH in 10 mL water was added dropwise to the stirring copper sulfate solution. The cuprous chloride was allowed to settle and the liquid decanted. The precipitated cuprous chloride was washed two times with water by decantation, subsequently filtered and washed with ethanol and diethyl ether. The cuprous chloride is obtained as a white powder that darkens green-brown on exposure to air. *Copper(II) chloride* - CuCl_2 hydrate was dried in a vacuum oven over P_2O_5 at 80-100 °C for 2-3 h, resulting in brown crystals. Copper chlorides were stored under argon in a dessicator.

Poly(hydroxyethyl methacrylate) using ATRP, PHEMA

A clean and dry 10 mL Schlenk flask was charged with HEMA-TMS (400 eq., 5 mL, 22.93 mmol), 4,4'-dinonyl-2,2'-dipyridyl (dNbpy, 4.4 eq., 103 mg, 0.252 mmol), CuCl (2 eq., 11 mg, 0.115 mmol), CuCl_2 (0.2 eq., 1.5 mg, 11 mmol), and anisole (10 v/v%, 0.56 ml). The flask was deoxygenated by three freeze-pump-thaw cycles. After the final cycle, the flask was filled with argon and ethyl- α -bromoisobutyrate (EBriB, 1 eq., 8.4 μL , 0.057 mmol) was quickly added, followed by another FPT-cycle. The flask was again back-filled with argon and immersed in an oil bath at 90 °C. The reaction was stopped after 1.5 h at 42 % monomer conversion (^1H NMR, CDCl_3) via exposure to air. GPC (CHCl_3 , PMMA standard): $M_{n,\text{GPC}} = 22.300$, $\text{DP} = 109$, $D = 1.10$. The reaction mixture was diluted with chloroform and the copper was removed by passing the reaction mixture through a silica column. The chloroform was removed under reduced pressure, after which 20 mL methanol was added to the reaction aliquote and 1.7 mL of 37 % HCl solution to give a final 1 M methanolic HCl solution to deprotect the TMS groups.

The reaction mixture was stirred overnight at RT, after which the solution was neutralized by the addition of 1.7 mL of a 1 M NaOH solution and the methanol removed under vacuum. The final polymer solution was precipitated in THF and dried under vacuum. GPC (DMF, PEO standard): $M_n = 17.000$, $DP = 129$, $M_w/M_n = 1.08$. $^1\text{H NMR}$ (DMSO, 400 MHz): δ 4.29 (b, 1H, OH), 3.88 (b, 2H, $\text{CH}_2\text{CH}_2\text{OH}$), 3.57 (b, 2H, $\text{CH}_2\text{CH}_2\text{OH}$), 1.77 (b, 2H, $\text{CH}_2\text{C}(\text{CH}_3)\text{C}=\text{O}$), 0.92, 0.76 (b, 3H, $\text{CH}_2\text{C}(\text{CH}_3)\text{C}=\text{O}$).

Poly(2-propionyloxyethylxanthateethyl methacrylate), PPXEM

PHEMA (0.5 g, 3.77 mmol HEMA unit), DPTS (1.11 g, 3.77 mmol) and XA (2.2 g, 11.31 mmol) were dissolved in 20 mL dry DMSO. EDC (1.95 g, 10.18 mmol) in 5 mL chloroform was added dropwise to the reaction mixture and left to stir for 2 days at RT. Chloroform (150 mL) was added to the reaction mixture and the solution was washed with twice with 1 % NaHCO_3 solution and four times with water (100 mL). The organic layer was dried over MgSO_4 and the chloroform was removed under reduced pressure. The polymer was precipitated in pentane three times. The final product was stored at 4 °C in chloroform and only dried directly before use. Nearly full functionalization was observed by $^1\text{H NMR}$ (CDCl_3). A small shoulder is present in the GPC trace attributed to minimal crosslinking, which is not observable by $^1\text{H NMR}$. GPC (THF, PMMA standard): $M_{n,\text{GPC}} = 37.400$, $DP = 121$, $M_w/M_n = 1.56$. $^1\text{H NMR}$ (CHCl_3 , 400 MHz): δ 4.63 (b, 2H, $\text{CH}_3\text{CH}_2\text{O}$), 4.35 (b, 2H + 1H, $\text{OCH}_2\text{CH}_2\text{O} + \text{SCH}(\text{CH}_3)\text{C}=\text{O}$), 4.17 (b, 2H, $\text{OCH}_2\text{CH}_2\text{O}$), 1.85 (b, 2H, $\text{CH}_2\text{C}(\text{CH}_3)\text{C}=\text{O}$), 1.61 (d, $J = 6.6$ Hz, 3H, $\text{SCH}(\text{CH}_3)\text{C}=\text{O}$), 1.42 (t, $J = 7.1$ Hz, 3H, $\text{CH}_3\text{CH}_2\text{O}$), 1.06, 0.89 (b, 3H, $\text{CH}_2\text{C}(\text{CH}_3)\text{C}=\text{O}$).

PPXEM-g-PVA

A clean and dry 10 mL Schlenk flask was charged with 2 mL VClAc (250 eq. of XA group, 19.8 mmol), PPXEM (24 mg, 0.079 mmol XA group), AIBN (0.2 eq. of XA group, 2.6 mg, 0.016 mmol) and dioxane (10 v/v%, 0.22 mL). The flask was deoxygenated by three freeze-pump-thaw cycles, back-filled with argon and immersed in an oil bath at 60 °C. The reaction progress was followed by $^1\text{H NMR}$ and stopped after 6 h at 42 % conversion. The polymer was precipitated in pentane three times and dialyzed (THF, Spectrapor RC-membrane 12-14 kDa MWCO). The polymer was dried under high vacuum for 3-4 h, and the resulting product had a solid white appearance. GPC (THF, PMMA standard): $M_n = 471.800$, $M_w/M_n = 1.07$. $^1\text{H NMR}$ (CHCl_3 , 400 MHz): δ 4.95 (b, 1H, CH_2CHO), 4.10 (b, 2H, $\text{ClCH}_2(\text{C}=\text{O})$), 1.92 (b, 2H, CH_2CHO).

The polymer was hydrolyzed by dissolving 50 mg in 5 mL THF/MeOH followed by addition 10 mg K_2CO_3 and stirred for 2 h at RT. The solvent was removed under reduced pressure. The yellow-orange product was redissolved in water and dialyzed (CE, 100-500 Da MWCO) to remove residual salt. $^1\text{H NMR}$ (d_6 -DMSO, 400 MHz): δ 4.72 mm, 4.58 mr, 4.34 rr (triad, 1H, OH), 3.84 (b, 1H, CH_2CHOH), 1.37 (b, 2H, CH_2CHOH).

4.6 References

1. Sheiko, S.S.; Sumerlin, B.S.; Matyjaszewski, K. *Prog. Polym. Sci.* **2008**, *33*, 759-785.
2. Gregory, A.; Stenzel, M.H. *Prog. Polym. Sci.* **2012**, *37*, 38-105.
3. Pakula, T.; Zhang, Y.; Matyjaszewski, K.; Lee, H.I.; Boerner, H.; Qin, S.; Berry, G.C. *Polymer* **2006**, *47*, 7198-7206.
4. Li, C.; Gunari, N.; Fischer, K.; Janshoff, A.; Schmidt, M. *Angew. Chem. Int. Ed.* **2004**, *42*, 1101-1104.
5. Lee, H.I.; Pietrasik, J.; Sheiko, S.S.; Matyjaszewski, K. *Prog. Polym. Sci.* **2010**, *35*, 24-44.
6. Nese, A.; Kwak, Y.; Nicolaj, R.; Barrett, M.; Sheiko, S.S.; Matyjaszewski, K. *Macromolecules* **2010**, *43*, 4016-4019.
7. Nese, A.; Li, Y.; Averick, A.; Kwak, Y.; Konkolewicz, D.; Sheiko, S.S.; Matyjaszewski, K. *ACS Macro Lett.* **2012**, *1*, 227-231.
8. Repollet-Pedrosa, M.H.; Weber, R.L.; Schmitt, A.L.; Mahanthappa, M.K. *Macromolecules* **2010**, *43*, 7900-7902.

Chapter 5

A new structural model of a 34 kDa dimeric type I antifreeze protein

Abstract

Antifreeze proteins (AFPs) allow fish living in icy polar waters to avoid freezing. A 34 kDa dimeric “hyperactive” type I antifreeze protein (hypAFP1) with unusually high thermal hysteresis (TH) activity in comparison to all other antifreeze proteins in fish was discovered in the winter flounder. We have measured the size and shape of this highly potent AFP by using small angle X-ray scattering (SAXS). Our results show that hypAFP1 adopts a long cylindrical shape with a length of 20 ± 2 nm and a diameter of 2.2 ± 0.1 nm, which means that hypAFP1 does not form a fully extended helical dimer in solution. These findings call for a revision of the structural model of hypAFP1 and the concept of a flat, threonine-rich ice binding site extending down the length of the protein. Instead, the binding of hypAFP1 to ice surfaces may be derived from a unique 3D arrangement of the helices.

A modified version of this work has been published in:

Olijve, L.L.C.; Sun, T.J.; Narayanan, T.; Jud, C.; Davies, P.L.; Voets, I.K. *RSC Advances* **2013**, *3*, 5903-5908.

5.1 Introduction

The freezing point of seawater (-1.9 °C) is more than 1 °C below the equilibrium freezing point of the body fluids of fish surviving in icy polar seawaters. To protect themselves in this undercooled state from rapidly freezing upon contact with ice, these fish produce antifreeze plasma proteins that lower the freezing point by stopping the growth of endogenous ice crystals.¹ Antifreeze proteins (AFPs) have specific structural properties that enable them to adsorb to the surface of ice crystals thereby restricting the addition of water molecules to the growing ice surface. The ice surface is forced to grow with a thermodynamically unfavorable curvature, leading to a local depression of the non-equilibrium freezing point, which results in an arrest of further ice growth.² Over the years, a wide diversity of AFP structures have been found in many different organisms ranging from fish³ to insects,^{4,5} bacteria⁶ and fungi.⁷

In 2004, Marshall *et al.* reported an unusually potent type I AFP isoform in winter flounder (hypAFP1), which was 10 to 100 times more active than the previously discovered type I AFP in the same fish species.⁸ Circular dichroism (CD) measurements at 4-5 °C showed that this alanine-rich, 195 residue-long (16.7 kDa) protein is almost entirely α -helical.⁹ Analytical ultracentrifugation (AUC) analysis and gel permeation chromatography (GPC) furthermore indicated that this protein forms a dimer in solution and that it has an extreme asymmetry with an estimated axial ratio of $L/d = 19$. Based on these data, Marshall and coworkers concluded that hypAFP1 is a helical dimeric rod of 29 nm in length and 1.6 nm in diameter, consisting of two long helices associated side-by-side.¹⁰ A coiled-coil structure was ruled out based on the paucity of hydrophobic amino acid residues (e.g., Leu, Ile, Val), thereby explaining the instability of the protein ($T_{denat} \sim 9$ °C). Also, a coiled-coil structure would interfere with regularly positioned threonine residues appearing on a flat ice-binding site along the length of the protein. The complex was therefore modelled as an antiparallel dimer composed of two straight helices with relatively weak interactions between the alanine (Ala) side chains, i.e., as an Ala-zipper (Figure 1A), resulting in a closer packing with $L = 27.5$ nm and $d = 1.6$ nm giving an axial ratio of $L/d = 17$.¹¹ In this model both subunits could simultaneously engage in ice-binding (Figure 1B).

To obtain reliable evidence on the exact dimensions and multimeric state of hypAFP1, we have performed small angle X-ray scattering (SAXS) experiments on the protein in solution. SAXS is a powerful tool for characterizing the structure of macromolecules in their native environment.^{12,13} Coherent scattering of X-rays by randomly oriented proteins gives information on their size, shape and molar mass. In contrast to X-ray diffraction, SAXS does not require crystalline samples which greatly broadens its application perspective, but reduces the attainable resolution. The results presented here confirm the dimeric state of hypAFP1 and provide accurate values for its dimensions. The length of hypAFP1 as determined from the SAXS experiments is found to be smaller than hypothesized based on the previous model,¹¹ which implies that the helical dimer is arranged differently and not fully stretched out.

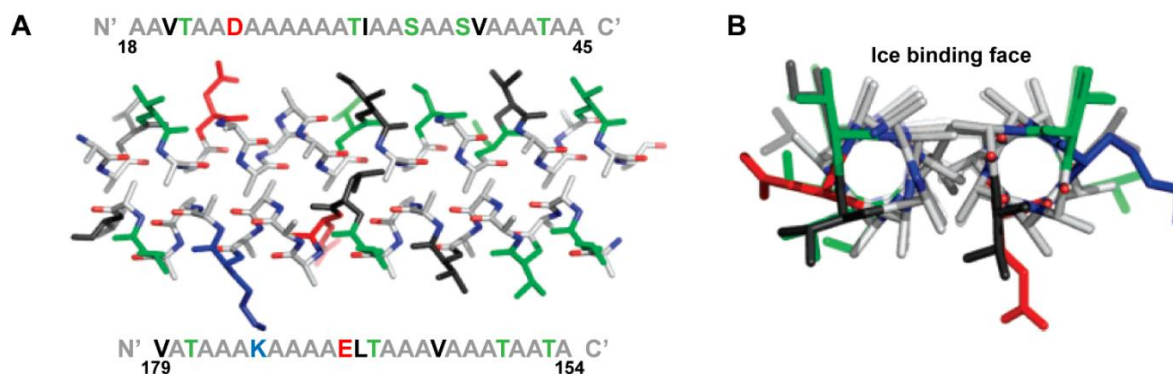


Figure 1: (A) Model of the antiparallel dimerization interface of a segment of hypAFP1 proposed by Graham *et al.*¹¹ (B) Cross-sectional end-on view of the dimer showing the interchain alanine interactions and regularly spaced threonine residues on the ice binding face.

5.2 Results

5.2.1 Guinier and form factor analysis

Figure 2A displays the small angle X-ray scattering profiles obtained at four different concentrations (2–15 mg mL⁻¹) at the high-brilliance beamline ID02 of the European Synchrotron Radiation Facility (ESRF, Grenoble, France). The accessible q -range covers the full SAXS profiles of hypAFP1, which extends from the Guinier regime at low q -values up to the form factor oscillation at high q -values with a slope of $\sim q^{-1}$ typical of cylindrical structures at intermediate q -values. A Guinier approximation (Figure 2B) was used to obtain the radius of gyration R_g and molecular weight M_w . The estimated molecular weight of $M_w = 34.7 \pm 2.5$ kDa corresponds to the formation of a dimer in solution. By using a modified Guinier approximation for a rod (Figure 2C) the cross-sectional radius R_{cs} is obtained. Using these structural parameters, the length of the protein complex was calculated using Eq. 2, confirming that hypAFP1 adopts a highly elongated structure with a length $L = 17.6 \pm 0.9$ nm and a cross-sectional radius of $R_{cs} = 1.12 \pm 0.01$ nm, giving an axial ratio of $L/d = 7.9 \pm 0.4$ (Table 2).

The experimental data are also well described by a rigid cylindrical form factor (Figure 2A and Table 3) and a worm-like chain model (data not shown). The cylindrical model assumes a rigid cylinder with uniform scattering length density. The structural parameters extracted from fitting the data with a cylindrical form factor yields a cross-sectional radius $R_{cs} = 1.26 \pm 0.02$ nm that is close to the R_{cs} obtained from the Guinier analysis, while the length $L = 19.7 \pm 0.2$ nm is slightly larger.

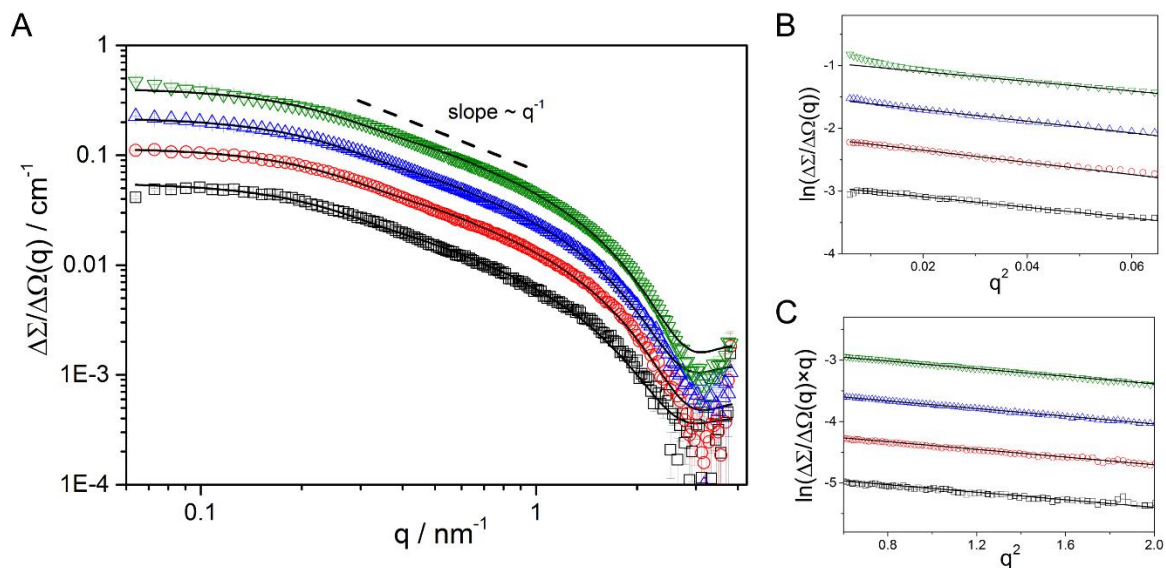


Figure 2: (A) Small angle X-ray scattering profiles of 2-15 mg mL⁻¹ hypAFP1 in 50 mM HEPES at pH 6.5 and $T = 5$ °C. The experimental data (symbols) are well described by a cylindrical form factor (solid lines). (B) Fit of the Guinier approximation of the experimental data of hypAFP1. The used q -ranges are $0.08 \leq q \leq 0.23$ nm⁻¹ (1.9 mg mL⁻¹), $0.09 \leq q \leq 0.21$ nm⁻¹ (3.8 mg mL⁻¹), $0.13 \leq q \leq 0.21$ nm⁻¹ (7.5 mg mL⁻¹) and $0.17 \leq q \leq 0.23$ nm⁻¹ (15 mg mL⁻¹). (C) Fit of a modified Guinier approximation for a rod to the experimental data. The used q -ranges are $0.65 \leq q \leq 1.49$ nm⁻¹ (1.9 mg mL⁻¹), $0.65 \leq q \leq 1.62$ nm⁻¹ (3.8 mg mL⁻¹), $0.65 \leq q \leq 1.57$ nm⁻¹ (7.5 mg mL⁻¹) and $0.73 \leq q \leq 1.50$ nm⁻¹ (15 mg mL⁻¹).

Table 1: Synchrotron data-collection and scattering-derived parameters. Structural parameters reported are from the measurements at a protein concentration of $c = 1.9 \text{ mg mL}^{-1}$. D_{max} is a model parameter in the P(r) calculation and no variance associated with D_{max} can be calculated.

Data-collection parameters	
Beamline	ID02 (ESRF, Grenoble, France)
Operating energy (keV)	12.46
Flux (photons s^{-1})	10^{12}
Wavelength (nm)	0.1
q -range (nm^{-1})	0.064-3.85
Sample-to-detector distance (m)	1.5 and 3
Total exposure time (s)	3
Concentration (mg mL^{-1})	2-15
Temperature ($^{\circ}\text{C}$)	5
Sample holder	Poly carbonate flow-through capillary, $\phi = 1.9 \text{ mm}$
Structural parameters	
I_0 (cm^{-1}) [Guinier]	0.055 ± 0.002
R_g (nm) [Guinier]	5.0 ± 0.09
I_0 (cm^{-1}) [P(r)]	0.557 ± 0.001
R_g (nm) [P(r)]	5.7 ± 0.1
D_{max} (nm)	22
Molecular mass determination	
Partial specific volume ($\text{cm}^3 \text{ g}^{-1}$)	0.7302
Contrast ($\Delta\rho \times 10^{10} \text{ cm}^{-2}$)	3.060
Molecular mass M_w from I_0 (Da)	34700 ± 1100
Calculated monomeric M_w from sequence (Da)	16685
Software employed	
Primary data reduction	SAXSutilities
Data processing	PRIMUS
<i>Ab initio</i> analysis	DAMMIF
Validation and averaging	DAMAVER
Computation of model intensities	CRYSOL
Rigid-body modelling	SASREF
Graphical representation	PyMol and SITUS

Table 2: Structural parameters obtained from a (modified) Guinier analysis. R_g and M_w are obtained using a Guinier approximation (Figure 2B), R_{cs} by using a modified Guinier approximation for a rod (Figure 2C) and L was calculated using Eq. 2.

C (mg/mL)	R_g (nm)	R_{cs} (nm)	L (nm)	L/d	M_w (kDa)
1.9	5.0	1.11	17.3	7.8	34.7
3.8	5.4	1.12	18.5	8.2	37.3
7.5	5.3	1.12	18.1	8.1	35.4
15	4.8	1.11	16.4	7.4	31.4
average	5.1 ± 0.3	1.12 ± 0.01	17.6 ± 0.9	7.9 ± 0.4	34.7 ± 2.5

Table 3: Structural parameters obtained after fitting the SAXS data with a cylindrical form factor. The radius of gyration is calculated from the obtained R_{cs} and L using Eq. 2.

C (mg/mL)	R_g (nm)	R_{cs} (nm)	L (nm)	L/d	χ^2
1.9	5.8	1.28	19.9	7.7	0.98
3.8	5.7	1.23	19.5	7.9	0.85
7.5	5.8	1.26	19.8	7.9	0.98
15	5.7	1.25	19.6	7.8	0.92
average	5.8 ± 0.1	1.26 ± 0.02	19.7 ± 0.2	7.8 ± 0.1	0.93 ± 0.06

5.2.2 Structural model of the protein complex

From the results of the Guinier and form factor analyses it is evident that hypAFP1 has a highly extended shape with a length of $L = 19 \pm 2$ nm and diameter of $d = 2.3 \pm 0.2$ nm. These dimensions imply that hypAFP1 cannot form a dimer of two fully extended helices, since the latter would correspond to a length of ~ 27.5 nm. To derive information on the shape of the dimer, we have reconstructed the *ab initio* shape of the protein from simulated annealing calculations using DAMMIF, which features an unlimited and adapting search volume that avoids boundary effects, especially in highly elongated objects.¹⁴ The averaged and filtered volumetric map of hypAFP1 shows a rod-like shape with a length of 18.5 nm (Figure 3D, cyan color), resembling the dimensions found in the Guinier and form factor analysis. Given the dimensions and high helical contact of hypAFP1, it is evident that the molecular structure of this hyperactive antifreeze protein is unlike any antifreeze protein found so far. The β -helical folds of hyperactive AFPs from insects display a flat β -sheet ice-binding surface with regularly positioned threonine residues.⁴ Hence, a likely arrangement of the dimer would be two helices associated side-by-side, enabling an uniform presentation of threonine residues along the length of the protein (Figure 1).¹¹ Yet, this structure is not consistent with the SAXS results, which means that a different conformation of the helices might confer the hyperactive antifreeze activity.

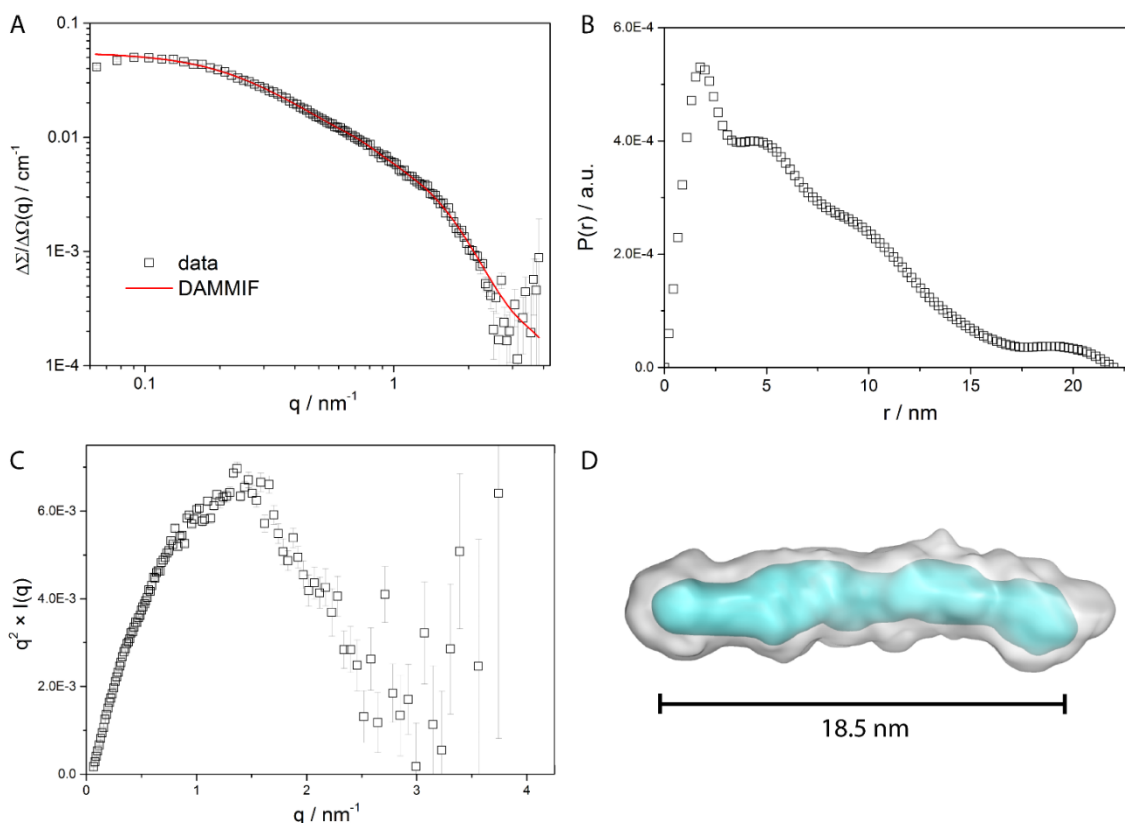


Figure 3: (A) Fit of simulated annealing with DAMMIF, (B) radial distribution function (RDF) obtained after inverse Fourier transformation of the experimental data, (C) Kratky plot showing a parabolic shape indicative of a folded state of the protein,¹⁵ and (D) 10 calculations with DAMMIF were performed to produce the average and filtered volumetric map of hypAFP1, showing a rod-like shape with a length of 18.5 nm (final $\chi^2 = 2.57$).

5.2.3 Rigid body modeling

To get more insight into the 3D arrangement of the helices in the protein complex of hypAFP1, we have performed rigid body modeling using SASREF.¹⁶ SASREF uses multiple rigid subunits with known atomic coordinates to perform quaternary structure modeling of a protein complex against the experimental data. Since no crystallographic data of the subdomains in the protein complex of hypAFP1 is available, we have constructed two long α -helices with a length of 18.5 nm and two short helices to account for the remaining number of residues of the protein complex. These subunits with provided contact conditions (Figure 4A) were provided as input for SASREF. The result of the rigid body modeling (Figure 4C) seems consistent with the results of the more coarse-grained modeling approach and comes very close to the hypothesized structure in which the protein complex is able to display regularly positioned threonine residues on its ice-binding face, enabling a large protein surface area to engage in ice-binding which could explain the hyperactive nature. However, we need to draw attention to the limitations of the resulting structural model. Firstly, the initial contact conditions influence the SASREF

results. Therefore, about six contact conditions per complex were set and various contact conditions were tested. Reducing the number of contact conditions resulted in one of the subunits losing contact with the complex. Secondly, we propose the structural model in Figure 4C on the basis of additional information rather than the goodness of fit of the different SASREF models. Hence, the validity of the model needs to be tested with additional biochemical experiments.

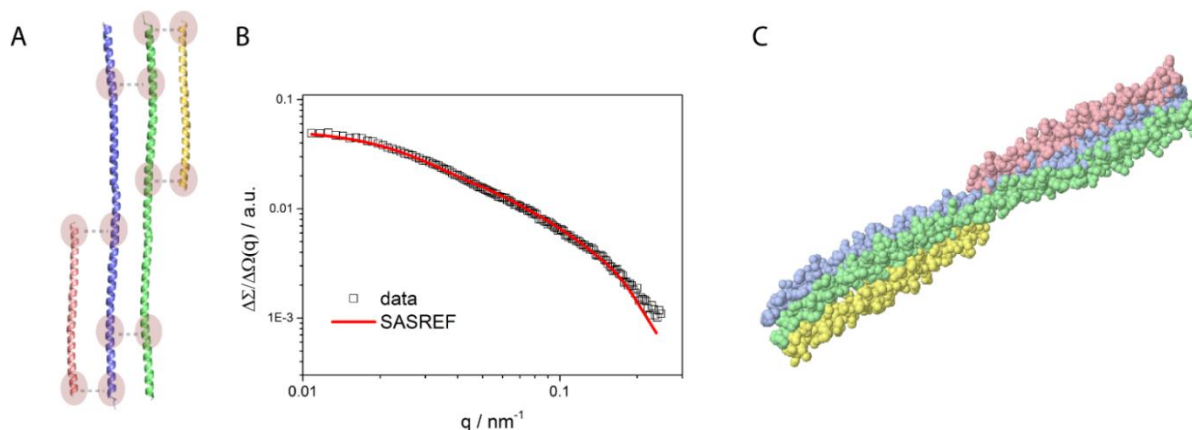


Figure 4: (A) Subdomains with provided contact conditions used for the rigid body modeling. The subdomains were constructed from the PDB entry 3VEM. (B) Fit of the model to the experimental data (final $\chi^2 = 3.79$), using P1 symmetry. Data range used for the rigid body modeling was cut-off from the first real point of the Guinier regime up to $q = 0.25 \text{ nm}^{-1}$. (C) Resulting structural model from the rigid body modeling.

5.3 Discussion

Shortly after the reported SAXS experiments on hypAFP1, Sun *et al.* resolved its crystal structure consisting of a dimeric, four-helix bundle (Figure 5A).¹⁷ Both 290 Å long helices fold exactly in the middle with an angle of 180° such that their N' and C' termini are aligned side-by-side. The two hairpin helices are aligned in an antiparallel manner with a distinct capping structure. Interestingly, the four-helix bundle contains an alanine-rich hydrophobic core that retains ~ 400 waters. These interior waters are coordinated by the bundles into two intersecting polypentagonal networks (Figure 5B), extending outwards to the protein surface. The ordered waters are hypothesized to be involved in the ice-binding function of the protein.

The four-helix bundle in the crystal structure of hypAFP1 has a length of $L = 14.5 \text{ nm}$, while analysis of the SAXS data yields a length of $L = 18.5 \text{ nm}$. We propose tentatively that this difference is due to the presence of a very small fraction of aggregated proteins. HypAFP1 irreversibly denatures above 10 °C, and is only stable below that temperature for approximately two weeks. During the SAXS measurements the sample was carefully prepared, the temperature strictly controlled and the measurements thoroughly checked for radiation damage. However, even a small amount of denaturation or radiation damage might have caused

irreversible aggregation leading to an increase in forward scattering intensity, and ultimately a higher value for the estimated length. A comparison between the theoretical scattering curve of hypAFP1 and the experimental data supports this line of thought (Figure 6A).¹⁸ The CRY SOL fit describes the data well in the high q -regime, but deviates in the low q -regime, which leads to χ^2 values > 5 . Superimposing the crystal structure to the low resolution model (Figure 6B) also shows that the volume of the model is larger than the volume occupied by the crystal structure due to the small overestimation in length due to the probable presence of a very small fraction of aggregates.

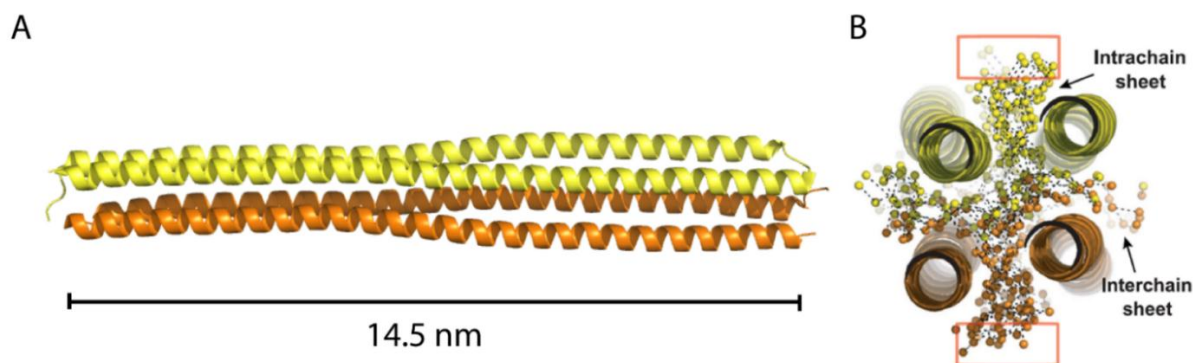


Figure 5: (A) Crystal structure of hypAFP1 showing a four-helix bundle. (B) Interior water network inside the four-helix bundle.¹⁷

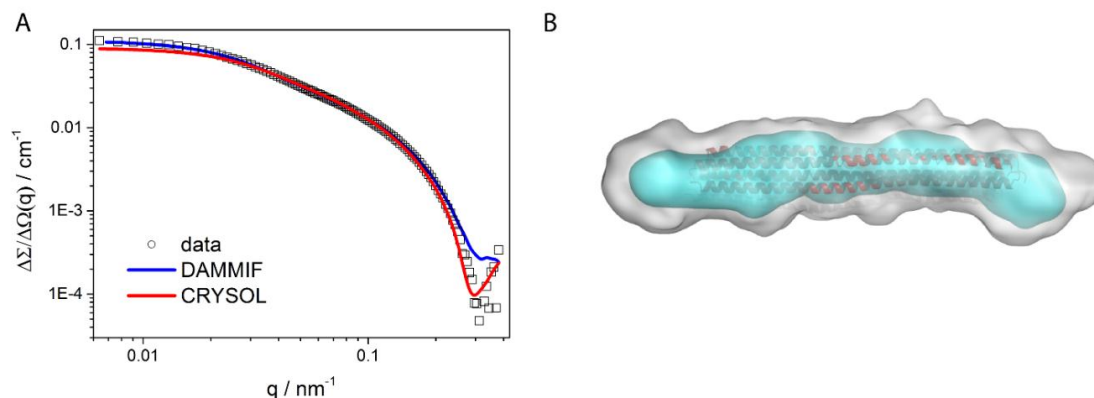


Figure 6: (A) Fit of CRY SOL (calculated theoretical scattering curve from the known atomic coordinates of the crystal structure) and DAMMIF (volumetric model) to the experimental data, (B) crystal structure (PDB: 4KE2) superimposed to the average of 10 independent DAMMIF models (grey) and filtered most probable volume (cyan).

5.4 Conclusion

Structural data form the basis for understanding the hyperactive nature of hypAFP1. Our SAXS experiments provided the first reliable and independent estimation of the length, diameter and molecular weight of hypAFP1 in solution. We found that hypAFP1 has a rigid cylindrical shape with a length and diameter of $L = 19 \pm 2$ nm and $d = 2.3 \pm 0.2$ nm. This demonstrates unequivocally that the two α -helices in the dimer are not fully extended (i.e., $L = 27.5$ nm), contrary to what was hypothesized previously, irrespective of whether they are arranged in a coiled-coil or parallel conformation. Furthermore, if the helical dimers would be held together via an interaction of the alanine side chains, the packing would be too close to match the experimentally observed diameter suggesting that hypAFP1 adopts a more complex conformation. Shortly after publication of these SAXS experiments, Sun *et al.* resolved the crystal structure of hypAFP1.¹⁷ This confirmed that hypAFP1 did not adopt a fully extended conformation. Instead, hypAFP1 arranges into a four-helix bundle containing a complex interior water network.

5.5 Materials and methods

Sample preparation

Recombinant hypAFP1 was produced as previously described¹⁹ with the following modification. Instead of ice affinity purification, three rounds of ammonium sulfate precipitation were used. This is an effective method for purification because hypAFP1 precipitates from solution at a relatively low percent saturation of ammonium sulfate (28 %) while most *Escherichia coli* proteins remain soluble. The hypAFP1 pellet from the last precipitation was re-suspended and dialyzed overnight in 50 mM HEPES buffer (pH 6.5) to remove ammonium sulfate. Purity was estimated by SDS-PAGE, and the protein concentration was measured by amino acid analysis. Recombinant hypAFP1 at 15 mg mL⁻¹ was stored at 4 °C and used within 2-3 weeks of its preparation.

Data acquisition and data reduction

The synchrotron radiation X-ray scattering data were collected at the high-brilliance beamline ID02 of the ESRF (Grenoble, France)²⁰ operating at 12.46 keV. The scattering intensity was measured as a function of momentum transfer vector $q = \frac{4\pi}{\lambda} \sin \theta$, where $\lambda = 0.1$ nm is the radiation wavelength and 2θ is the scattering angle. Two sample-to-detector distances of 1.5 and 3 m were used to cover an angular range of $0.064 < q < 3.85$ nm⁻¹. Samples were measured in a polycarbonate (ENKI, KI-Beam) flow-through capillary with a diameter of $d = 1.9$ mm kept in a temperature-controlled holder at $T = 5$ °C. The two-dimensional SAXS patterns were normalized to an absolute intensity scale using the calibrated detector response function, known sample-detector distance, and measured incident and transmitted beam intensities.²⁰ These normalized SAXS patterns were subsequently azimuthally averaged to obtain the one dimensional SAXS profiles. For each sample, 10 frames of 0.3 s were collected and averaged after checking for radiation damage. This corresponds to a total data collection time of 3 s per sample with a reduced flux of about 10¹² ph/s. To obtain the protein scattering curve, the normalized background scattering profile of the buffer and polycarbonate cell was subtracted from the normalized sample scattering profiles. Finally, the absolute calibration of the scattering curves were verified using the known scattering cross-section per unit sample volume, $\Delta\Sigma/\Delta\Omega$, of water, being $\Delta\Sigma/\Delta\Omega(0) = 0.01665$ cm⁻¹ for $T = 5$ °C.^{21,22}

Data analysis

Small angle X-ray scattering is a powerful tool to determine the dimensions and molar mass of proteins and protein complexes directly in solution. The primary requirement is an accurate measurement of the q -dependence of the scattering intensity of the sample of interest, the buffer, and a calibration standard with known scattering cross-section such as water²¹ to compute the differential scattering cross-section per unit sample volume, $\Delta\Sigma/\Delta\Omega$. This quantity

gives direct access to the size, shape, and average molar mass of the protein (complex) under investigation according to

$$(1) \frac{\Delta\Sigma}{\Delta\Omega} = KcM_wS(q)P(q)$$

with the difference in scattering contrast with the solvent, K , the concentration, c , the molecular weight, M_w , and interference effects arising from the structure within the sample, i.e., interparticle and intraparticle interference represented by the structure factor, $S(q)$, and the form factor, $P(q)$. First, the scattering data were analyzed using a Guinier approximation to extract the radius of gyration, R_g , and the forward scattering intensity, I_0 , which is $\Delta\Sigma/\Delta\Omega(q \rightarrow 0)$. For monodisperse globular proteins, the Guinier approximation is valid for $qR_g \leq 1.3$ and R_g and I_0 were determined from the slope and y-intercept of the Guinier plot $\ln(\Delta\Sigma/\Delta\Omega(q))$ vs. q^2 using PRIMUS from the ATSAS software package.²³ For a rod-like particle, a modified Guinier approximation can be used in the q -range where $\Delta\Sigma/\Delta\Omega(q) \propto q^{-\alpha}$ with $\alpha \sim 1$ to extract the cross-sectional radius of the cylinder from the determined cross-sectional radius of gyration, with $R_{cs} = \sqrt{2}R_{gcs}$.

Using the obtained radius of gyration and the cross-sectional radius from the Guinier approximation, the length of a cylinder can be calculated by

$$(2) R_g^2 = \frac{R_{cs}^2}{2} + \frac{L^2}{12}$$

Subsequently, $I_0 = \Delta\Sigma/\Delta\Omega(q \rightarrow 0)$ was used to calculate the molar mass of the protein (complex), according to

$$(3) M_{saxs} = I_0 \frac{N_{av}}{c(\Delta\rho\bar{v})^2}$$

with the molecular weight M_{SAXS} in g mol^{-1} , the forward scattering intensity I_0 in cm^{-1} , concentration c in g cm^{-3} , Avogadro's number N_{av} , the scattering length density difference $\Delta\rho$ in cm^{-2} ($\rho_{\text{protein}} - \rho_{\text{H}_2\text{O}}$, where $\rho_{\text{protein}} = 1.25 \times 10^{-5} \text{ cm}^{-2}$ and $\rho_{\text{H}_2\text{O}} = 9.44 \times 10^{-6} \text{ cm}^{-2}$)²⁴ and the partial specific volume of the protein in solution $\bar{v} = 0.7302$ in $\text{cm}^3 \text{ g}^{-1}$ calculated using SEDNTERP.²⁵ Finally, we have analyzed the scattering profiles in the entire recorded q -range with various form factor models using the software package SASfit²⁶ assuming that hypAFP1 was measured in ideal dilute solution where interparticle interactions can be neglected (i.e., $S(q) = 1$). Two form factors were used; one describing a cylindrical object²⁷ and the other describing a worm-like chain model according to the equations reported by Pedersen *et al.*²⁸

Molecular shape reconstruction

In order to derive information on the solution structure of the protein, the molecular shape was reconstructed using simulated annealing methods. First, the radial distribution function (RDF), $P(r)$, which describes the probable frequency of interatomic vector lengths (r) within the scattering particle, was obtained upon indirect inverse Fourier transformation of the scattering data using GNOM.¹⁴ The maximum linear dimension (D_{max}) was set to approximately $3 \times R_g$ and adjusted to give the best fit to the experimental data. The RDF was considered to be zero at $r = 0 \text{ \AA}$ and approaching zero at D_{max} . The GNOM output files were used as input for simulated annealing calculations over the range $0.08 < q < 3.8 \text{ nm}^{-1}$ using the online version of DAMMIF.²⁹ For each scattering curve, 10 independent bead models were generated without predefined shape or symmetry. The 10 different models were superimposed using DAMSEL and DAMSUP. Next, DAMAVER was used to average the aligned models and compute the probability map.³⁰ Finally, DAMFILT was used to filter the averaged model to give a structure that has high densities on the probability map.

5.6 References

1. DeVries, A.L.; Wohlschlag, D.E. *Science* **1969**, *163*, 1073-1075.
2. Raymond, J.A.; DeVries, A.L. *Proc. Natl. Acad. Sci. USA*. **1977**, *74*, 2589-2593.
3. Fletcher, G.L.; Hew, C.L.; Davies, P.L. *Annu. Rev. Physiol.* **2001**, *63*, 359-390.
4. Pentelute, B.L.; Gates, Z.P.; Tereshko, V.; Dashnau, J.L.; Vanderkooi, J.M.; Kossiakoff, A.A.; Kent S.B. *J. Am. Chem. Soc.* **2008**, *130*, 9695-9701
5. Greather, S.P.; Kuipers, M.J.; Gagné, S.M.; Walker, V.K.; Jia, Z.; Sykes, B.D.; Davies, P.L. *Nature* **2000**, *406*, 325-328.
6. Garnham, C.P.; Campbell, R.L.; Davies, P.L. *Proc. Natl. Acad. Sci. USA*. **2011**, *108*, 7363-7367.
7. Lee, J.H.; Park, A.K.; Do, H.; Park, K.S.; Moh, S.H.; Chi, Y.M.; Kim, H.J. *J. Biol. Chem.* **2012**, *287*, 11460-11468.
8. Marshall, C.B.; Fletcher, G.L.; Davies, P.L. *Nature* **2004**, *429*, 153.
9. Gauthier, S.Y.; Marshall, C.B.; Fletcher, G.L.; Davies, P.L. *FEBS* **2005**, *272*, 4439-4449.
10. Marshall, C.B.; Chakrabartty, A.; Davies, P.L. *J. Biol. Chem.* **2005**, *280*, 17920-17929.
11. Graham, L.A.; Marshall, C.B.; Lin, F.H.; Campbell, R.L.; Davies, P.L. *Biochemistry* **2008**, *47*, 2051-2063.
12. Svergun, D.I.; Koch, M.H.J. *Rep. Prog. Phys.* **2003**, *66*, 1735-1782
13. Putnam, C.D.; Hammel, M.; Hura, G.L.; Tainer, J.A. *Q. Rev. Biophys.* **2007**, *40*, 191-285.
14. Svergun, D.I. *J. Appl. Cryst.* **1992**, *25*, 495-503.
15. Jacques, D.A.; Guss, J.M.; Svergun, D.I.; Trehwella, J. *Acta Cryst.* **2012**, *D68*, 620-626.
16. Petoukhov, M.V.; Svergun, D.I. *Biophys. J.* **2005**, *89*, 1237-1250.
17. Sun, T.; Lin, F.H.; Campbell, R.L.; Allingham, J.S.; Davies, P.L. *Science* **2014**, *343*, 795-798.
18. Svergun, D.I.; Barberato, C.; Koch, M.H.J. *J. Appl. Cryst.* **1995**, *28*, 768-773.
19. Lin, F.H.; Sun, T.; Fletcher, G.L.; Davies, P.L. *Protein Expr. Purif.* **2012**, *82*, 75-82.
20. Sztucki, M.; Di Cola, E.; Narayanan, T. *J. Appl. Cryst.* **2010**, *43*, 1479-1487.
21. Glatter, O.; Kratky, O. eds. *Small-angle X-ray Scattering*. Academic Press, London, **1982**.
22. Mylonas, E.; Svergun, D.I. *J. Appl. Cryst.* **2007**, *40*, s245-s249
23. Konarev, P.V.; Volkov, V.V.; Sokolova, A.V.; Koch, M.H.J.; Svergun, D.I. *J. Appl. Cryst.* **2003**, *36*, 1277-1282.
24. Online scattering length density calculator of NIST
<http://www.ncnr.nist.gov/resources/sldcalc.html>
25. Jacques, D.A.; Trehwella, J. *Protein Sci.* **2010**, *19*, 642-657.

26. SASfit software package for fitting small angle scattering curves
<http://kur.web.psi.ch/sans1/SANSSoft/sasfit.html>
27. Lindner, P.; Zemb, T. eds. *Neutron, X-rays and light: scattering methods applied to soft condensed matter*, Elsevier, Amsterdam, **2002**.
28. Pedersen, J.S.; Schurtenberger, P. *Macromolecules* **1996**, *29*, 7602-7612.
29. Franke, D.; Svergun, D.I. *J. Appl. Cryst.* **2009**, *42*, 342-346.
30. Volkov, V.V.; Svergun, D.I. *J. Appl. Cryst.* **2003**, *26*, 860-864.

Chapter 6

A calcium-induced conformational change of an ice-anchoring protein domain studied using small angle X-ray scattering

Abstract

Protein structure is directly related to protein function. Hence, information on the solution structure of a protein in addition to biochemical and crystallographic data allows to understand the functional role of proteins. Small angle X-ray scattering (SAXS) is a powerful tool to determine the size, shape and other structural properties of (biological) macromolecules in solution and in various buffer conditions. In this chapter, the influence of calcium binding on the solution structure of a tetrameric tandem model protein (tetraRII) is studied. The SAXS data clearly show a rigidification of the structure of tetraRII, which cannot be measured directly in biochemical experiments. This information provides insight into the role of the RII domain in anchoring of an Antarctic bacterium to ice.

Part of this work has been published in:

Vance, T.D.; Olijve, L.L.C.; Campbell, R.L.; Voets, I.K.; Davies, P.L.; Guo, S. *Biosci. Rep.* **2014**, *34*, 357-368.

6.1 Introduction

The Antarctic bacterium *Marinomonas primoryensis* produces a 1.5 MDa ice adhesion membrane protein which enables it to reach the upper layers of Antarctic lake water where oxygen and nutrients are more abundant.^{1,2} The large size of this protein is mainly due to the highly repetitive RII region of the protein, which contains approximately 120 tandem repeats of an identical 104-residue domain. The small RIV end-region of the protein is the only ice binding part of the protein, but both domains have a fully folded structure only in the presence of calcium ions.^{3,4} To resolve the role of calcium binding on the structure of the RII region of the ice anchoring protein, a protein with four tandem repeats of RII (tetraRII) was constructed.⁵ Circular dichroism (CD) analysis showed that calcium binding induces the formation of secondary structure (β -sheets) in the tetraRII protein (Figure 1). In this study, small angle X-ray scattering (SAXS) is used to study calcium induced conformational changes in the tertiary structure of tetraRII directly in solution. The results show that tetraRII rigidifies significantly upon calcium binding. The crystal structure, only resolved in the presence of calcium, shows an excellent fit to the experimental SAXS data of calcium-bound tetraRII.

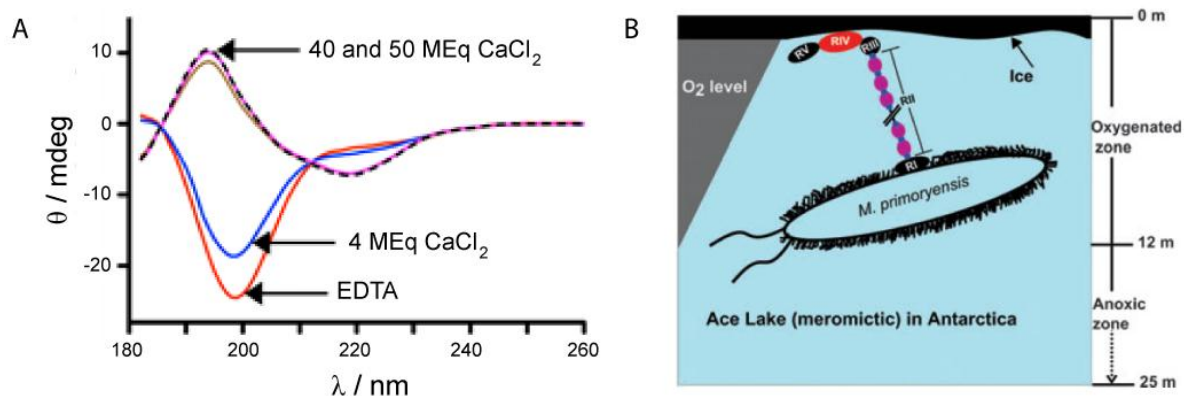


Figure 1: (A) Circular dichroism spectra of tetraRII showing a calcium induced conformation change and the formation of β -sheets. (B) Hypothesized function of the RII domain in the ice-anchoring of *M. primoryensis* bacteria to reach oxygen rich ice-water levels (not drawn to scale).

6.2 Results

6.2.1 Validation of crystal structure

SAXS measurements were performed on solutions of tetraRII in buffer with either 20 mM CaCl_2 or 0.5 mM EDTA. The experimental scattering profile of tetraRII in the presence of calcium is shown in Figure 2A. The scattering profile ranges from the Guinier regime at low q -values up to the first form factor oscillation at high q -values. Three power-law regimes are apparent: a Guinier plateau occurs at low q -values; at intermediate q -values the intensity falls off with q^{-1} , which is typical for rigid 1D objects; and finally at high q -values the Porod regime holds where $I \propto q^{-4}$.

To verify from the SAXS data that the protein in the presence of calcium is in non-aggregated form, the XRD data is compared to the solution scattering data using CRY SOL, yielding an excellent fit over the whole q -range (Figure 2A). Furthermore, a low-resolution model was constructed from the experimental SAXS data using the *ab initio* modeling program DAMMIN.⁶ DAMMIN uses an enclosed search volume of densely packed dummy atoms to reconstruct the shape of the protein in solution. Ten independent models were calculated and all provided a good fit to the experimental data (Figure 2A). The ten models were averaged using DAMAVER and no models in the set were rejected.⁷ The resulting molecular shape of the *ab initio* model shows a good overlay with the crystal structure of tetraRII (Figure 3), corroborating that the crystal structure is representative of the structure of the protein in solution.⁸

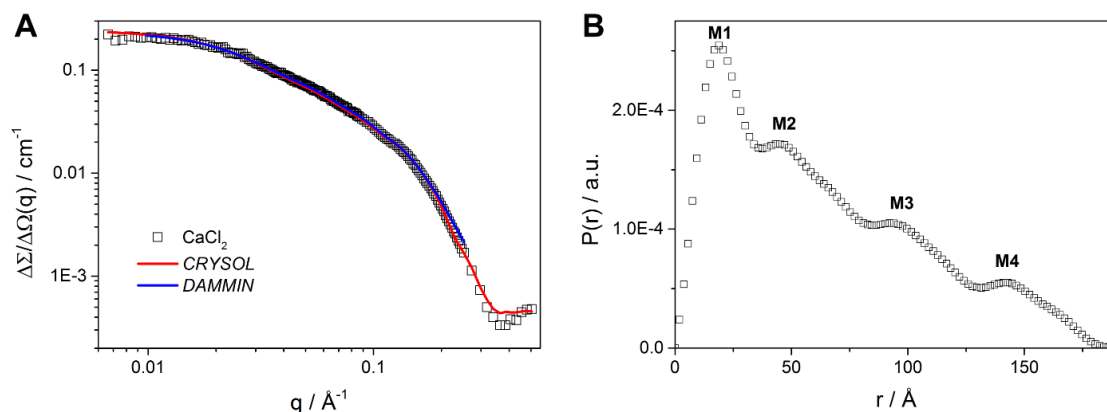


Figure 2: Fit of low-resolution model and crystal structure of tetraRII in the presence of calcium to experimental SAXS data (A) Experimental scattering data of tetraRII measured in 20 mM Tris–HCl pH 9, 100 mM NaCl and 20 mM CaCl_2 (symbols), fit result of *ab initio* modeling (DAMMIN, blue line) and theoretical scattering curve calculated from the known atomic coordinates of the crystal structure of tetraRII using CRY SOL (red line).⁸ (B) Radial distribution function (RDF) obtained after IFT analysis of the scattering data, using data points starting from the first Guinier point until the Porod regime ($0.009 < q < 0.26 \text{\AA}^{-1}$). Four maxima (M1–4) can be observed, which correspond to the center of each domain of the tetraRII.

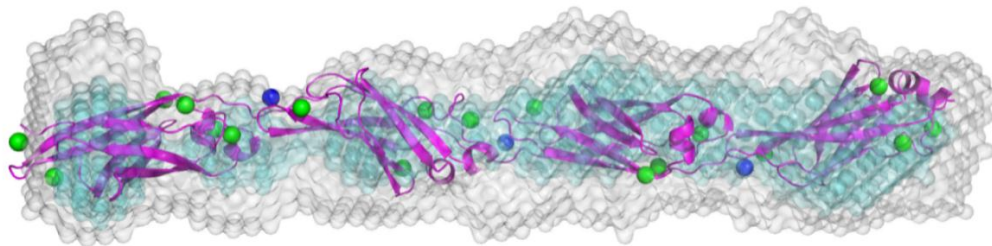


Figure 3: Aligned low-resolution dummy-atom model and crystal structure of tetraRII in the presence of calcium. The averaged ab initio shape calculated from ten models (grey) represents the total volume occupied by the spread of all models (final goodness of fit, $R_f = 0.00084$), with the filtered and most-populated volume represented in cyan and the crystal structure of tetraRII in magenta. Ca^{2+} ions are represented as spheres, with in blue the inter-domain calcium ions.

6.2.2 Impact of calcium binding

To evaluate the impact of Ca^{2+} on the rigidity of tetraRII in solution, the protein was also measured in buffer containing the calcium chelator EDTA (0.5 mM). The $I \propto q^{-1}$ power-law regime is much shorter in the presence of EDTA (Figure 4A) and is preceded by a short power-law regime with a scaling exponent $-1 \leq \alpha \leq -2$ indicating a considerable reduction in stiffness upon the addition of EDTA. In Figure 4B, the data are visualized in a Holtzer-Cassasa plot of $q \times \Delta\Sigma/\Delta\Omega(q)$ versus q to highlight these differences between the samples with EDTA and Ca^{2+} in the intermediate q -regime. The Holtzer-Cassasa representation clearly reveals the Ca^{2+} -induced rigidification of tetraRII as evidenced by the differences in the length of the Holtzer plateau in the intermediate q -regime. In line with the CD data (Figure 4A), it is evident from the SAXS profiles that tetraRII undergoes a significant change in fold upon calcium binding.

Next, the experimental data was analyzed using a form factor originally developed for semi-flexible, self-avoiding polymer chains, which is the WLC model as reported by Schurtenberger and Pedersen.⁹ This WLC model describes the conformation of an intrinsically flexible cylinder built up from N rigid segments with a related Kuhn length L_k , which is equal to twice the so-called persistence length, L_p . The contour length L_c is then given by the number of locally stiff segments N multiplied by their length L_p . The structural parameters obtained from the form factor analysis are given in Table 1. For tetraRII we may compare these to the dimensions computed from the crystal structure obtained by XRD (X-ray diffraction) that show the protein is a rod-like object with a length $L \sim 190 \text{ \AA}$ composed of four rigid subunits of approximately $23 \times 28 \text{ \AA}$ in cross-section and 45 \AA long. We find a good agreement between the XRD and SAXS data for tetraRII in the presence of calcium: application of the WLC model gives $L_c \sim 176 \text{ \AA}$, a cross-sectional radius $R_{cs} \sim 11 \text{ \AA}$ and persistence length $L_p \sim 95 \text{ \AA}$. Here, L_p is larger than the size of one subunit suggesting the formation of a rigid protein complex. Similar to the results obtained from size-exclusion chromatography experiments, tetraRII

appears larger and less rigid in the presence of EDTA as observed from the increase in contour length $L_c \sim 199 \text{ \AA}$ and decrease in persistence length $L_p \sim 41 \text{ \AA}$. The persistence length in the presence of EDTA is comparable with the length of one subunit ($\sim 45 \text{ \AA}$), suggesting that the protein loses its rigidity if no calcium is complexed to the structure.

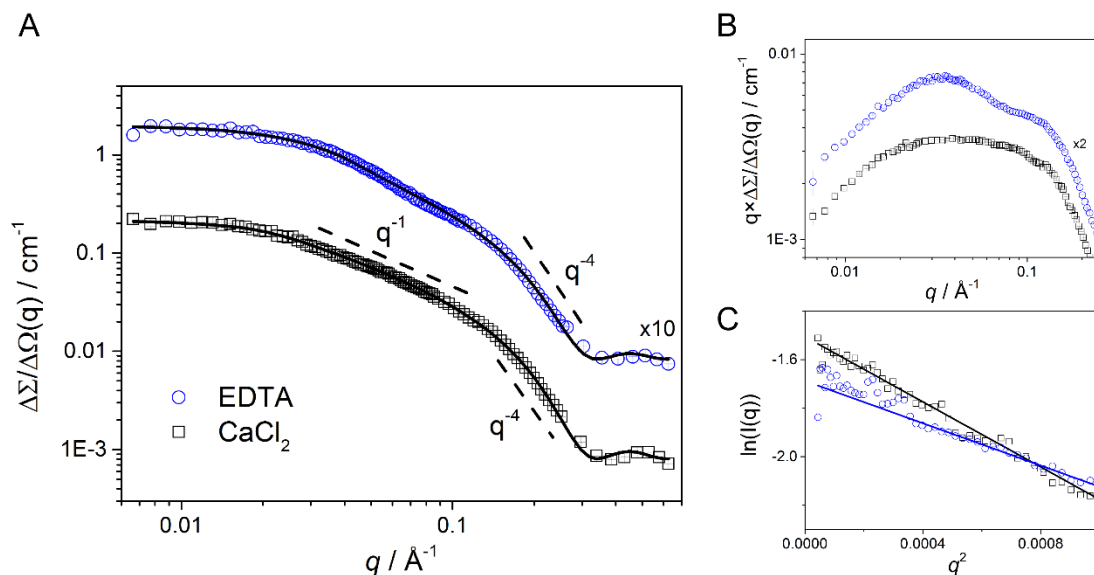


Figure 4: SAXS profiles of tetraRII in presence and absence of calcium, with (A) experimental SAXS data (symbols) and fits with the Schurtenberger–Pedersen form factor for worm-like, self-avoiding chains (solid lines). Dashed lines are drawn to indicate the slope of the scattering curves in the intermediate and high q -regime. The solution structure of tetraRII (squares, circles) was investigated in two buffers composed of (**CaCl₂**) 20 mM Tris–HCl pH 9, 100 mM NaCl and 20 mM CaCl_2 and (**EDTA**) 20 mM Tris–HCl pH 9, 100 mM NaCl and 0.5 mM EDTA, respectively. (B) Holtzer–Cassasa representation ($q \times \Delta\Sigma/\Delta\Omega(q)$ versus q) clarifying the change in shape of the scattering curve evident from the difference in length of the Holtzer plateau at intermediate q -regime in 0.5 mM EDTA (circles) or 20 mM CaCl_2 . (C) Guinier representation of the data (symbols) and Guinier fits (lines).

Table 1: Structural parameters obtained from fitting the experimental data of tetraRII with a form factor describing a WLC with excluded volume interactions with a circular cross-section of uniform scattering length density given by Schurtenberger and Pedersen L_c = contour length, L_p = persistence length, R_{cs} = cross-sectional radius of cylinder.¹³

	L_c (Å)	L_p (Å)	R_{cs} (Å)
CaCl₂	175.9 ± 1.8	96.3 ± 2.3	11.2 ± 0.1
EDTA	198.9 ± 0.2	41.2 ± 0.1	11.2 ± 0.1

Table 2: Parameters obtained from the Guinier analysis. C = concentration, $M_{w,calc}$ = theoretical molecular weight calculated from the amino acid sequence, I_0 = forward scattering intensity extrapolated to zero angle, R_g = radius of gyration, $M_{w,saxs}$ = estimated molecular weight determined by SAXS.

	C (mg/mL)	$M_{w,calc}$ (kDa)	I_0 (cm ⁻¹)	R_g (Å)	$M_{w,SAXS}$ (kDa)
CaCl₂	5	42.6	0.222 ± 0.001	44.9 ± 0.5	52.6
EDTA	5	42.6	0.185 ± 0.003	36.2 ± 0.1	43.9

6.3 Discussion

Circular dichroism data from previous work showed the influence of calcium binding on the secondary structure of tetraRII (Figure 1). At 20 molar equivalents the protein shows a β -sheet-like spectrum. The role of calcium on the overall protein and its influence on the rigidity of the structure is difficult to study with biochemical experiments and/or crystallography, however small angle X-ray scattering enables the determination of the structural properties of the protein in solution. The SAXS measurements clearly show a difference in the fold of tetraRII in buffer with calcium or EDTA, which is best observed by presenting the data in a Holtzer-Cassasa plot of $q \times \Delta\Sigma/\Delta\Omega(q)$ versus q to highlight the power law regime where $I \propto q^{-1}$. The formation of the $I \propto q^{-1}$ regime is an indication of the formation of an extended, cylinder-like structure in the presence of calcium. Also, a form factor analysis using a worm-like chain model showed an increase in persistence length (i.e., stiffness) of tetraRII in the presence of calcium. Furthermore, since the crystal structure of tetraRII in the presence of calcium has been determined, the known atomic coordinates of the crystal structure can be used to calculate a theoretical scattering curve, which can be superimposed to the experimental scattering data (CRYSOL). The CRYSOL fit is in good agreement with the experimental data and likewise, the crystal structure nicely matches the low resolution model of the solution structure of tetraRII.

These findings suggest that the calcium rigidified linker regions could act to increase the distance between the ice-adhesive RIV domain and bacterial cell surface (Figure 1), with a maximum length of 0.6 μm for the RII domain when fully extended. High extension is necessary to protrude away from the densely covered cell surface and enable efficient

interaction with ice.¹ Calcium is normally present in sub-micromolar concentrations in the bacterial cytosol, while the brackish-water of the Ace Lake has high salinity and calcium concentrations in the low millimolar range (3-7 mM).⁵ The RII domain of *MpAFP* needs roughly 10 molar equivalents of calcium to be fully structured. Therefore, *MpAFP* could be secreted as a large unfolded chain, and only fold upon entering the extracellular brackish ice-water. The extension of the extremely large ice-anchoring membrane proteins enables the strictly aerobic bacteria to localize efficiently near the water surface where there is more oxygen and nutrients.

6.4 Conclusion

The SAXS experiments in this study showed that tetraRII in the presence of calcium is in the non-aggregated form. Evaluation of the XRD data with the solution scattering data yields an excellent fit over the whole q -range, verifying that the crystal structure is the representative structure in solution. The influence of calcium on the tertiary structure of tetraRII is further studied by comparing the structural parameters of tetraRII in the presence of calcium and calcium chelator (EDTA). Form analysis of the scattering data clearly demonstrates a rigidification of the protein structure in the presence of calcium. Calcium induced rigidification of the linker regions of the RII protein enable *M. primoryensis* to protrude ice adhesion proteins away from the cell surface and localize in oxygen- and nutrient-rich water layers. As demonstrated in this chapter, in combination with biochemical and crystallographic data, small angle X-ray scattering can be a valuable tool in understanding ligand induced conformational changes in protein structures, and give more insight in the functional role of the protein structure.

6.5 Material and methods

SAXS data acquisition and reduction

SAXS data were collected on a Ganesha lab instrument (SAXSLAB) equipped with a GeniX-Cu ultra-low divergence source producing X-ray photons with a wavelength of 1.54 Å and a flux of 10^8 ph/s. The scattering intensity was measured as a function of momentum transfer vector $q = \frac{4\pi}{\lambda} \sin \theta$, where λ is the radiation wavelength and 2θ is the scattering angle. Three sample-to-detector distances of 113, 713 and 1513 mm were used to cover an angular range of $0.006 < q < 2.41 \text{ \AA}^{-1}$. Samples were measured in polycarbonate (ENKI, KI-Beam) capillaries with a diameter of $d = 2$ mm kept in a temperature controlled holder at $T = 20$ °C. The 2D scattering data were recorded on a Pilatus 300 K silicon pixel detector with 487×619 pixels of 172 \mu m^2 . The beam center and q -range were calibrated using a silver behenate standard. Two-dimensional SAXS patterns were brought to absolute intensity scale using the calibrated detector response function, known sample-to-detector distances, and measured incident and transmitted beam intensities. These normalized SAXS patterns were subsequently azimuthally averaged to obtain the 1D SAXS profiles. Data were collected at protein concentrations of 5 and 20 mg ml⁻¹ and subsequently merged. The merging of SAXS profiles is customary to generate a profile of sufficient signal-to-noise in the entire q -range. This is required for subsequent data analysis without introducing interference effects due to non-negligible protein–protein interactions (i.e., $S(q)$ deviates from unity), which becomes more prominent at low q -values and elevated concentrations. The normalized background scattering profile of the buffer and polycarbonate cell was subtracted from the normalized sample scattering profiles to obtain the protein scattering curve. The absolute scale calibration of the scattering curves was verified using the known scattering cross-section per unit sample volume, $\Delta\Sigma/\Delta\Omega$, of water, being $\Delta\Sigma/\Delta\Omega(0) = 0.01632 \text{ cm}^{-1}$ for $T = 20$ °C.^{10,11}

Data analysis

All SAXS data processing steps, such as solvent subtraction and data merging, were performed using PRIMUS from the ATSAS software package.¹² The experimental 1D scattering profiles were analyzed using a Guinier approximation to extract the radius of gyration (R_g) and the forward scattering intensity $I_0 = \Delta\Sigma/\Delta\Omega(q = 0)$, which is valid for monodisperse spherical particles at small angles $q \leq 1.3/R_g$. The forward scattering intensity I_0 was used to calculate the molar mass of the protein. Furthermore, the scattering profiles were analyzed using a form factor for self-avoiding worm-like chains (WLCs),¹³ which is implemented in the software package SASview. Information on the dimensions of the proteins was extracted assuming a uniform scattering length density along the cross-section.

Molecular shape reconstruction

The *ab initio* molecular shape of the protein in solution was reconstructed using simulated annealing methods implemented in DAMMIN.⁶ First, an inverse Fourier transformation was applied to the experimental scattering data to obtain the RDF (radial distribution function), describing the probability of finding interatomic vectors of length (r) within the scattering particle, using GNOM.¹⁴ The maximum linear dimension (D_{max}) was set to approximately $3 \times R_g$ and adjusted to give the best fit to the experimental data. The RDF was considered to be zero at $r = 0 \text{ \AA}$ and approaches zero at D_{max} . The GNOM output files were used as input for the simulated annealing calculations using DAMMIN. Ten independent dummy atom models were calculated from a predefined cylindrical shape with radius $r = 25 \text{ \AA}$ and length $l = 200 \text{ \AA}$, without point symmetry (P1). The ten different models were aligned using DAMSEL followed by DAMSUP, and averaged using DAMAVER to compute the probability map.⁷ Finally, DAMFILT was used to filter the averaged model to give a structure that has high densities on the probability map representing the molecular shape of the protein in solution.

6.6 References

1. Guo, S.; Garnham, C.P.; Whitney, J.C.; Graham, L.A.; Davies, P.L. *PloS One* **2012**, *7*, e48805.
2. Guo, S.; Garnham, C.P.; Karunan Partha, S.; Campbell, R.L.; Allingham, J.S.; Davies, P.L. *FEBS J.* **2013**, *280*, 5919-5932.
3. Gilbert, J.A.; Davies, P.L.; Laybourn-Parry, J. *FEMS Microbiol. Lett.* **2005**, *245*, 67-72.
4. Garnham, C.P.; Gilbert, J.A.; Hartman, C.P.; Campbell, R.L.; Laybourn-Parry, J.; Davies, P.L. *Biochem. J.* **2008**, *411*, 171-180.
5. Vance, T.D.; Olijve, L.L.C.; Campbell, R.L.; Voets, I.K.; Davies, P.L.; Guo, S. *Biosci. Rep.* **2014**, *34*, 357-368.
6. Svergun, D.I. *Biophys. J.* **1999**, *76*, 2879-2886.
7. Volkov, V.V.; Svergun, D.I. *J. Appl. Crystallogr.* **2003**, *36*, 860-864.
8. Svergun, D.I.; Barberato, C.; Koch, M.H.J. *J. Appl. Crystallogr.* **1995**, *28*, 768-773.
9. Pedersen, J.S.; Laso, M.; Schurtenberger, P. *Phys. Rev. E*, 1996, **54**, R5917-R5920.
10. Glatter, O.; Kratky, O. eds. *Small-angle X-ray Scattering*. Academic Press, London, **1982**
11. Mylonas, E.; Svergun, D.I. *J. Appl. Cryst.* **2007**, *40*, s245-s249.
12. Konarev, P.V.; Volkov, V.V.; Sokolova, A.V.; Koch, M.H.J.; Svergun, D.I. *J. Appl. Crystallogr.* **2003**, *36*, 1277-1282.
13. Pedersen, J.S.; Schurtenberger, P. *Macromolecules* **1996**, *29*, 7602-7612.
14. Svergun, D.I. *J. Appl. Crystallogr.* **1992**, *25*, 495-503.

Summary

The detrimental impact of ice formation and growth on the structural integrity and performance of materials warrants the use of antifreeze agents in many industrial applications. Current de-icing and anti-icing strategies involve the use of colligative antifreeze agents, such as glycols or salts. However, these additives are often destructive for the physical properties of soft materials, especially colloidal systems, complex liquids and biological materials. Hence, soft materials require a different strategy to realize freeze tolerance without affecting their mechanical, structural and functional properties. In this thesis, the development of new technologies and strategies to produce freeze tolerant soft matter is described, based on natural antifreeze proteins and synthetic ice binding macromolecules.

Chapter 1 describes a strategy that many cold-adapted organisms have developed to overcome the risk of freeze damage: they produce antifreeze proteins (AFPs), which adsorb onto embryonic ice crystals and thereby arrest further ice growth. On a macroscopic level, direct ice binding of AFPs results in ice shaping, inhibition of ice recrystallization (IRI) and depression of the non-colligative freezing point (thermal hysteresis; TH). This introductory chapter further describes what is currently known about the working mechanism of AFPs, and methods to measure AFP activity. Next, recent advances in polymer sciences are described, which serves as background for the design strategies of inexpensive polymer-based materials that mimic AFP activity. Furthermore, a short introduction into small angle X-ray scattering (SAXS) for macromolecular structure determination in solution is given, followed by the aim and outline of this thesis.

In chapter 2, the antifreeze activity of all major classes of AFPs is studied by nanoliter cryoscopy, sonocrystallization and optical microscopy to evaluate the ability to inhibit the recrystallization of ice and lower the non-equilibrium freezing point. The results show that binding to fast growing non-basal ice planes is a prerequisite for effective inhibition of ice recrystallization and non-colligative freezing point depression at cooling rates favoring rapid ice growth (sonocrystallization and IRI). Accumulation of AFPs onto slow growing basal planes is only important under slow ice growth conditions, as in cryoscopy. The insights described in this chapter provide a deeper understanding of the underlying mechanism that governs IRI and TH activity, and supports the development of synthetic mimics and innovative strategies for cryoprotection and anti-icing technologies. Contrary to the current pursuit, synthetic strategies should target prism and not basal plane ice binders.

Chapter 3 focuses on poly(vinyl alcohol) (PVA), which is an inexpensive material known to inhibit ice recrystallization. Despite the early discovery of its IRI activity, the mechanism of ice binding is still not understood. For example, it is unknown whether AFPs and PVA bind ice in a similar fashion, and direct evidence for binding of PVA to prism, pyramidal or basal

planes is lacking. In this chapter, the synthesis of PVA is described via reversible addition-fragmentation chain-transfer (RAFT) polymerization of four vinyl ester monomers with varying bulky substituents, aiming to evaluate the impact of polymer tacticity on the multivalent ice-PVA interaction. However, only a minimal difference in polymer tacticity (5-6 %) was obtained via this strategy. Therefore, a reliable quantification of the effect of tacticity on antifreeze activity could not be obtained. Furthermore in this chapter, PVA with a naphthalimide end-functionalization (Napht-PVA) is prepared to study the ice binding of PVA in more detail via fluorescence microscopy.

In chapter 4, PVA molecular bottlebrushes are synthesized and their activity compared to linear PVA to evaluate if chain architecture impacts performance by strengthening the multivalent ice-PVA interaction. PVA brushes are prepared via a combination of atom-transfer radical polymerization (ATRP) and RAFT polymerization, resulting in a rigid poly(hydroxyethyl methacrylate) (PHEMA) backbone with densely grafted PVA side chains. SAXS experiments demonstrate that the PVA brushes exhibit an extended topology. Evaluation of the antifreeze activity of the PVA brushes by IRI assays and sonocrystallization experiments shows that the brush-like polymer architecture does not increase the antifreeze performance of PVA compared to linear polymers. The effective weight concentration of PVA in solution determines antifreeze activity; chain architecture does not play a significant role.

Since AFPs adsorb onto ice crystals from solution, it is important to characterize their solution structure in detail. Chapter 5 and 6 describe the use of SAXS for the structural characterization of highly asymmetric antifreeze proteins in solution. In chapter 5, the size and shape of a highly potent antifreeze protein from winter flounder (hypAFP1) is measured to assess the validity of a previously proposed molecular model of a fully extended double helix. Based on the SAXS profiles and data analysis including *ab initio* modeling, we conclude that hypAFP1 assembles into a folded helix bundle where the individual α -helices are not fully extended.

In chapter 6, SAXS is used to validate the crystal structure of the calcium binding tetrameric RII protein (tetraRII) in the presence of calcium. Furthermore the structure of tetraRII in the absence of calcium is studied, which is impossible by XRD since no protein crystals could be obtained in the absence of calcium. The SAXS experiments demonstrate that the calcium-bound structure of tetraRII is less flexible, which explains the functional role of the RII protein domain in anchoring of Antarctic bacteria to ice surfaces.

Curriculum Vitae

Luuk Olijve was born on September 3, 1987 in Heerlen, the Netherlands. After finishing his atheneum (pre-university) degree at the Sintermeerten College in Heerlen in 2005, he started his study in Biomedical Engineering at the Eindhoven University of Technology (TU/e). The Master's program of his study included a research internship in the group of Prof. Songi Han at the university of California Santa Barbara (UCSB, Santa Barbara, USA), as part of the Cooperative International Science and Engineering Internships (CISEI) of the Material Research Laboratory. A second research internship as part of his Master's degree was done at the University of New South Wales (UNSW, Sydney, Australia) under supervision of Dr. Pall Thordarson. His Master's program was completed with a research project on the characterization of self-assembled hydrogels by nuclear magnetic resonance in the group of Prof. Bert Meijer, under supervision of Dr. Tom de Greef, Dr. Marcel van Genderen and Dr. Patricia Dankers. After obtaining his Master's Degree in 2011, he started his PhD research in the laboratory of Macromolecular and Organic Chemistry and the Intitute for Complex Molecular Systems (ICMS) at the Eindhoven University of Technology under supervision of Prof. Bert Meijer and Dr. Ilja Voets. His work focussed on understanding the working mechanism of antifreeze proteins and the development of synthetic ice-binding polymers for innovative cryoprotection and anti-icing technologies for sustainable soft materials. The most important results of his research are presented in this dissertation.

List of publications

1. Olijve, L.L.C.; Meister, K.; DeVries, A.L.; Duman, J.G.; Guo, S.; Bakker, H.J.; Voets, I.K. *submitted*.
2. Lotze, S.; Versluis, J.; Olijve, L.L.C.; Van Schijndel, L.; Milroy, L.G.; Voets, I.K.; Bakker, H.J. *submitted*.
3. Meister, K.; Lotze, S.; Olijve, L.L.C.; DeVries, A.L.; Duman, J.G.; Voets, I.K.; Bakker, H.J. *J. Phys. Chem. Lett.* **2015**, *6*, 1162-1167.
4. Meister, K.; Strazdaite, S.; DeVries, A.L.; Lotze, S.; Olijve, L.L.C.; Voets, I.K.; Bakker, H.J. *Proc. Natl. Acad. Sci. USA* **2014**, *111*, 17732-17736.
5. Cheng, C.Y.; Olijve, L.L.C.; Kausik, R.; Han, S. *J. Chem. Phys.* **2014**, *141*, 22D513.
6. Lotze, S.; Olijve, L.L.C.; Voets, I.K.; Bakker, H.J. *J. Phys. Chem. B* **2014**, *31*, 8962-8971.
7. Vance, T.D.; Olijve, L.L.C.; Campbell, R.L.; Voets, I.K.; Davies, P.L.; Guo, S. *Biosci. Rep.* **2014**, *34*, 357-368.
8. Olijve, L.L.C.; Sun, T.J.; Narayanan, T.; Jud, C.; Davies, P.L.; Voets, I.K. *RSC Advances* **2013**, *3*, 5903-5908.
9. Janssen, B.M.G.; Lempens, E.H.M.; Olijve, L.L.C.; Voets, I.K.; Van Dongen, J.L.J.; De Greef, T.F.A.; Merckx, M. *Chem. Sci.* **2013**, *4*, 1442-1450.
10. Olijve, L.L.C.; How, E.N.W.; Bhadhade, M.; Prasad, S.; Colbran, S.B.; Zhao, C.; Thordarson, P. *J. Porphyrins Phthalocyanines* **2011**, *15*, 1-9.
11. Besenius, P.; Van den Hout, K.P.; Albers, H.M.H.G.; De Greef, T.F.A.; Olijve, L.L.C.; Hermans, T.M.; De Waal, B.F.M.; Bomans, P.H.H.; Sommerdijk, N.A.J.M.; Portale, G.; Palmans, A.R.A.; Van Genderen, M.H.P.; Vekemans, J.A.J.M.; Meijer, E.W. *Chem. Eur. J.* **2011**, *17*, 5193-5203.

Dankwoord

Niet te vergeten het belangrijkste onderdeel van het proefschrift: het dankwoord. Daar waar de experimentele hoofdstukken vaak met het idee “ik geloof het wel” worden doorgenomen, wordt het dankwoord uiterst nauwkeurig en kritisch bekeken. En terecht, een boek schrijf je nooit alleen, maar wordt onbewust geschreven door iedereen die er ook maar in enige mate bij betrokken is tijdens je PhD-tijd.

Veel dank gaat uit naar Bert en Ilja. Ilja, ik denk dat je dit ook wel deels jouw boekje kan noemen. Zoveel tijd en energie die jij in het doorlezen en corrigeren hebt gestoken, heel veel dank daarvoor. Niet alleen jouw brede kennis binnen de fysische chemie, ongeremde energie tijdens lange dagen op het synchrotron, en het gemak waarmee je nieuwe samenwerkingen met verschillende vakgebieden weet op te zetten, maar vooral jouw nieuwe ideeën maakt jou een onderzoekster die naar mijn idee perfect op de juiste plaats zit binnen het ICMS. Ook bij het onderzoek naar de antivries eiwitten zijn we vanaf nul begonnen (geen eiwitten, geen polymeren en geen analyse methode), en zijn we toch tot nieuwe inzichten gekomen die nog meer stof doen opwaaien. Ookal zijn het een beetje ‘rare’ eiwitten, de interesse vanuit academie en industrie blijft verbazend groot, met nog genoeg onderzoek te doen voor de komende jaren. Heel erg veel dank voor de afgelopen 4 jaar. Jouw deur stond altijd voor alles open. En ik wens Thijs en jou veel geluk in jullie nieuwe huisje.

Bert, ik heb enorm veel bewondering hoe je op een charmante en gemoedelijke manier het onderzoek in jouw groep aanstuurt. Ondanks een drukke agenda ben je altijd op de hoogte van ieders voortgang in het onderzoek, maar nog meer van ieders persoonlijke situatie en ontwikkeling, zowel van staflid tot beginnende stagair. Het ICMS is een zeer mooi onderzoeksinstituut geworden, dat vast en zeker in de ‘championsleague’ zal meedraaien (iets wat ik Ajax voorlopig niet zie doen).

I’m very grateful that I was able to work in two succesful collaborations, both which held a great contribution to this dissertation: Konrad Meister, Stephan Lotze en prof. Huib Bakker of the AMOLF in Amsterdam, and Phil, TSun and prof. Peter Davies of Queen’s University in Kingston, Canada. Konrad, thanks a lot for helping with Chapter 2. I have to acknowledge that you noticed the correlation between activity and ice binding planes first, and you got me convinced after all. Hopefully, Eindhoven and Amsterdam will keep working together with many more results to come, and maybe someday we might completely understand how these proteins work. Stephan, I was happy I could provide you with some of the proteins and admire your detailed analysis.

TSun, thanks for preparing the Maxi protein described in Chapter 5. Although the protein was not quite easy to handle, the crystal structure you resolved looks amazing. Phil and Tyler, thanks for preparing the R2t protein described in Chapter 6. Phil, I hope you enjoyed your visit

to Eindhoven and the synchrotron. Maybe one day we can fully understand that weird Antarctic bacterium of yours.

I highly appreciate prof. Art DeVries, dr. Matthew Gibson, prof. Jan van Hest, prof. Nico Sommerdijk and prof. Emmo Meijer for reading the dissertation and taking place in the defense committee. Also I would like to thank prof. René Jansen for taking place as chairman.

Ik heb de afgelopen 6 jaar met plezier gewerkt binnen SMO. Brian, mijn BMT-broer vanaf het eerste moment! We kennen ons al vanaf de middelbare school, en eigenlijk al eerder van de derby's tussen Voerendaal en Ubachsberg. Tijdens de studie kon ik er elke keer van genieten om jou op maandag ochtend om 7u in bus 40 te zien zitten met je slaaphoofd en de haren alle kanten op, dan wist ik dat het weer een goede week ging worden. Ik ben blij dat dat je samen met Remco mijn paranimf wilt zijn. Remco, jij bent echt inne goeie! Binnen SMO ben jij een drijvende kracht achter alles wat niks met werk te maken heeft. Borrels, feestjes en voetbaltrainingen, jij zorgde ervoor dat iedereen van de partij was. Nou mag je op 8 oktober dat feestje regelen nog eens dunnetjes over doen. En ik ga er vanuit dat je op de zondagen veel doelpunten gaat maken. Janus, gij zijt ook inne goeie! Gelukkig zijn we voorlopig nog niet van al jouw gezwets verlost, want SMO zal aardig stil worden zonder. Van mij mag je tijdens de verdediging een stoel erbij pakken en gezellig naast Remco gaan zitten. Overigens is het met een grote koptelefoon op ook nog eens best goed uit te houden met jou op kantoor. Dan is er nog het 'snoepvoorraad' kantoor. Ralph, jij bent de beste! Thuur, jij bent zowaar nog beter dan Ralph! Lidia, thanks for making fun of me all the time!

Luuk van Schijndel, jij was mijn beste afstudeerder! (ook de enige) Het was geen gemakkelijk project waar we jou aan lieten werken, en met elk resultaat haalde je onze mooie theorie helemaal onderuit. Je liet je niet van de wijs brengen en bleef doorgaan. Jouw werk heeft de eerste stap gezet naar hoofdstuk 2, en ook nog eens een mooie publicatie samen met Stephan. En wacht maar af, ooit verbeter ik jouw tijd op de halve marathon.

I would like to acknowledge Lech for a lot of help in the peptide synthesis of the type I AFP. Marco Hendrix, bedankt voor de AFM metingen op het allerlaatste moment voor de concept versie van het proefschrift. René, we hebben bijna 4 jaar lang een zuurkast gedeeld zonder dat er ook maar één keer met rondbodemkolven door de lucht werd gegooid. Bedankt man! Het originele kantoor met Patrick, Isja en Rob heeft heel lang stand gehouden. Bedankt voor jullie hulp en het delen van alle bloed-zweet-en-tranen momentjes. Louis, I had a great time during the ACS conference in New Orleans (although Bourbon street is the only thing I can remember), and I very much enjoyed visiting your hometown. I really have to go back sometime when there is no tons of snow and rain. Joséke, Miguelino, Matt and Nic, thanks a lot for stealing all the cookies in our office and interrupting our magnificent scientific work.

Onderzoek is niet mogelijk zonder al het werk dat uit handen wordt genomen door de stafleden binnen SMO. Veel dank gaat daarom ook uit naar het analytisch team: Ralf, Lou en Joost; het secretariaat team: Martina, Nora, Jolanda, Carla en Marjo; Hans voor het regelen van alle bestellingen; Henk voor de koffie ‘zo sterk dat er een spijker in blijft drijven’. Als niet-chemicus heb ik heel veel bijgeleerd van Jolanda en Bas ‘succescoach’ vd Waal. Jolanda, bedankt dat ik in het beste lab van Eindhoven heb mogen werken. Bas, jij bent simply the best!

Dan is er natuurlijk nog een belangrijke dosis afleiding, zonder welke ik vast en zeker veel meer voor de wetenschap had kunnen betekenen. De oekels uit Wijnandsrade en omstreken: Ruud, Mark, Jeroen, Brett en Tim; de BMT boys: Frank, Joep, Rieneke, Anne, Jelle, Thomas, Leo en Bert, en de mannen van WODAN 8 voor de afleiding in de weekenden, geouwehoer op de training en kantine dagen met koppijn op de maandag tot gevolg.

Koen, bedankt voor je hulp met de cover, het ziet er nu zeker beter uit. Pap en mam, ookal begrijp je geen woord van wat er in dit boekje beschreven staat, jullie bijdrage is misschien wel het grootst van allemaal. Bedankt voor alle goede zorg voor de afgelopen 27 jaar.

Luuk

